

Fractal Charge Carrier Recombination Kinetics

in Photocatalytic Systems

Von der Naturwissenschaftlichen Fakultät
der Gottfried Wilhelm Leibniz Universität Hannover
zur Erlangung des Grades

Doktor der Naturwissenschaften
(Dr. rer. nat.)

genehmigte Dissertation von

Fabian Sieland, M. Sc.

geboren am 04.09.1990 in Bad Pyrmont

2018

Referent: Prof. Dr. rer. nat. habil. Detlef W. Bahnemann

Korreferent: Prof. Dr. Christophe Colbeau-Justin

Korreferentin: Prof. Dr. rer. nat. Nadja-Carola Bigall

Tag der Promotion: 23. April 2018

Für meine Familie

Danksagung

Die letzten 2,5 Jahre im Arbeitskreis von Prof. Dr. Bahnemann haben mich in vielseitiger Hinsicht sehr geprägt. Daher möchte ich die Gelegenheit nutzen, um an dieser Stelle meinen Dank auszusprechen. Zuallererst gilt mein Dank Prof. Bahnemann, für die hervorragende Betreuung, die ich während der gesamten Promotionszeit als freundschaftlich und respektvoll empfunden habe.

Mit hohen Erwartungen und großer Vorfreude entschied ich mich genau für diesen Arbeitskreis, in dem jederzeit eine angenehme Arbeitsatmosphäre herrschte. Darüber hinaus findet in diesem Arbeitskreis ein grenzenloser fachlicher Austausch in einem besonders internationalen Umfeld statt. Diese Umgebung hat maßgeblich zum Erfolg dieser Arbeit beigetragen und nur ungern würde ich die letzten Jahre missen.

Prof. Dr. Thomas Scheper möchte ich meinen Dank aussprechen für die Gelegenheit am Institut für Technische Chemie zu promovieren und für die Bereitschaft den Prüfungsvorsitz zu übernehmen.

Prof. Dr. Christophe Colbeau-Justin danke ich ebenfalls ganz herzlich für die Bereitschaft zur Übernahme des Korreferats.

Prof. Dr. Nadja Bigall spreche ich ebenso meinen Dank für die Bereitschaft zur Übernahme des Korreferats aus.

Darüber hinaus danke ich Prof. Wonyong Choi für besondere Gastfreundschaft und die Möglichkeit photokatalytische Messungen an der POSTECH in Pohang, Südkorea, durchzuführen.

In besonderem Maße gilt mein Dank auch Dr. Jenny Schneider, die mich bei inhaltlichen und organisatorischen Fragen unterstützt hat und zusätzlich meine wichtigste Ansprechperson war. Ohne ihr fachliches „Knowhow“ und ihre Einweisung in die Laser-Blitz-Photolyse Spektroskopie, wäre mir eine Promotion auf diesem Gebiet deutlich schwerer gefallen. Natürlich danke ich darüber hinaus auch Dr. Dillert und Prof. Patrocínio für die Weitergabe von Erfahrung und zahlreichen inhaltlichen Diskussionen.

Mein besonderer Dank geht an meine Kollegen und Freunde im Arbeitskreis von Prof. Bahnemann, die mir über die letzten Jahre sehr ans Herz gewachsen sind.

Vermissten werde ich die intensiven Gespräche und Diskussionen in den Mittagspausen mit Stephanie Melchers, Ana Blanco, Camilla Sehring, Lena Megatif, Arsou Arimi, Christoph Haisch, Maryam Jami und Manuel Fleisch.

Anh-Thu Duong gilt ebenfalls mein Dank für die tatkräftige Unterstützung meiner Forschung als Masterstudentin, Kollegin und Freundin. Ebenfalls danke ich Lisa Rehbock und Thorsten Lippmann, die beide im Rahmen meiner Promotionstätigkeit ihre Bachelorarbeiten geschrieben haben.

Ich möchte mich darüber hinaus außerordentlich bei meiner Familie und meinen Freunden bedanken. Sie haben stets größtes Vertrauen in mich gehabt und mich während der gesamten Studienzzeit unterstützt.

Zusammenfassung

Die Photokatalyse ermöglicht die Zersetzung von zahlreichen ungewünschten Verbindungen aus Luft und Abwasser. Jedoch sind die grundlegenden Elementarreaktionen der Photokatalyse in den vergangenen Jahrzehnten größtenteils unerforscht geblieben, obwohl das genaue Verständnis der geschwindigkeitsbestimmenden Reaktion die Entwicklung aktiverer Photokatalysatoren ermöglichen sollte. Der Photokatalysator Titandioxid (TiO_2) ist bisher am intensivsten erforscht worden, trotzdem gibt es noch viele ungeklärte Fragestellungen, im Besonderen im Bereich der kinetischen Analyse der Ladungsträgerrekombination. Weiterhin ist noch immer strittig, welchen Einfluss die Änderung der Partikelgrößenverteilung oder einfach Zusätze wie Karbonate auf den photokatalytischen Prozess besitzen.

Im Rahmen dieser Arbeit wurde die Rekombination der lichtinduzierten Ladungsträger in TiO_2 Pulvern mit Hilfe der Laserblitzphotolyse Spektroskopie untersucht. Dafür wurden die transienten Reflektionssignale der getrappten Ladungsträger in TiO_2 -Pulvermischungen mit binärer Partikelgrößenverteilung und TiO_2 -Pulvermischungen mit baustoffähnlichen Zusatzstoffen detektiert und analysiert. Auf der Basis der fraktalen Dimensionen der Pulveroberflächen wurde schließlich ein Modell für die mathematische Analyse der Rekombinationskinetik hergeleitet. Dieses Modell zeigt im Vergleich zu anderen Fit-Funktionen eine höhere Verlässlichkeit in der Anwendung und ermöglicht den schnellen Vergleich der Ladungsträgerkinetik von Pulverproben.

Darüber hinaus korrelieren die Messungen des photokatalytischen NO Abbaus der Proben sehr gut mit den Ergebnissen aus der Laserblitzphotolyse. Proben mit hoher photokatalytischer Aktivität zeigen gleichzeitig entweder besonders langlebige oder besonders hohe Ladungsträger-Signale. Das fraktale Modell ermöglicht hierbei die einfache Identifikation des Wirkmechanismus der zu TiO_2 zugegebenen Additive. Der Zusatz von Natrium-Ionen führt beispielsweise zu einer schnelleren Ladungsträgerrekombination in TiO_2 , welche die photokatalytische Aktivität der entsprechenden Proben verringert.

Stichwörter: Photokatalyse, Titandioxid, Laserblitzphotolyse, Ladungsträger-Rekombinationsdynamik, Fraktale Kinetik, Stickstoffmonoxid-Abbau.

Abstract

Photocatalysis can be utilized to decompose several undesired organic and inorganic compounds present in air and water. However, the underlying basic reactions of the photocatalytic process have remained largely unexplored during the past few decades, even though detailed knowledge about the rate limiting step makes it possible to facilitate the development of photocatalysts with higher photocatalytic activity. The most studied photocatalyst is TiO_2 ; nevertheless, there are still many unsolved questions, in particular in the area of the kinetic analysis of charge carrier recombination. Moreover, the effects of the particle size distribution of TiO_2 and the addition of carbonates on the photocatalytic process are still discussed controversially.

In this study, the recombination of photo-generated charge carriers in TiO_2 was investigated employing laser flash photolysis spectroscopy. The transient reflectance signals of trapped charge carriers in TiO_2 powder samples were detected. TiO_2 mixtures with binary particle size distribution and TiO_2 mixtures with additives related to construction materials were analyzed, respectively. Subsequently, a model for the mathematical analysis of charge carrier recombination was derived from the fractal geometry of the powder samples. In comparison to other fit functions, the fractal model shows a higher reliability and facilitates the fast comparison of the charge carrier recombination kinetics of powder samples.

Furthermore, the detected photocatalytic NO degradations of the samples correlate well with the results obtained by laser flash photolysis spectroscopy. Samples with higher photocatalytic activity display relatively high or long-lived charge carrier signals. In this context, the fractal model enables the identification of the effects observed upon mixing with different additives. The addition of sodium ions, for instance, causes a faster charge carrier recombination in TiO_2 , which explains the smaller photocatalytic activities detected for the respective samples.

Keywords: photocatalysis, titanium dioxide, transient reflectance spectroscopy, charge carrier recombination dynamics, fractal kinetics, nitric oxide degradation.

Table of contents

1. Introduction and purpose of study	1
2. Theoretical background	5
2.1 Photocatalysis	5
2.1.1 Basic processes of semiconductor photocatalysis	5
2.1.2 Titanium dioxide	6
2.1.3 Photocatalytic NO _x degradation employing TiO ₂	9
2.2 Kinetic analysis of charge carrier recombination	12
2.2.1 Transient absorption spectroscopy (TAS).....	13
2.2.2 Second order kinetics	15
2.2.3 Fractal kinetics	17
2.2.4 Power law decays	19
3. Materials and experimental methods	21
3.1 Materials	21
3.2 Preparation	21
3.3 Instrumentation	23
3.4 Experimental methods	23
3.4.1 Transient reflectance spectroscopy	23
3.4.2 Photocatalytic NO degradation	27
4. Results.....	29
4.1 Pure TiO₂ samples	29
4.1.1 Transient reflectance spectra	29
4.1.2 Second order fit with baseline	30
4.1.3 Fractal kinetics fit.....	35
4.1.4 Photocatalytic NO degradation	39
4.2 TiO₂ powders with binary particle size distribution.....	40
4.2.1 Structure of the TiO ₂ agglomerates	40
4.2.2 Transient reflectance signals observed for the TiO ₂ agglomerates	41
4.2.3 Photocatalytic NO degradation by the TiO ₂ agglomerates	43
4.2.4 Surface area of the TiO ₂ agglomerates.....	44
4.3 TiO₂ powders mixed with additives	45
4.3.1 TiO ₂ -BaSO ₄	46
4.3.2 TiO ₂ -Na ₂ CO ₃ and TiO ₂ -CaCO ₃	49
4.4 TiO₂ paints	51

5. Discussion	57
5.1 Transient reflectance signals in TiO₂	57
5.1.1 Identification of trapped charge carriers	57
5.1.2 Choice of experimental parameters	58
5.2 Analysis of charge carrier recombination kinetics	63
5.2.1 Second order decay kinetics vs. fractal kinetics	63
5.2.2 Fractal kinetics vs. power law decay	71
5.2.3 Model of charge carrier segregation on surfaces	74
5.2.4 Application of the fractal fit function on the experimental data.....	79
5.2.5 Fractal kinetics fit as a meaningful kinetic analysis?.....	83
5.3 TiO₂ samples with binary particle size distribution	89
5.3.1 Charge carrier kinetics	89
5.3.2 Photocatalytic NO degradation	93
5.4 TiO₂ samples mixed with additives	98
5.4.1 Influence of BaSO ₄	98
5.4.2 Influence of carbonates	102
5.5 TiO₂ paints	108
6. Summary and conclusions	113
7. References.....	119
Appendix	133
Publications.....	143
Curriculum vitae	IX

Abbreviations

Abs	Absorbance
BET	Specific surface area (Brunauer Emmett Teller)
CB	Conduction band
FWHM	Full width at half maximum
IR	Infrared
NIR	Near infrared
NO	Nitrogen monoxide
NO _x	Nitrogen oxides
ROS	Reactive oxygen species
TEM	Transmission electron microscopy
TiO ₂	Titanium dioxide
TAS	Transient absorption spectroscopy
TRMC	Time resolved microwave conductivity
UV	Ultraviolet (315-380 nm)
VB	Valence band
Vis	Visible (380-760 nm)
Wt	Weight

Symbols and constants

A_{SA}	Geometrical surface area
A	Beginning height of transient reflectance†
B	Baseline†
c	Speed of light ($2.998 \cdot 10^8 \text{ m s}^{-1}$)

E_{BG}	Bandgap energy
e^-	Electron
ξ_{NO}	Photonic efficiency taken from the NO degradation
ν	Frequency (Hz)
$\phi(365\text{ nm})_{NO}$	Apparent quantum yield taken from the NO degradation employing 365 nm illumination
h	Fractal parameter†
h_p	Planck's constant ($6.626 \cdot 10^{-34} \text{ m}^2 \text{ kg s}^{-1}$)
h^+	Hole
I	Light intensity
ΔJ	Change in reflectance (%)
k_2	Second order recombination rate constant†
$k_{2,f}$	Fractal recombination rate constant†
λ	Wavelength (nm)
N_A	Avogadro constant ($6.022 \cdot 10^{23} \text{ mol}^{-1}$)
R_c	Gas constant ($8.314 \text{ J mol}^{-1} \text{ K}^{-1}$)
R	Reflected light at 365 nm
p	Pressure (1013 hPa)
t	Time (s)
T	Temperature (298.15 K)
\dot{V}	Volume flow ($5.0 \cdot 10^{-5} \text{ m}^3 \text{ s}^{-1}$)

† (parameter of fit function)

1. Introduction and purpose of study

The future global problems of humanity lie in the fields of energy, water, and environment. During the past few centuries, the global economy and transportation have been depending on the use of fossil fuels. However, burning of these carbon compounds increases the concentration of carbon dioxide and nitrogen oxides (NO_x) in the atmosphere, which leads to global warming.¹ If the global warming process cannot be stopped or slowed down, climate change will result in a higher probability of storms, floods, and a general rise of the sea level.² The increasing levels of chemical compounds in the atmosphere, such as toxic NO_x, start to represent a severe risk for human health in several ways.³ Annual records in the local concentration of NO_x have been detected in urban areas due to the large number of cars with conventional combustion engines and the presence of industrial facilities.^{3,4} Moreover, the recent limit-exceeding NO_x emissions from diesel cars has raised concerns about the success of political and economic attempts to reduce the amount of NO_x engine emissions.⁵

In addition to the increased release of toxic gases in the environment, the quality of the water in urban areas is endangered as well.^{6,7} For example, the contamination of drinking water is not solely observed in large cities. In less developed regions of the world, the removal of bacteria as well as the conversion of wastewater into drinking water represents a topic of high importance.⁸⁻¹⁰ In sum, the treatment of wastewater is a global issue, since pure water is a precious and limited product.

Overall, the world is facing a discouraging future, if no sustainable solution for the aforementioned problems can be found and utilized. Photocatalysis represents a key technology with a large potential for future applications in the fields of energy and environment.^{11,12} Currently, the application of photocatalysis for energy storage or production of electricity seems to be unlikely, since the direct conversion of solar energy to electricity is already commercially available with photovoltaic devices.¹³ Nevertheless, the huge potential of photocatalysis stems from its flexibility for utilization of solar energy for specific chemical reactions, e.g., water or air purification,^{12,14-16} selective chemical transformations, and the synthesis of solar fuels from biomass or waste.^{17,18} These numerous possible applications of photocatalysis could result in a reduction in the future fossil fuel consumption and might solve current environmental problems like air and water pollution.

Nonetheless, despite all the studies which have been performed with semiconductor photocatalysts, there is still not a complete understanding of the photocatalytic process. In the last few decades, a large number of new photocatalysts have been developed to improve the photocatalytic activity.^{19,20} Yet many types of photocatalysts, such as ZnO or CdS, demonstrate a somewhat negative stability under illumination.¹⁹ Several strategies, for instance coating of the CdS surface, have been tested to improve the stability of these compounds.²¹ However, TiO₂ still represents the best photocatalyst for commercial applications, because of its stability, availability, price, and nontoxicity.¹⁴

Nevertheless, photocatalysis is not often found in large-scale applications. The reason for that are two main limitations in the photocatalytic process. First, the photocatalytic activity is limited by charge carrier recombination. Over 90 % of the charge carriers in TiO₂ recombine during the first nanoseconds following their generation by bandgap illumination and, subsequently, are unavailable for the photocatalytic reaction.²² Second, the low photocatalytic activity of commercially available TiO₂ photocatalysts requires the use of high microscopic surface areas.²³

One possible solution can be found in the utilization of the surface of building materials; however, the photocatalytic activities of real surfaces, such as the photocatalytic activity of TiO₂ containing paints, are often much smaller compared to those obtained under laboratory conditions.²⁴ Chemical compounds, such as binders, polymers, or stabilizers, present on the surface of TiO₂, can interfere with the photocatalytic reaction, and their potential impact on the photocatalytic performance is not predictable. While some additives show a beneficial effect on the photocatalytic activity,²⁵ other additives poison the catalyst surface and cause deactivation of the photocatalyst.²⁶ Deeper insights into the mechanism of photocatalysis are required and the influence of single additives on the photocatalytic basic processes, namely, charge carrier recombination and charge transfer needs to be investigated. The development of materials with beneficial properties is of vital importance for the design of future photocatalysts with higher photocatalytic activities.²⁷ Ideally, these properties include that a large amount of charge carriers survive the fast recombination processes in these materials and the trapped charge carriers, which survived the bulk recombination, display small recombination rates.

The analysis of charge carrier recombination rates depends on the physical detection of the charge carrier concentration in the semiconductor sample. Among other technologies, the

trapped or free charge carriers in TiO₂ can be measured optically by transient absorption spectroscopy.²⁸ This technique was adapted to evaluate optically dense powder surfaces by Wilkinson in 1981.²⁹ Currently, the use of transient spectroscopy facilitates the analysis of the charge carrier kinetics in semiconductor materials in time domains ranging from femtoseconds to seconds.^{30,31} Nonetheless, the prevention of the charge carrier recombination is only possible if the recombination can be detected quantitatively, and the comparison of results between different measurements and laboratories is feasible. Hence, kinetic analysis of the transient signals requires the use of mathematical fitting models.

Up until today, charge carrier signals in TiO₂ have been fitted to monoexponential,³² double-exponential,³³ and second order^{14,30,34,35} decay functions. Nevertheless, no generally accepted model for the mathematical description of the charge carrier recombination in semiconductors is available. The above-mentioned fit functions essentially suffer either from an arbitrary baseline, or the physical interpretation of the modeled parameters is problematic. In particular, the baseline of the second order fit function summarizes the processes not matching the selected fit function in one arbitrary parameter.³⁶

Apart from mathematical fitting models of charge recombination, many researchers have tried to gain a deeper understanding of the photocatalytic process. For instance, Budarz *et al.* investigated the impact of single additives on the photocatalytic performance of TiO₂.³⁷ They reported an inhibition of photocatalytic iodide oxidation on TiO₂ by adsorbed phosphate and carbonate ions, while no effect was observed for the weakly bound nitrate, chloride, and sulfate ions. In comparison to this study, the work of Bardock *et al.* revealed conflicting results.³⁸ In fact, the authors detected no effect of carbonate ions on the photocatalytic oxidation of phenol. Moreover, the application of the reported findings for the degradation of gaseous compounds is not possible, since most of these studies were performed employing TiO₂ suspensions. Indeed, the photocatalytic process is highly substrate specific; therefore, even the comparability of the degradation of different probe molecules generally remains questionable.³⁹

Hence, the main task of the present work is to analyze and compare the available models for the kinetic analysis of charge carrier recombination in TiO₂ powder samples, with the intention to identify the best model available for a meaningful kinetic analysis. Ideally, the kinetic constants obtained from this model can be connected to physical properties of the sample and the model also avoids the use of an arbitrary baseline. Furthermore, the

1. Introduction and purpose of study

feasibility of the kinetic model needs to be analyzed and discussed for different semiconductors typically employed in photocatalytic systems. In the following steps, the impact of the particle size distribution or single additives on the charge carrier kinetics and photocatalytic activity can be investigated with the help of the selected model. Finally, this work aims to find a correlation between the detected charge carrier recombination constants and the photocatalytic NO degradation.

2. Theoretical background

The basic principles and mechanisms of photocatalysis on semiconductor surfaces are given in this chapter; in particular, the properties of TiO₂ and the photocatalytic degradation of NO as a potential application of TiO₂ for air treatment are described. Furthermore, the trapping processes of charge carriers in TiO₂ and the corresponding transient reflectance signals are shown in detail in **Chapter 2.2.1**. Finally, the principles of second order kinetics, power law decays and fractal kinetics are discussed as examples for the kinetic analysis of the charge carrier recombination in semiconductor samples.

2.1 Photocatalysis

In addition to air and water treatment,^{6,40} photocatalysis can be used for chemical synthesis^{41,42} and self-cleaning applications.⁴³ This study focuses on the degradation of gaseous NO over TiO₂ powder samples and on the kinetic analysis of the charge carrier recombination in TiO₂. Hence, the following chapters illustrate the basic processes happening during photocatalysis and photocatalytic NO degradation.

2.1.1 Basic processes of semiconductor photocatalysis

Typically, semiconductor materials with bandgap energies E_{BG} ranging from 1.6 to 4 eV are employed as photocatalysts.^{12,44–46} The energy of the light corresponds to UV-Vis or NIR light. The photocatalytic process is schematically depicted in **Figure 2.1**.

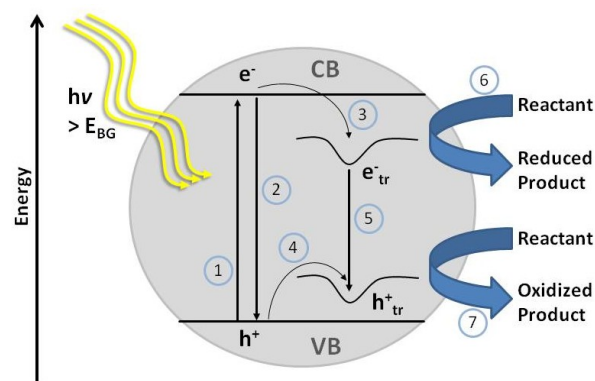


Figure 2.1: Schematic illustration of the photocatalytic reaction in a semiconductor particle.

The following steps are assigned to a photocatalytic reaction on semiconductor surfaces:^{14,47–49} Absorption of light exceeding the bandgap energy promotes electrons e^- from the valence band VB into the conduction band CB (1). The remaining vacancy is described as a hole h^+ . The photo-generated charge carriers can recombine directly (2), or

2. Theoretical background

move to the surface or internal defects, where the charge carriers are stabilized at different trapping sites (3 and 4). The stabilized charge carriers can recombine with other trapped charge carriers (5) or with mobile free charge carriers (not shown). Moreover, the transfer of trapped electrons e^-_{tr} to adsorbed molecules can induce a reduction reaction on the surface on the semiconductor (6) and the charge transfer from adsorbed species to trapped holes h^+_{tr} describes an oxidation process (7). A direct oxidation by valence band holes or a direct reduction by conduction band electrons are possible as well (not shown).^{50,51}

2.1.2 Titanium dioxide

TiO₂ is a large bandgap semiconductor with bandgap values ranging from 3.0 to 3.4 eV.^{52,53} The bandgap of the semiconductor represents the energetic distance between the valence band (VB) and the conduction band (CB) and its value depends on the crystal structure. The four commonly known polymorphs available under standard conditions are: rutile, anatase, brookite, and TiO₂ (B).^{54,55} The most thermodynamically stable phase at room temperature is rutile, resulting in a conversion of all metastable phases to rutile above temperatures of 500-600 °C.⁵⁶ Anatase and rutile have a tetragonal structure and consist of TiO₆ octahedra.⁵⁷ In the rutile phase the octahedra are connected via shared corners and the anatase phase is composed of edge-sharing octahedra (cf. **Figure 2.2**).

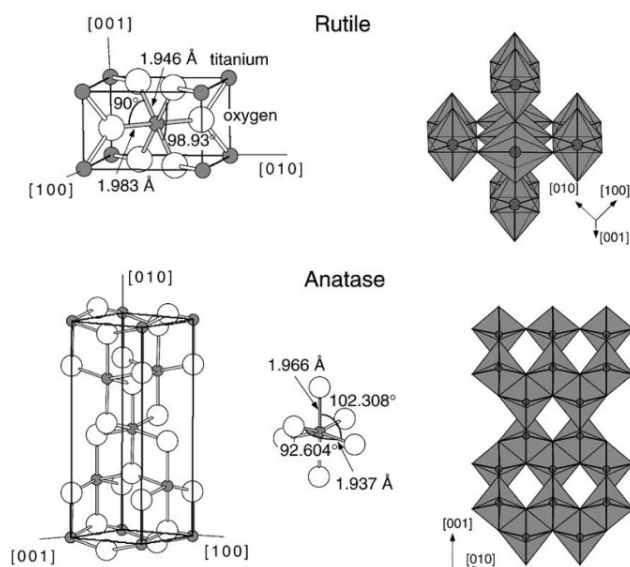


Figure 2.2: Unit cell and crystal structure of rutile and anatase. Reprinted with permission from Ref. 57.

Anatase is typically described as the most photocatalytically active phase.⁴⁷ The higher photocatalytic activity of anatase can be related to its high electron mobility, low dielectric

constant, higher Fermi level, high degree of hydroxylation, and lower capacity for the adsorption of molecular oxygen in comparison to the other phases.^{55,58,59}

As described in the introduction, one of the main benefits of TiO₂ is its great potential for the photocatalytic degradation of several organic and inorganic chemicals in air and water.^{12,14-16} Since the degradation of such compounds is carried out at the interphase between the bulk semiconductor and the gaseous or liquid surrounding, this interphase needs to be maximized.⁶⁰ The simplest approach to achieve such a high surface area is through the utilization of small particles. Small anatase particles can be synthesized by several strategies including bottom-up approaches, such as sol-gel and hydrothermal synthesis, and top-down approaches, including milling or laser ablation.⁴⁷

In addition to the photo stability of TiO₂ and its inert character, the non-toxicity is a huge advantage in comparison to many potential photocatalysts.¹⁴ Nevertheless, several publications question the non-toxic character of TiO₂. For example, Hall *et al.* recently reported an acute toxicity of TiO₂ on cladocerans and algae.⁶¹ However, the observed effect is caused by the omnidirectional processes of the reactive oxygen species (ROS) formed on the TiO₂ surface under illumination. In the absence of light the non-toxic character of TiO₂ is usually confirmed.⁶² These difficulties and pitfalls of photo toxicity in typical toxicity assays were discussed in detail by Friehs *et al.*⁶³ The authors stressed that “in vivo studies in higher animals, which would allow conclusions regarding the risk of photo induced toxicity to humans, are extremely rare.” They concluded, furthermore, that for a sufficient analysis of the risk potential, realistic illumination intensities and particle concentrations must be selected in future biologic assays.

Trapping of charge carriers in TiO₂

Photocatalytic reactions on the surface of TiO₂ proceed in the picosecond to second time-scale.⁶⁴⁻⁶⁶ The basic processes inside the semiconductor, on the other hand, such as charge carrier generation and charge carrier trapping, partially proceed faster and elapse in femtoseconds or nanoseconds (cf. **Figure 2.3**).^{32,67}

Typically, more than 90 % of the charge carriers recombine within 10 ns.²² The high probability for the bulk recombination of the photo-generated electrons and holes is seen as the major cause for the relatively low photocatalytic performance of pure TiO₂.⁶⁸ The trapped charge carriers mainly possess a lifetime long enough to efficiently drive

2. Theoretical background

photocatalytic reactions on the surface.⁵¹ Subsequently, the trapping reactions are processes of the utmost importance for the photocatalytic performance of a photocatalyst, since they increase the lifetime of charge carriers.

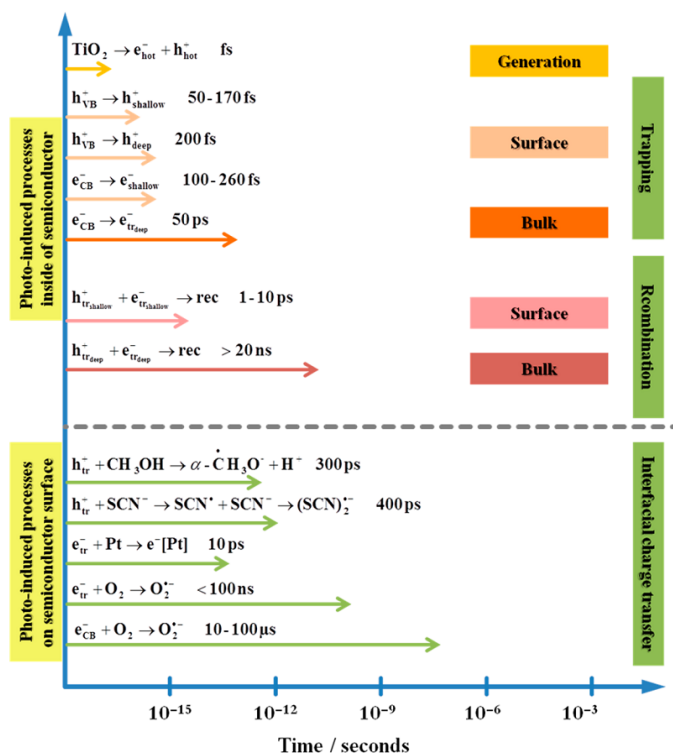


Figure 2.3: Schematic illustration of the time-scales of photocatalytic reactions in the bulk and at the surface of TiO₂. Reprinted with permission from Ref. 47. Copyright 2014 ACS.

Despite the beneficial prolongation of the charge carrier lifetime, trapping of the photo-generated charge carriers can also reduce the reactivity of the trapped species.⁴⁷ Bahnemann *et al.*, for instance, reported that some trapped hole species in TiO₂ are incapable of oxidizing adsorbed anions, which are usually oxidized in photocatalytic reactions on TiO₂ surfaces.⁶⁹ Hence, stabilization of the charge carriers at trapping sites can be essential for the prevention of charge carrier recombination, but decreases the inherent energetic driving force for the photocatalytic reactions.

The photo excitation of electrons into the conduction band is a femtosecond process.⁶⁷ The trapping processes occurring afterwards can be subdivided into fast surface trapping of both types of charge carriers and slower deep electron trapping in the bulk. For instance, the formation of shallow hole traps on the surface requires only 50 fs,⁷⁰ while the relaxation of shallowly trapped electrons to deeply trapped electrons in the bulk proceeds in 0.5 fs.⁶⁷

Chemically, the trapped electrons and holes at the surface are assigned to Ti^{3+} centers and $\cdot OH$ radicals, respectively.⁴⁷ The $\cdot OH$ radicals are products of the oxidation of surface OH groups and the Ti^{3+} centers are generated by the formal reduction of Ti^{4+} ions (cf. **Eqs. 2.1** and **2.2**).



Typically, photocatalytic reactions, for instance in photocatalytic air treatment, are carried out in the presence of molecular oxygen. The conduction band electrons and the trapped electrons (Ti^{3+} centers) react with molecular oxygen forming superoxide radical anions, since the redox potential of the conduction band electrons in TiO_2 is negative enough (-0.52 V vs. NHE) (**Equation 2.3**).⁷¹



Oxygen-based radicals formed upon illumination of photocatalysts, such as superoxide radicals, singlet oxygen, peroxides and $\cdot OH$ radicals, are summarized as ROS.^{20,72} Consequently, the two phrases “trapped charge carriers” and “ROS” are in many cases identical for TiO_2 . These ROS are typically formed on the surface of a photocatalyst under illumination in the presence of molecular oxygen and water (water vapor or surface adsorbed water) and, together with free charge carriers, the ROS initiate photocatalytic reactions.⁵⁰

2.1.3 Photocatalytic NO_x degradation employing TiO_2

As mentioned in the introduction, high NO_x concentrations are harmful to human health and lead to global warming.^{1,3} Nitrous oxide is especially responsible for changes in the climate due to secondary processes like ozone depletion.^{3,73,74} The growing demand for personal mobility worldwide and the slow development of alternatives like full electric vehicles render fast improvements of the environmental conditions in urban areas highly unlikely.^{75,76} Hence, photocatalytic air purification employing TiO_2 represents a viable alternative for the reduction of NO_x concentration in the atmosphere.⁴⁰ For the sake of completeness, it should be mentioned here that photocatalytic air treatment is not tackling the problem of air pollution at its core. In the end, the formation of volatile toxic substances in engines should be avoided, since the complete removal of released volatile

2. Theoretical background

compounds by photocatalysis is technically hardly possible due to limited mass transport to the catalyst surface.^{77–79}

In case of the NO degradation, NO₂ is formed as one of the intermediates and the final product is nitric acid HNO₃ (**Equation 2.4**).⁸⁰



The fate of the atmospheric NO is always the formation of nitrate species, because next to the photocatalytic reaction, the non-photocatalytic oxidation of NO_x to HNO₃ occurs in the atmosphere as well.⁸¹ The nitrates being formed by the oxidation of NO are removed from the atmosphere by rainwater. The nitric acid is indeed the main chemical compound responsible for acid rain, next to sulfur dioxide.⁸¹ Nevertheless, the nitrate salts formed from the nitric acid have a much lower toxicity compared to the NO_x species generated during the redox processes yielding NO. Furthermore, nitrates serve as agricultural fertilizers and are used on a technical scale worldwide.⁴ The fraction of nitrates detected in subterranean water coming from the atmosphere is small compared to the fraction derived from agricultural land use. In 2015, more than 75 % of the NO_x emissions in the US came from agricultural soil management, which includes the use of synthetic and organic fertilizers.⁴ An overview of the complex reaction mechanism of the photocatalytic NO degradation is shown in **Figure 2.4**.^{82,83}

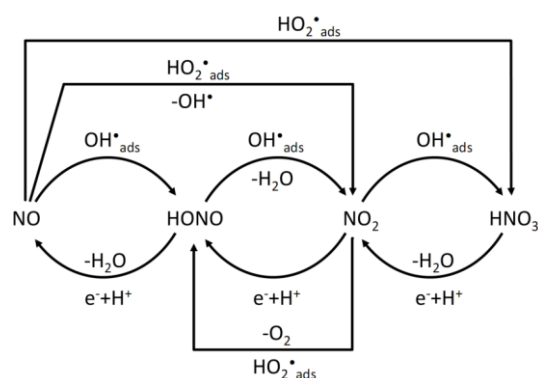


Figure 2.4: Pathways of the photocatalytic degradation of NO on TiO₂ under UV-light illumination. Instead of adsorbed [•]OH radicals the oxidation steps can be carried out by valence band holes as well. Similarly, the reduction reactions can be carried out via Ti³⁺ species. Furthermore, the different nitrogen oxides are partially adsorbed in the TiO₂ surface. The image has been adapted from Ref. 82.

The application of photocatalysts for photocatalytic NO degradation requires a certain understanding of the interactions between the materials used for the fabrication of

construction materials and the photocatalytic process on the surface of TiO_2 . Hence, numerous studies have been performed elucidating the effects of different materials in the photocatalytic air treatment. For instance, Mills and Elouali reported recently that an accumulation of NO_3^- on the TiO_2 surface during the course of the NO degradation reduces HNO_3 formation.⁸⁴ The authors reported that there is an equilibrium between NO_2 and NO_3^- on the surface of TiO_2 . When the surface is saturated completely with nitrate, no more nitrate is being formed and the photocatalyst solely converts NO to NO_2 . Apart from the discussions about nitrate on the surface of TiO_2 , the effects of other ions on the photocatalytic reaction have been studied. For instance, the presence of carbonate ions on the surface has been reported to increase the photocatalytic efficiency of TiO_2 .⁸⁵ However, the photocatalytic activities of TiO_2 -based materials for the NO_x degradation remain relatively small; subsequently, the efficient removal of NO_x from ambient air requires the utilization of large surfaces, for instance the surface area of construction materials.^{23,40,86}

Application in construction materials

TiO_2 is a widely studied and applied photocatalyst, since it fulfills many of the requirements for large scale applications.⁴⁷ However, as indicated above, the photocatalytic activity of TiO_2 for NO degradation is rather small. To overcome the drawback of the low photocatalytic performance of pure TiO_2 , the surface area of construction materials can be utilized, which are available on a large scale.⁷⁹ Numerous TiO_2 -composite materials with various additives have been employed in large-scale applications for the conversion of anthropogenic NO_x . The degradation of NO_x has been carried out on the surfaces of roof tiles, concrete,⁸⁷ paints,⁸⁸ pavement stones,⁸⁹ and mortar panels.⁸⁶

Interestingly, diverging results have been found for the NO_x reduction in real scale applications. Several studies reported a reduction of the NO_x concentration in the ambient atmosphere in the order of 19 to 80 %.⁸⁹⁻⁹¹ However, other studies revealed no detectable NO_x reduction.^{24,92,93} These differences might be related to diverging experimental characteristics such as the properties of the chosen photocatalysts (like the photocatalytic activity or the surface area), geometrical characteristics of the samples, differences in the climatic conditions, or the sampling time and rate.⁹⁴ The observed results can also be influenced by the support of the photocatalyst⁹⁵ or the matrix of the construction material.⁹⁶ Additionally, poisoning of the photocatalyst, for instance, could be responsible for the low observed photocatalytic performances and can occur by the adsorption of compounds from

the environment or by substances derived from the matrix. Therefore, the effect of every intermediate and chemical present on or close to the TiO₂ surface should be investigated.

The study of the interactions between single additives and TiO₂ should facilitate a deeper understanding required for the fabrication of TiO₂-composites with higher photocatalytic activities. However, the interplay of the employed additives and the photocatalytic processes has rarely been studied. The studies found in the literature show contradictory results even for the presence of simple ionic species.^{26,37,38,97} Barndock *et al.*, for instance, detected no influence of carbonate ions on the photocatalytic phenol oxidation by TiO₂.³⁸ Budarz *et al.*, on the other hand, reported that carbonate ions are strongly adsorbed on the TiO₂ surface leading to a strong inhibition of the photocatalytic iodide oxidation.³⁷ In addition to these conflicting findings, the photocatalytic studies listed above have been performed in TiO₂ suspensions. Since the photocatalytic process is highly substrate specific, the transferability of the observed results to the gas phase degradation of NO remains ambiguous.³⁹

2.2 Kinetic analysis of charge carrier recombination

The analysis of charge carrier kinetics is of the utmost importance for the application of semiconductor devices in photocatalytic, photo electrochemical, and photovoltaic reactions.^{27,47,98,99} The photocatalytic reaction, for instance, is only observed when the photo-generated charge carriers are able to reach the surface by diffusion. Similarly, a photovoltaic device requires a sufficient charge carrier diffusion length for the generation of a photocurrent.²⁷ Hematite, an iron(III) oxide modification, is an example for a semiconductor possessing a very short charge carrier lifetime, resulting in its poor photocatalytic performance in direct comparison to the use of titanium dioxide.^{31,100} Consequently, for every newly developed photoactive material the charge carrier concentrations and lifetimes should be compared and analyzed with the help of fit functions. Nevertheless, it remains difficult to achieve meaningful kinetic fit parameters if the applied fit model does not match the physical processes happening in the semiconductor. Hence, it is virtually impossible to know whether varying results are contradictory or caused by the observation of fundamentally different basic reactions.

2.2.1 Transient absorption spectroscopy (TAS)

A deeper understanding of transient phenomena in semiconductors is crucial for the development of new photocatalysts with improved properties. For instance, a higher charge carrier concentration and longer charge carrier lifetime is expected to increase the photocatalytic degradation rate of pollutants. Transient absorption spectroscopy (TAS) is a feasible technique for the detection of charge carriers, which facilitates a deeper insight into the basic processes of the photocatalytic reaction.^{28,35} Upon illumination, transient species are generated in the semiconductor, changing the optical properties of the sample. The optical changes are detected spectroscopically. In 1981, Wilkinson adapted the setup of TAS to optically dense powder samples (**Figure 2.5**).^{29,101} This enabled the time-resolved analysis of photo induced reactions occurring on powder surfaces, such as photocatalytic reactions on the surface of TiO₂. Furthermore, a large number of studies show that TAS is a viable tool for the analysis of charge carrier dynamics in semiconductor materials in time domains ranging from femtoseconds^{32,35} to seconds.¹⁰²

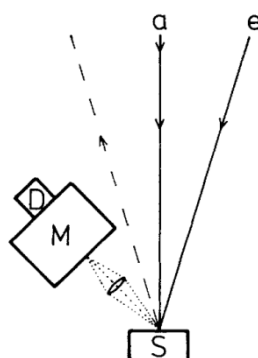


Figure 2.5: Schematic illustration of the TAS diffuse reflectance setup. a, analyzing light; e, excitation light; S, sample; M, monochromator; D, detector. The image has been reproduced from Ref. 101.

TAS is not the only tool that has been employed for the analysis of charge carrier kinetics. In fact, different techniques have been utilized in the last decades to study charge carrier kinetics, including, photoluminescence (PL)^{103,104} and time resolved microwave conductivity (TRMC).^{105–107} PL originates from the radiative recombination of photo-generated charge carriers. The PL signals can be released either by direct band–band transition (direct recombination) or by the transfer of trapped electrons to the valence band.¹⁰⁴ The corresponding signals of the transfer of these shallowly trapped electrons are observed in the visible region and the associated defects of the crystal structure are energetically located slightly below the conduction band.¹⁰³ Apart from PL, the TRMC

enables the detection of the mobile free charge carrier concentration in the material.¹⁰⁵ However, in contrast to the optical studies with laser flash photolysis spectroscopy, no direct information about the trapped charge carriers is usually obtained.

Generally, most studies lack a connection between the obtained kinetic parameters, like charge carrier lifetime or charge carrier concentration, and the physical properties of the photocatalyst, such as particle size or crystallinity. Often, the characterization of samples is solely carried out by the comparison of the height of the charge carrier signals under varied experimental conditions without the utilization of a fit function.³⁵ In the future, this method should be replaced by a detailed kinetic analysis of the decaying charge carrier signals, which would facilitate a deeper understanding of the underlying processes.

Transient signals in TiO₂

The transient absorption signals of photo-generated charge carriers in TiO₂ had already been observed by Henglein *et al.* in 1982.¹⁰⁸ However, the correlation of the transient absorption signals with specific excited states still remains challenging today. Furthermore, the respective chemical identities are still discussed controversially. The recent review article by Schneider *et al.* summarizes the assignments between transient absorption signals and charge carriers in TiO₂ made in the literature so far.⁴⁷ The findings of Yoshihara *et al.*¹⁰⁹ agree with most of the studies listed by Schneider *et al.*:⁴⁷ photo-generated holes are located around 400 to 550 nm, while photo-generated trapped electrons are observed between 620 and 800 nm (**Figure 2.6**).

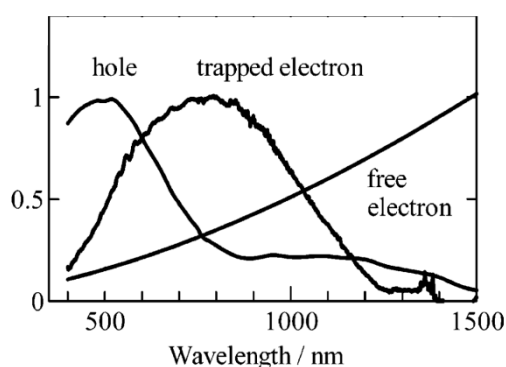
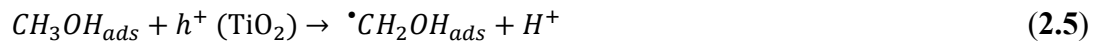


Figure 2.6: Transient absorption spectra of photo-generated electrons and holes in TiO₂. Adapted with permission from Ref. 109. Copyright 2004 ACS.

The broad transient absorption bands (cf. **Figure 2.6**) of the charge carrier species can be explained by the coexistence of several trap states. The trapped hole species are either

located at bridging oxygen atoms or at surface $\cdot\text{OH}$ radicals.^{47,110} Recently, Zawadski simulated transient absorption spectra of trapped holes in anatase employing DFT calculations.¹¹¹ These studies revealed signals of surface trapped holes at 350 to 550 nm, which is in agreement with the previously performed experimental studies.

For the individual observation of photo-generated electrons or photo-generated holes scavenger molecules have been employed. The scavenger molecules react with one of the charge carrier species and, hence, prevent fast charge recombination. Typically, methanol and molecular oxygen are applied as hole and electron scavengers, respectively, and nitrogen and argon atmospheres are used as reference conditions.^{28,35,47,69,109} In case of the photo-generated electrons, the above-mentioned wavelength areas of the transient absorption signals were detected in the presence of the hole scavenger methanol. The reaction of the methanol oxidation on the TiO_2 surface by photo-generated holes is shown in **Equation 2.5**.¹¹²



2.2.2 Second order kinetics

Monoexponential,³² double-exponential,³³ and second order^{14,30,34,35} decay functions have already been utilized to fit charge carrier recombination kinetics in TiO_2 . While exponential fit functions have mainly been used to fit exciton recombination, double-exponential and second order fit functions have also been used to explain the observed recombination kinetics of trapped charge carriers in the material.¹¹³ This chapter focuses on the second order processes, since the complex recombination of charge carriers in TiO_2 usually does not correlate with single exponential decays.^{34,114,115} Moreover, the multi-exponential fit functions have the inherent disadvantage of their uncertainty about the physical meaning of the modeled constants.⁷⁰

The second order fit function, on the other hand, is based on the bimolecular reaction of two species $A+B$, such as, photo-generated electrons and photo-generated holes.¹¹⁶



The reaction rate of the second order reaction is defined as the change in the concentration of the reactants over the course of time.

2. Theoretical background

$$rate = \frac{-d[A]}{dt} = \frac{-d[B]}{dt} \quad (2.7)$$

In the case of the formation of photo-generated electrons and holes, it can be assumed that the concentration of both species is identical at all times ($[A] = [B]$). Furthermore, the reaction rate can be expressed with the help of the rate constant k_2 .

$$rate = \frac{-d[A]}{dt} = k_2[A][B] = k_2[A]^2 \quad (2.8)$$

The integration of the rate equation results in:

$$\frac{1}{[A]} = k_2 t + \frac{1}{[A_0]} \quad (2.9)$$

$$[A] = \frac{[A_0]}{1 + [A_0]k_2 t} \quad (2.10)$$

The linearization shown in **Equation 2.9** can be used for the assessment of the suitability of a second order fit function. Therefore, the experimental data is plotted as inverse concentration $1/c$ against the time t . The plot reveals a linear trend, where the slope represents the second order rate constant k , if simple second order reaction kinetics is observed. In 2008, Katoh *et al.* performed this kinetic analysis for the transient absorption signal of a rutile single crystal in the time domain from 0 to 25 ns, after excitation with 2.8 mJ/cm^2 (**Figure 2.7**).¹¹⁴

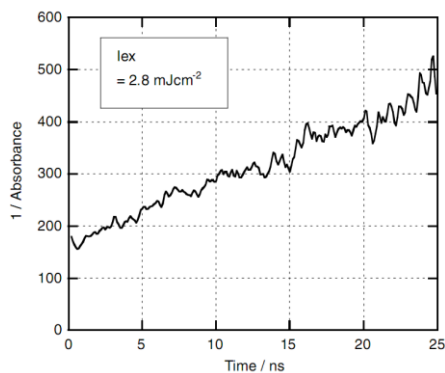


Figure 2.7: Reciprocal absorbance at 850 nm of rutile after excitation with 2.8 mJ/cm^2 . Reprinted with permission from Ref. 114.

Unfortunately, second order kinetic fits, including a rather arbitrary chosen baseline, are generally employed for the analysis of the charge carrier recombination due to the unavailability of alternatives.^{22,30,35} In 1995, Serpone *et al.* already observed a long-lived fraction of the transient signal observed for TiO_2 and employed a second order function with baseline.²² The authors related this long-lasting signal to the deeply trapped electrons.

Recently, Schneider *et al.* reported a permanent optical change of TiO₂ after laser excitation.¹¹⁷ This irreversible damage of a sample, employing a respective energy intensity of 7-60 mJ/cm², may also account for the long-lived signals observed in the transient reflectance spectroscopy. Overall, this baseline is used to mask the long-lasting components of the signal, which exhibit a more complex behavior diverging from pure second order kinetics.³⁶

However, Grela and Colussi reported that the charge carrier recombination in colloidal TiO₂ samples cannot be represented by second-order kinetics in all time-scales.³⁶ The observed second-order rate constants were found to depend on both the laser intensity and the chosen time window. Therefore, the second order fit with baseline does not represent an ideal model for application on charge carrier recombination in TiO₂, if correct and comparable results should be achieved.

2.2.3 Fractal kinetics

Fractal models for the kinetic analysis are derived from the concept of fractal geometry. Such models have already been used frequently for the analysis of several experimental observations. For instance, the dielectric response of TiO₂¹¹⁸ or the decay of trapped electrons in the form of O₂⁻ on the surface of TiO₂.¹¹⁹ In addition, fractal models were used for reactions on the surface of TiO₂, such as the dehydrogenation of methanol^{112,120} and the photo desorption of O₂.¹²¹

The first description of fractals in natural sciences was given by Mandelbrot in 1983.¹²² Mandelbrot reported that natural phenomena, such as the line of the seacoast or Brownian motion, can be described with the help of fractal geometry. Also in 1983, Pfeifer and Avnir discussed the application of the fractal theory on heterogeneous surfaces.^{122,123} Generally speaking, fractals are objects with effective “fractal” dimensions that are not identical with the 1, 2 or 3 dimensions of the Euclidean space. The underlying structure or geometry has a large impact on chemical reactions on heterogeneous surfaces, since the reactants need to diffuse to each other. In this case, bimolecular chemical reactions, such as the charge carrier recombination on such heterogeneous surfaces, display different kinetics as compared to similar reactions carried out in solution. The reason for the observed phenomena is the geometrical diffusion limitation causing the segregation of the charge carriers.¹²⁴

2. Theoretical background

Since the diffusion of the reagents into the liquid/gaseous environment or into the bulk of the semiconductor particle is not possible, the reaction is carried out on a structured two-dimensional surface instead of a free three-dimensional space. **Figure 2.8A** illustrates this limited diffusion for a random walk on a fractal surface. The geometrical diffusion limitation can even result in apparent one-dimensional reaction kinetics for some nanostructured surfaces or in pores.¹¹⁶ Heterogeneous TiO₂ powder surfaces have relatively large variations in topography, bearing catalytic islands and possessing irregularly distributed trapping sites.¹²⁵ Therefore, the surface combines a nanostructure, governed by the particle size and shape, with a microstructure, generated by the agglomeration of the particles. **Figure 2.8B** shows an example of the TiO₂ microstructure obtained after drying of a TiO₂ paste. Furthermore, in **Figure 2.8C** a network of agglomerated TiO₂ particles is shown as an example for the mentioned nanostructure.

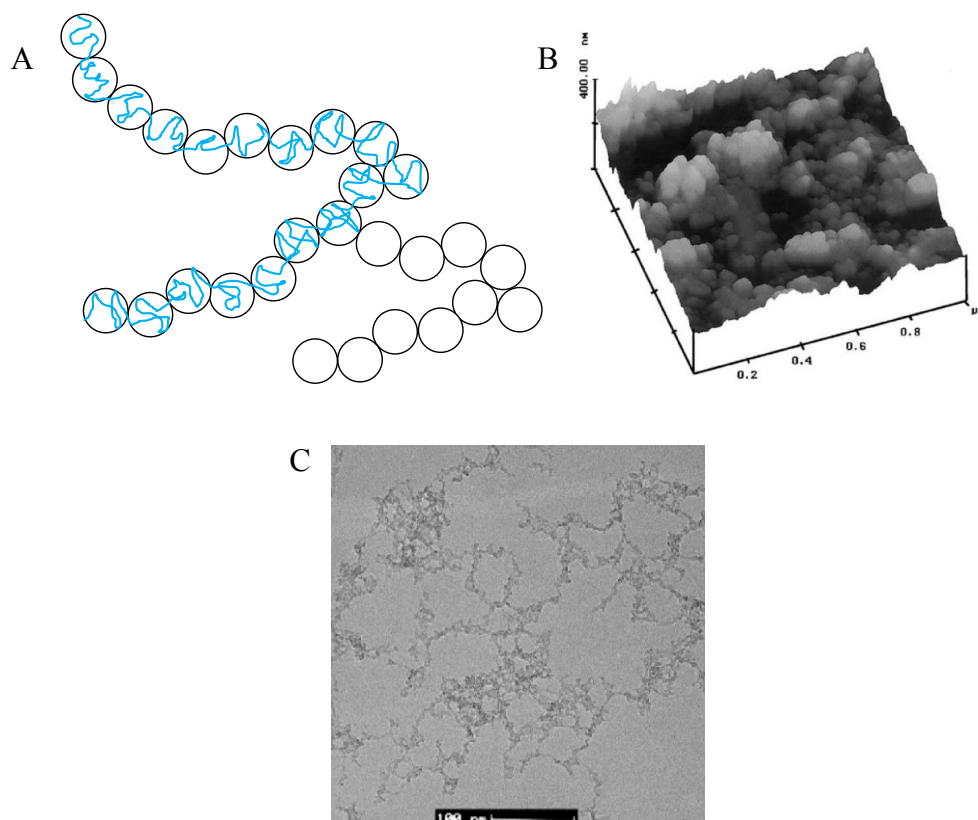


Figure 2.8: Schematic view of a fractal surface (black circles) and random pathway of a charge carrier (blue line) (A) and AFM 3D image of a doctor-blade TiO₂ film (B) and TEM image of a network formed by platinized TiO₂ (C). Adapted from Ref. 124 and reproduced from Ref. 125 and 126, respectively.

The impact of fractal structures on reaction kinetics was already reported by Kopelman in 1988.¹¹⁶ According to the work of Kopelman, the rate constant k should be replaced by the

fractal rate coefficient k_f for batch reactions on fractal surfaces. The fractal rate coefficient represents the product of the fractal recombination constant $k_{2,f}$ multiplied by the time t to the power of $-h$ (**Equation 2.11**).¹¹⁶

$$k_f = k_{2,f} t^{-h} \quad 0 \leq h \leq 1 \quad (2.11)$$

The fractal parameter h is an indicator for the fractal dimension of the surface, limiting the diffusion of the observed species. In homogeneous media, such as reactions in solution or in the gas phase, classical time-independent kinetics are observed and the exponent is equal to zero ($h = 0$).¹¹⁶ Nevertheless, for reactions carried out on fractal surfaces the exponent differs from zero $h > 0$ and fractal-like kinetics are observed. Typical values for h of fractal surfaces are between $h = \frac{1}{3}$ and $h = \frac{1}{2}$.¹¹⁶ If the fractal parameter is equal to 0.5 ($h = \frac{1}{2}$), the diffusion limitation of the fractal substructure is identical to the diffusion in a one-dimensional pore system.¹¹⁶

Fractal models are rarely applied for the analysis of charge carrier recombination dynamics. Nonetheless, Grela and Colussi reported that stochastic calculations in 2D lattices modeling the recombination of photo-generated electrons and holes reveal a change in the second order rate coefficient, which can be explained by fractal kinetics.³⁶ The kinetic model of Grela and Colussi shows that the initially uniform distribution of charge carriers follows the above-described segregation process and leads to non-classical kinetic behavior. Hence, the recombination kinetics of charge carriers can be related to stochastic surface events.

2.2.4 Power law decays

Apart from the previously discussed fit functions, a different approach has been suggested by Schindler and Kunst in 1990.¹¹⁵ Based on the observations of Tachiya and Mozumder¹²⁷, who reported power law recombination kinetics for specific electron tunneling processes, a power law was used to fit transient photoconductivity (TRMC) decays observed for TiO₂.¹¹⁵ The multiple trapping and detrapping processes of photo-generated electrons were reported to be responsible for the power law decay kinetics in TiO₂ particles.¹²⁸

2. Theoretical background

The linearization of the power law kinetics can be achieved by double logarithmic plotting.

Figure 2.9 illustrates such a double logarithmic plot of reported power law decays in untreated and platinized TiO₂ (P25, Degussa).

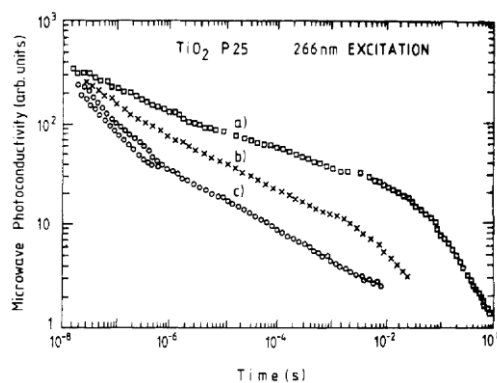


Figure 2.9: Transient photoconductivity of TiO₂ powder (P25) after laser excitation ($\lambda_{ex} = 266 \text{ nm}$; $0.5\text{-}1 \text{ mJ/cm}^2$). (a) untreated P25; (b) platinized P25 treated with 2-propanol; (c) platinized P25. Reproduced from Ref. 115.

However, the physical background of the photoconductivity measurements is not identical to the basic processes observed in transient absorption studies. In 2010 Shuttle *et al.* reported a model resulting in power law decays of the transient absorption signals of the charge carriers.¹²⁹ The results were derived from an exponential distribution of trapped states in the bandgap.¹³⁰ Furthermore, the authors made the assumption that the trapped hole species are immobile and that the effective charge carrier mobility depends on the charge density.^{128,129,131} The power law model presumes further that at significantly long periods of time after the excitation, the mechanism of charge carrier recombination is influenced only by the energetic distribution of the trap states. This model has mostly been applied for studies employing very low laser intensities and investigating charge carrier signals microseconds to seconds after excitation.^{31,131,132} The fitting of entire transient photoluminescence signals by Wang *et al.*, consequently, could be achieved using a combination of a power law decay and an exponential decay curve.¹³³ In 2008 Tang *et al.* reported likewise that at low laser intensities power law decay kinetics and at reasonable higher excitation intensities monoexponential recombination kinetics are observed in TiO₂.¹³¹

3. Materials and experimental methods

3.1 Materials

Commercial TiO₂

The properties and suppliers of the TiO₂ (anatase) powder samples are listed in **Table 3.1**. The ultrasound pretreatment has been carried out employing ultrapure water (Milli-Q, EMD Millipore) and ethanol (Carl Roth GmbH & Co. KG; 99.8% with 1 % MEK). All chemicals were used as received without further purification.

Table 3.1: Suppliers, average particle sizes and Brunauer-Emmet-Teller (BET) surface areas of the commercial TiO₂ materials.

Material	Supplier	Average particle size*	BET surface area
		/ nm	/ m ² /g
PC500	Cristal (Tronox)	7	305
KronoClean7050	KRONOS	15	250
	International Inc.		
PC105	Cristal (Tronox)	17	78
Kronos1001	KRONOS	125	10
	International Inc.		

* the average particle size was given by the supplier and was confirmed by TEM imaging

TiO₂-additive powder samples

TiO₂ (KronoClean7050, anatase) was ground with one of the following materials: BaSO₄ (Sigma-Aldrich; 99 %), CaCO₃ (Sigma-Aldrich; 98 %, <30 μm particle size), Na₂CO₃ (Sigma-Aldrich; >99.5 %).

3.2 Preparation

The following procedures for the preparation of the TiO₂ powder samples have already been published by the author in the references 48, 134, and 135. However, a complete overview of the employed methods is given here as a summary and the respective original publications are indicated by the references next to the headlines.

3. Materials and experimental methods

Cleaning method of the pure and mixed TiO₂ powder samples^{48,134}

Prior to the laser flash photolysis experiments, the pure TiO₂ samples were treated with the following ultrasound cleaning procedure: TiO₂ (Kronos1001, PC105, or PC500) was added to an aqueous ethanolic solution (10 vol.-% ethanol, 10 g/L TiO₂) and subjected to 8 min ultrasound treatment (340 W/L). The solid particles were separated by centrifugation (6 h, 500 rpm) and subsequent sedimentation (overnight). Finally, the precipitates were collected and stored at 100 °C overnight.

Mixed TiO₂ powder samples⁴⁸

TiO₂ samples with binary particle size distribution were prepared by the deposition of small particles, PC105 or PC500, on the large spherical Kronos1001 particles. According to the above-described ultrasound procedure, two series of new materials were obtained: Kronos1001 combined with 0.4, 5, 20, 40, and 70 wt.% of PC105 or PC500. To achieve a good mixing of the TiO₂ samples, the ultrasound procedure was separated into two parts (**Figure 3.1**). In the first step, PC105 or PC500 was added to an aqueous ethanolic solution (10 vol.-% ethanol) and subjected to 5 min ultrasound treatment (340 W/L). The sonication was not interrupted for the second step in which the larger particles (Kronos1001) were added. A final concentration of 10 g/L TiO₂ was achieved by the addition of Kronos1001 and the ultrasound processing of the mixed TiO₂ suspension was extended for a further 3 min. The reference materials, namely the pure Kronos1001, PC105, and PC500, were treated in the same manner.

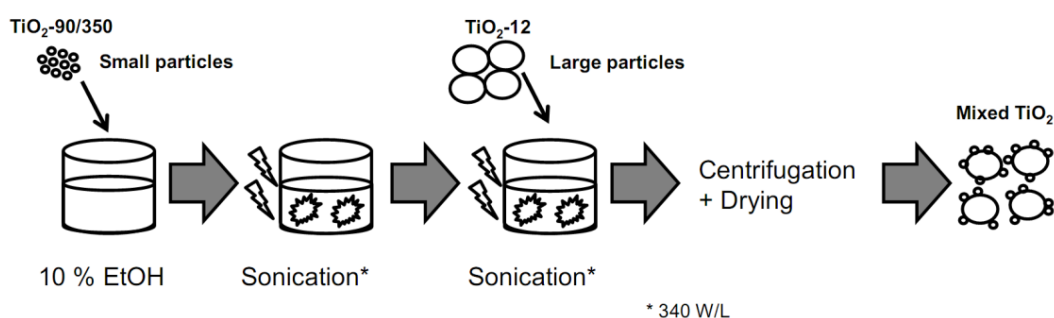


Figure 3.1: Two-step ultrasound treatment for the synthesis of TiO₂ samples with binary particle size distribution (mixed TiO₂). Reprinted from Ref. 48.

TiO₂-additive samples¹³⁵

The synthesis of the TiO₂-additive samples was carried out without any ultrasound cleaning or mixing procedure. The employed TiO₂ powders were achieved by 15 min

grinding of TiO₂ (KronoClean 7050) with one of the additives (BaSO₄, CaCO₃, Na₂CO₃). The volume ratios of the mixed powder samples were determined employing the powder densities of the TiO₂ and the additives, respectively. The mixed TiO₂ samples are named according to the additives employed (TiO₂-additive).

TiO₂ paints

Six silicate based paints, containing the same weight fraction of TiO₂, were provided by a collaborating company. The paints differ according to the additives used and, subsequently, the overall composition varies slightly. Every sample contained a different additive and the paints were labeled according to the increased constitution of the following ions: lithium, iron, copper, zinc, and cobalt. The sixth sample contained none of the given additives and was used as a reference.

3.3 Instrumentation

The TiO₂ powder samples were sonicated with a Branson 450 Digital Sonifier (102-C Converter), centrifuged with a Kendro Megafuge 1.0 and dried in an oven (Memmert GmbH + Co. KG; BE 400). BET surface area measurements were carried out with a Micromeritics AutoMate 23. The photocatalytic removal of NO was performed according to ISO 22197-1:2011: HB 175 Lamp from Philips (4 x Philips Cleo 15 W, 365 nm); Flow meter B.V. Smart Mass Flow 5850S from Brooks Instrument; APNA 360 NO analyzer from Horiba. UV-Vis absorption measurements were acquired with a Cary 5000 Absorption Spectrophotometer from Agilent that was equipped with a diffuse reflectance accessory (DRA 2500; Agilent), external detector and integrating sphere. All absorption spectra were calculated from the fraction of non-reflected light (1-R) employing the highly UV reflective reference BaSO₄.^{136,137} Transient reflectance spectroscopy was carried out with an Applied Photophysics LKS 80 Laser Flash Photolysis Spectrometer coupled with an Nd-YAG laser (Quantel; Brilliant B; 3rd harmonic, 355 nm).

3.4 Experimental methods

3.4.1 Transient reflectance spectroscopy

Every sample was flushed with nitrogen gas for at least 30 min, prior to the transient reflectance measurements. The transient reflectance spectroscopy was performed in diffuse reflectance mode (**Figure 3.2**).

Table 3.2: Conditions of the experiments performed by means of transient reflectance spectroscopy. Reprinted from Ref. 134.

Total acquired time	10 μs	1 ms*
Laser frequency	1 Hz	10 Hz
Terminal resistance	50 Ω	5 k Ω
Xenon lamp	Pulsed	non-pulsed
Average shots	12 shots	200 shots
Time resolution	100 ps/point	100 ns/point*
Laser energy	1 mJ/cm ²	2 mJ/cm ²
Laser wavelength	355 nm	355 nm

* in case of the mixed TiO₂ samples with binary particle size and the TiO₂ paint samples the total acquired time was 200 μs resulting in a time resolution of 10 ns/point

The stated correlations include the assumption that during laser excitation the scattering properties of the sample remain constant. **Figure 3.3** shows the absorbance raw data of PC105 in the time-scale of 10 μs as an example.

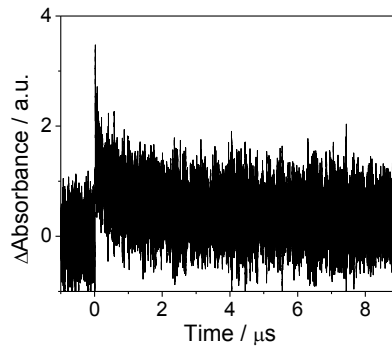


Figure 3.3: Transient absorbance of charge carriers photo-generated in PC105 measured at 500 nm following a 1 mJ/cm² laser pulse with 355 nm (raw data; 10000 points; 10 μs). Reprinted from Ref. 134.

The acquired set of data points was reduced to 500 points by averaging 200 reflectance values to one data point, enabling an easier processing and mathematical fitting of the transient signals. Additionally, the change in reflectance ΔJ of the powder samples was calculated from the absorbance value (**Equation 3.2**):

$$\Delta J = 1 - 10^{-Abs} = \frac{I_0 - I}{I_0} \quad (3.2)$$

3. Materials and experimental methods

The change in reflectance represents the fraction of the light that is absorbed by the transient species.

Lin and Kan demonstrated in 1970 that the optical change in reflectance depends linearly on the concentration of the transient species, as long as the changes in reflectance are considerably small ($\Delta J < 10\%$).¹³⁹ **Figure 3.4** displays the processed transient data observed for PC105 in the 10 μs and the 1 ms time domain.

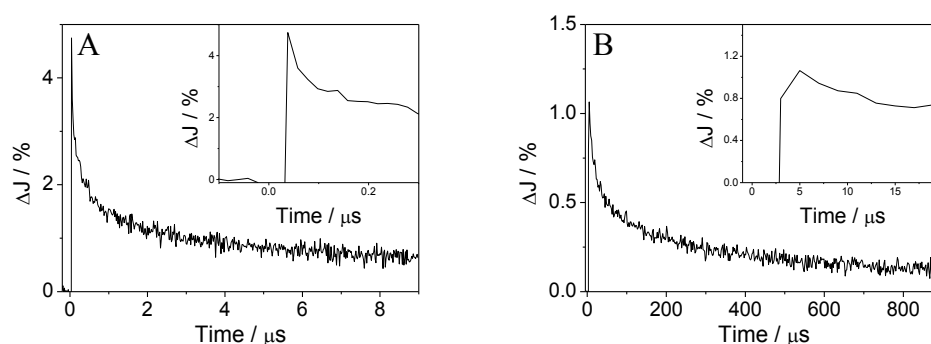


Figure 3.4: Transient reflectance signals of charge carriers photo-generated in PC105 (500 points) measured at 500 nm after laser excitation ($\lambda_{ex} = 355\text{ nm}$) observed over 10 μs (A) and 1 ms (B). The insets show the signals at the very beginning of each measurement. Images adapted from Ref. 134.

The inset of **Figure 3.4A** shows that the transient reflectance signal in the 10 μs measurement could be detected after 40 ns. The initial negative peak is related to scattering of the UV laser (6 ns FWHM), which was used as excitation source. The terminal resistance of 50 Ω facilitates a short rise time and allows the fast observation of the signal after 40 ns. The high resistance of 5 k Ω used for the 1 ms measurement leads to a much longer rise time for the detector. Accordingly, the first 5-6 μs of the measurement do not represent the real transient signal of TiO_2 and need to be removed before kinetic analysis.

For all the following calculations and figures, the charge carrier signals were analyzed after 40 ns for the 10 μs measurement and after the first 6 μs for the 1 ms measurement. The double logarithmic plot of the data in both time-scales (**Figure 3.5**) demonstrates that the same signal could be detected after normalization. In **Figure 3.5B** the results are shown after normalization. Normalization was carried out utilizing the overlapping region of 6-9 μs , where the charge carrier signals should be identical. Because of the different experimental conditions, in particular the varying laser intensity and the terminal resistance, the signals display a different height.

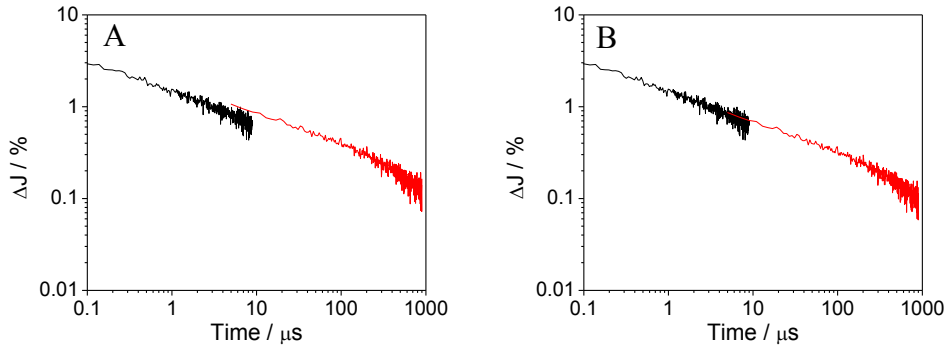


Figure 3.5: Double logarithmic plots of the transient reflectance signals of charge carriers photo-generated in PC105 ($\lambda_{ex} = 355 \text{ nm}$) measured at 500 nm observed over the two time-scales 10 μs (black) and 1 ms (red) (A) and signal after normalization (B). The images have been adapted from Ref. 134.

Subsequently, the signals were averaged in the overlapping time domain and the correction factor was employed on the results obtained in the 1 ms measurement. Hence, for the following kinetic analysis the normalization is generally considered.

3.4.2 Photocatalytic NO degradation

The photocatalytic degradation of gaseous NO has been carried out similar to the experimental procedure described in ISO 22197-1. However, the active surface area and the gas flow derived from the ISO conditions. The experimental characteristics were: Volume flow $\dot{V} = 5.0 \cdot 10^{-5} \frac{\text{m}^3}{\text{s}}$ and a geometrical surface area of the sample $A_{SA} = 9.61 \cdot 10^{-4} \text{ m}^2$. Gas bottles of NO in nitrogen (The Linde Group; 50 ppm NO in N_2) and compressed, oil-free air have been used. The detailed experimental procedure has been described elsewhere.⁴⁸

Prior to the analysis, all powder samples were treated with UV-light ($10 \frac{\text{W}}{\text{m}^2}$, 365 nm, Philips Cleo) for 72 hours and stored in vacuum-tight desiccators. Photocatalytic removal of NO (1 ppm NO in synthetic air) was detected under $10 \frac{\text{W}}{\text{m}^2}$ UV radiation (365 nm, Philips Cleo, monochromatic light has been assumed) and 40-50 % relative humidity. As an illustration of the experimental procedure, the NO concentration c_{NO} of pure TiO_2 in the course of the experiment is shown in **Figure 3.6**.

3. Materials and experimental methods

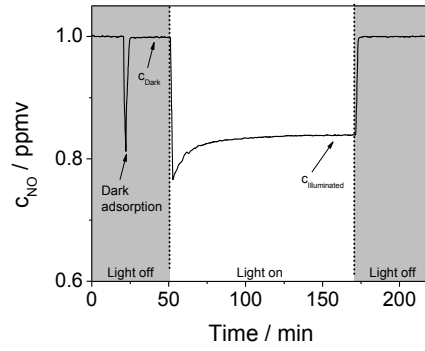


Figure 3.6: NO concentration during the photocatalytic NO degradation experiment employing pure TiO₂. Adapted from Ref. 48.

Under dark conditions the concentration of approximately 1 ppm NO was detected (c_{Dark}). The negative peak during the dark condition represents the dark adsorption of NO on the sample surface and was observed after changing the gas flow from bypass to reactor. Illumination of the samples with UV-light reduced the concentration of NO due to the photocatalytic degradation of NO. After 2 hours illumination the concentration of NO reached a constant value. The last 120 data points before the light was turned off were averaged to determine the concentration of NO under illumination $c_{Illumination}$. The difference between the two concentrations represents the fractional conversion of NO Δc_{NO} (**Equation 3.3**).

$$\Delta c_{NO} = c_{Dark} - c_{Illumination} \quad (3.3)$$

The obtained fractional conversion of NO was used to calculate the photonic efficiency ξ_{NO} (**Equation 3.4**).⁸²

$$\xi_{NO} = \frac{\Delta c_{NO} \cdot \dot{V} \cdot p \cdot N_A \cdot h \cdot c}{I \cdot \lambda \cdot R_C \cdot T \cdot A_{SA}} \quad (3.4)$$

The photonic efficiency considers the incident light intensity and, hence, does include the reflection and scattering of the sample surface. To analyze the photocatalytic activity normalized to the absorbed photons, the apparent quantum yield $\phi(365 \text{ nm})_{NO}$ was calculated with the fraction of absorbed light $(1 - R)$, where R represents the reflected light of the sample at 365 nm.¹⁴⁰

$$\phi(365 \text{ nm})_{NO} = \frac{\xi_{NO}}{1 - R} \quad (3.5)$$

4. Results

4.1 Pure TiO₂ samples

4.1.1 Transient reflectance spectra

Figure 4.1 illustrates a typical transient reflectance signal at 500 nm observed for TiO₂ (PC105) after excitation with a nanosecond UV-laser pulse.

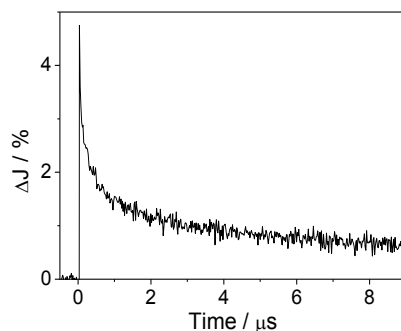


Figure 4.1: Transient reflectance signals of charge carriers photo-generated in N₂-saturated PC105 measured at 500 nm after laser excitation ($\lambda_{ex} = 355 \text{ nm}$; 1 mJ/cm² pulse energy).

The transient reflectance of anatase was detected and analyzed in two different time domains. The transient signals obtained in this study show a good correlation with the results reported in the literature; for instance, the signal heights and visual decay kinetics observed here agree with the findings of many reports.^{32,69,70} Furthermore, Wang *et al.* detected comparable transient signals of rutile and anatase in two separated time domains (10^{-5} to 1 s) as well.⁶⁵

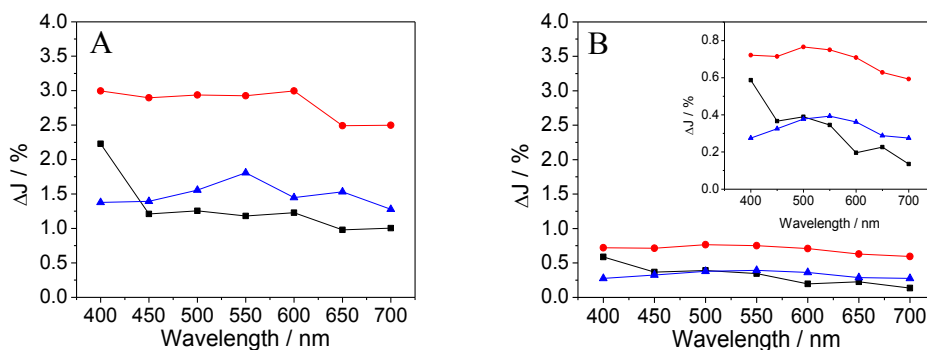


Figure 4.2: Transient reflectance spectra of charge carriers photo-generated in the three TiO₂ powder samples (Kronos1001 (black), PC105 (red), and PC500 (blue)) observed 0.1 μs (A) and 7 μs (B) after laser excitation. The inset shows a magnification of the spectrum. The image has been adapted from Ref. 134.

The transient reflectance signals were detected in the wavelength domain ranging from 400 to 700 nm. **Figure 4.2** shows the resulting transient reflectance spectra of the charge carriers photo-generated in the three commercial TiO₂ samples (Kronos1001, PC105, PC500) measured at 0.1 μ s and at 7 μ s after the laser excitation.

In good agreement with literature reporting that the trapped charge carrier species absorb light over a broad range of wavelengths,¹⁰⁹ all samples revealed a broad transient reflectance in the selected wavelength regime. If electron or hole scavengers had been applied, the transient reflectance bands of trapped holes would be expected at a lower wavelength between 400 and 500 nm and bands of trapped electrons would be expected at a higher wavelength ranging from 600 to 800 nm, respectively.⁴⁷ However, since the experiments were performed in an inert nitrogen atmosphere and no reagents or scavenger molecules were employed, no peak or band could be identified for the transient reflectance spectra between 400 and 700 nm. Consequently, the transient reflectance signals represent a sum of transient signals of trapped electron and trapped hole species.

According to Friedmann *et al.* the transient reflectance signal at 500 nm can be correlated to a 50:50 mixture of trapped electrons and trapped holes, since the reported absorption coefficients are nearly identical at this wavelength.¹⁴¹ Hence, the overlapping signal of multiple charge carrier species are observed. However, under the given inert conditions pure recombination kinetics is observed. Hence, discrimination between the different charge carriers is not required for the kinetic analysis of the charge carrier recombination. **Figure 4.2A** and **B** show that the broad signals decay with identical speed. Therefore, the transient reflectance signals at 500 nm were selected as representatives and analyzed with the help of the following fit functions.

4.1.2 Second order fit with baseline

Typically, the literature employs second order decay functions fitting the transient absorption signals.³⁵ The generally employed second order fit function is achieved following the hypothesis that both charge carrier species react only with each other and the same amount of electrons and holes is generated during the course of the laser excitation. Subsequently, the individual concentrations of the charge carriers are replaced by one concentration. Hence, the concentration of the charge carriers c decays from the initial concentration c_0 with the inherent second order rate constant k_2 . Based on **Equation 2.10**,

Equation 4.1 shows the respective second order fit function including the fitted parameters.

$$\Delta J = \frac{A}{1+Ak_2t} + B \quad (4.1)$$

The parameter A represents the beginning height of the transient signal. The parameter B represents the residual signal not matching the second order process and the second order decay constant k_2 is a measure for the recombination speed of the photo-generated charge carriers. To obtain **Equation 4.1**, a linear dependency of the optical change in reflectance on the concentration of the transient species has been adopted ($c \sim \Delta J$).^{139,142} Furthermore, the extinction coefficient of the transient species ε was set to $1 \frac{L}{mol \cdot cm}$ ($A = \varepsilon \cdot c, A = c$).

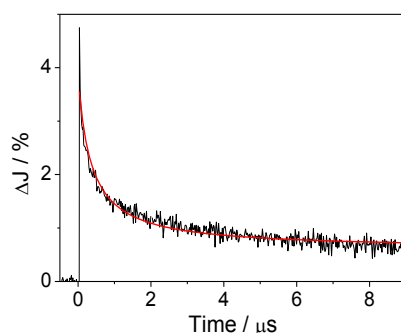


Figure 4.3: Transient reflectance signals of charge carriers photo-generated in N_2 -saturated PC105 measured at 500 nm after laser excitation with second order fit function (red).

As mentioned in the introduction, the baseline of the second order kinetics fit was correlated with the long-lived transient signals in TiO_2 .¹⁰³ Indeed, non-reactive trapped charge carriers⁶⁹ and permanent optical changes¹¹⁷ have been reported and can justify the application of a fit function including a baseline. **Figure 4.3** illustrates the second order fit function of **Equation 4.1** applied to the transient reflectance signal measured at 500 nm employing PC105.

The second order fit function shown in **Figure 4.3** does not fit the beginning height of the transient reflectance signal properly; further, the signal also derives from the course of data points at the end of the selected time frame. This still results in an adjusted coefficient of determination of 0.96 ($\bar{R}^2 = 0.96$). All fitting parameters of the second order fit applied to TiO_2 samples containing PC105 are listed in the appendix (**Table S1** and **Table S2**). The transient reflectance signals were detected in two time domains and, therefore, the fitting

process was carried out either for the full time-scale observed (**Table S1**) or for a part of the time-scale (**Table S2**).

Dependency of the second order fit on the selected time window

Equal to the findings of Grela and Colussi,³⁶ a dependence of the fitting results on the laser intensity and the selected time-scale was observed for the second order fit function applied to the transient reflectance signals of the photo-generated charge carriers in TiO₂ after laser excitation. For a solely second order process, the plot of the inverse charge carrier concentration $1/c$ against the time t should reveal a linear trend. **Figure 4.4** shows these linearized second order kinetic plots of the experimental transient reflectance data obtained here for PC105.

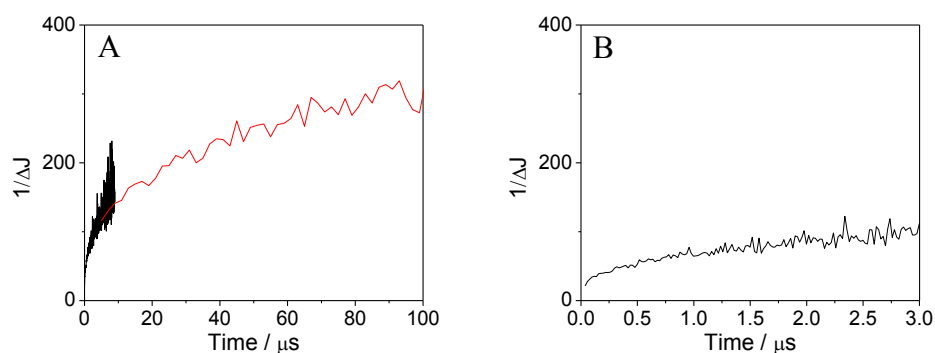


Figure 4.4: Reciprocal transient reflectance signal measured at 500 nm of PC105 after excitation with 1 mJ/cm² in the time domains 100 μ s (A) and 3 μ s (B) taken from the 10 μ s measurement (black) and the 1 ms measurement (red). Reprinted from Ref. 134.

Interestingly, no linear tendency of the inverse change in reflectance could be achieved for the entire time-scale. However, **Figure 4.4A** reveals that a nearly linear trend was observed in the long-time domain ranging from 20 to 100 μ s. Furthermore, **Figure 4.4B** shows that a linear trend is also seen if the selected time domain is as small as 3 μ s. Both images show that the slope of the signal is higher in short time intervals after excitation and becomes smaller over the course of time. The linearization of the second order function (cf. **Equation 2.9**) gives the second order decay constant k_2 , representing the slope of the signal. Therefore, the slope and, accordingly, the recombination constant of the charge carriers decrease over the course of time.

Despite this non-linear trend, the signal can be modeled by a combination of linear functions with varied slope. **Table 4.1** lists the second order rate constants obtained for

such a section-by-section analysis. The full set of the fitting parameters can be found in the appendix (**Table S3**). The table indicates that the second order decay constant is constantly decreasing over the course of time.

Table 4.1: Results of second order fit with baseline (**Equation 4.1**) of the transient reflectance measured at 500 nm of PC105 after excitation with 1 mJ/cm². Reprinted from Ref. 134.

Time window	40 ns – 4.3 μ s	4.3 μ s – 9 μ s	9 μ s – 430 μ s	430 μ s – 899 μ s
$k_2 / 10^6 \text{ a. u.}$	137.26	9.82	2.66	0.87

In fact, the experimental data shown in **Figure 4.4** agrees with previously published tendencies. Charge carrier signals obtained employing high laser intensities (up to 20 mJ/cm²) might be fitted to second order decay functions if the observed or chosen time window is appropriately selected.^{35,138} The discrepancy between the ideal bimolecular behavior and the experimental data, which is in particular visible for the boundaries of the selected time domain (cf. **Figure 4.3**), is compensated for by the addition of a baseline diverging for each time-scale.^{30,35,47} However, the successful kinetic analysis of transient signals over a broad time-scale is typically not feasible with a second order approach.³⁶

Effect of the laser intensity on the second order fit

The transient reflectance signals measured at 500 nm employing PC105 were detected after laser excitation with varied laser intensity (0.6-5 mJ/cm²). **Figure 4.5** displays the increase in the transient signal intensity as a function of the laser intensity.

The charge carrier signal increases by 19 % if the laser intensity is doubled from 1 mJ/cm² to 2 mJ/cm². In the range between 1-2 mJ/cm² a linear correlation of the charge carrier signal on the laser intensity can be expected. However, the ΔJ values obtained for the highest laser intensities (3-5 mJ/cm²) are smaller than this linear correlation indicates. For a large variation of the laser intensity, the plot of ΔJ against laser intensity might be better represented by a logarithmic function, since doubling the laser intensity from 2 to 4 mJ/cm² resulted in a 20 % increase in the signal as well.

An approximately linear correlation can only be assumed for low laser intensities producing small amounts of transient species,¹⁴² since the number of trapped states, localized at defects in the crystal structure, is limited. At certain laser intensities, a saturation effect is expected, leading to the formation of less additional trapped charge

carriers for excitation with higher laser intensities. At significantly higher laser intensities, all trapped states are occupied; thus, upon increase of the laser intensity the transient reflectance signal remains constant.

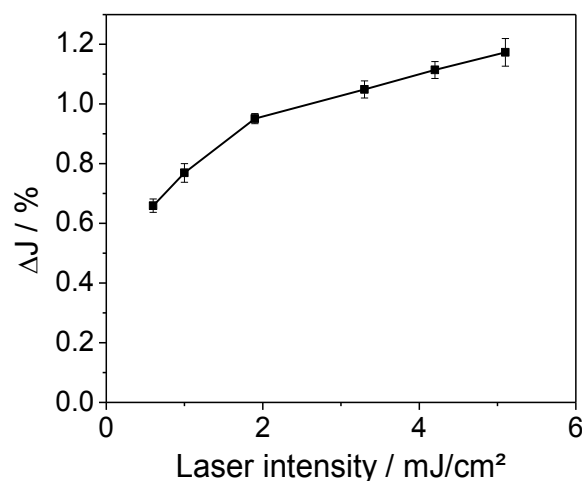


Figure 4.5: Transient reflectance signals of charge carriers photo-generated in PC105 measured at 500 nm 6 μ s after excitation for different laser intensities 0.6-5 mJ/shot. The experiments were performed in triplicates and the error bars indicate the standard deviation.

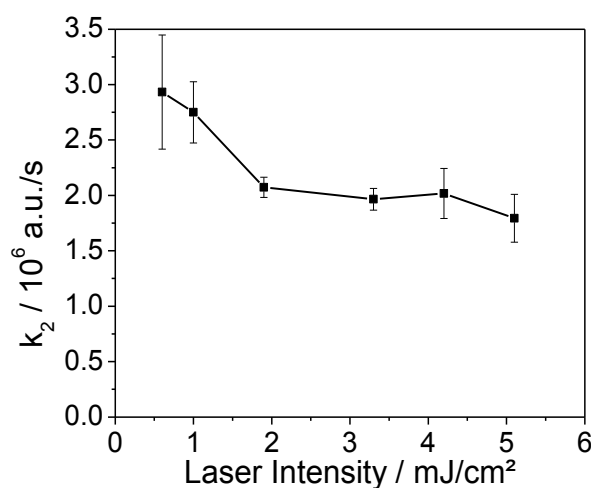


Figure 4.6: Second order decay constant k_2 calculated for the transient reflectance signals of charge carriers photo-generated in PC105 measured at 500 nm for different laser intensities (0.6-5 mJ/cm²). The experiments were performed in triplicates and the error bars indicate the standard deviation.

The charge carrier signals obtained from the experiments carried out employing 0.6-5 mJ/cm² laser intensity were fitted with second order fit functions with baseline (**Equation 4.1**). The full set of the fitting parameters can be found in the appendix (**Table**

S4). The impact of the variation of the laser intensity on the second order decay constant is shown in **Figure 4.6**. The second order decay constant shows quite constant values between 1.6 and $2.8 \cdot 10^6$ *a. u./s*. Nevertheless, smaller decay constants were observed for higher laser intensities.

4.1.3 Fractal kinetics fit

As an alternative to the second order approach, the present work utilizes a fitting model based on fractal geometry of the powder sample for the analysis of charge carrier recombination in TiO₂. According to the model of Kopelman¹¹⁶ the influence of the fractal-like structure (cf. **Equation 2.11**) was included in the second order rate law (**Equation 2.8**). The integration leads to **Equation 4.2**.

$$\Delta J = \frac{A(1-h)}{(1-h) + Ak_{2,f}t^{1-h}} \quad (4.2)$$

The decay constant k_2 was substituted by a time-dependent term derived from fractal-like kinetics ($k_{2,f}t^{-h}$). **Equation 4.2** has been employed for the kinetic analysis of the observed transient reflectance signals observed for TiO₂. All fitting parameters of the fractal fit applied to TiO₂ samples containing PC105 are given in the appendix (**Table S5** and **Table S6**). The charge carrier signal and the fit function observed for PC105 are shown in **Figure 4.7**.

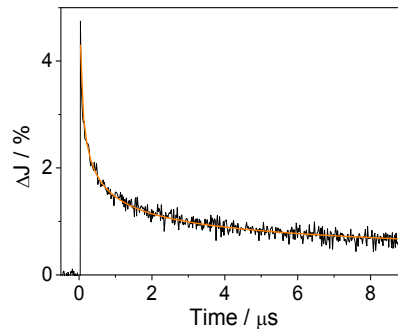


Figure 4.7: Transient reflectance signal of charge carriers photo-generated in N₂-saturated PC105 measured at 500 nm after laser excitation with fractal kinetics fit (orange).

In comparison to the second order fit function with baseline, a very good agreement between the experimental data points and the fit function were achieved without the need of an arbitrary baseline ($\bar{R}^2 = 0.98$) (cf. **Table S5**). Subsequently, the fractal kinetic model

proves to be feasible for the kinetic analysis of charge carrier recombination in TiO₂ samples and superior to a second order fit with an (arbitrary) baseline.

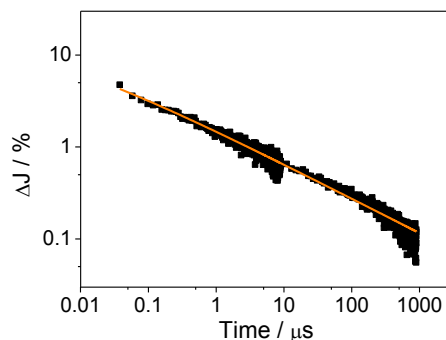


Figure 4.8: Transient reflectance signal of charge carriers photo-generated in PC105 (black) measured at 500 nm and bimolecular fit based on fractal-like kinetics (orange) in the time domain 40 ns to 1 ms. Reprinted from Ref. 134.

The charge carrier signals were observed in the time range from 40 nanoseconds to 1 microsecond. For visualization, a double logarithmic plot was employed to illustrate the charge carrier signal and the respective fractal fit function over the course of time (**Figure 4.8**). Double logarithmic plots with transient charge carrier signals observed in different time domains have already been used by Martin *et al.* for time-resolved microwave conductivity.¹⁰⁵ These plots enable the assessment of charge carrier signals over a broad range of time domains. **Figure 4.8** reveals that the obtained charge carrier signal observed for PC105 in both time-scales can be represented by a fractal kinetics fit.

Dependency of the fractal kinetics fit on the selected time window

As discussed in the last **Chapter 4.1.2**, possible drawbacks of the second order fit function are its arbitrary baseline and the dependency of the fitting results on the selected timeframe. To illustrate this dependency on the time domain, the transient reflectance at 500 nm of the mixed TiO₂ series containing PC105 and Kronos1001 was fitted either in the long time-scale between 5 μs and 1 ms (**Y**) (cf. **Table S2**) or in the full time-scale ranging from 40 ns to 1 ms (**X+Y**) (cf. **Table S1**). The resulting second order decay constants are shown in **Figure 4.9**.

The fit of full time-scale (**X+Y**) leads to 2-3 times higher recombination constants in comparison to the constants achieved for the long time-scale (**Y**). This change in the decay constant represents evidence for the inappropriateness of the fitting model. A better

correlation and higher coefficients of determination R^2 were only achieved for the short time-scales. The investigated transient reflectance signals of the TiO₂ series containing PC105 and Kronos1001 showed R^2 values of 0.93 to 0.98 for the time-scale **Y** and only R^2 values of 0.84 to 0.96 employing the full-scale **X+Y**.

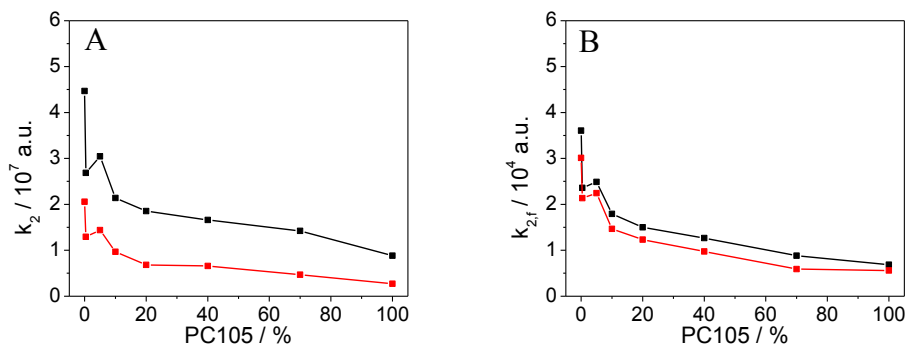


Figure 4.9: Second order decay constants k_2 of the transient reflectance signals of the TiO₂ series containing PC105 and Kronos1001 measured at 500 nm employing the time-scale 5 μ s to 1 ms (red) and the full time-scale of 40 ns to 1 ms (black) (A) and fractal decay constant $k_{2,f}$ of the transient reflectance signals of the TiO₂ series containing PC105 and Kronos1001 measured at 500 nm employing the time-scale 5 μ s to 1 ms (red) and the full time-scale of 40 ns to 1 ms (black) with $h = 0.5$ (B).

On the other hand, the deviation of the fractal decay constant $k_{2,f}$ is comparably small for the fit of both time domains (**Figure 4.9B**). In addition, the coefficient of determination for the fractal fit of both time-scales remains between 0.91 and 0.99.

Effect of laser intensity on the fractal dynamics fit

Equivalent to the analysis of the second order fit function, the fractal kinetics fit has been carried out for transient reflectance signals obtained employing different laser intensities. In the case of kinetic analysis with the fractal kinetics fit (**Equation 4.2**) two different situations can be modeled. On one hand, the value of the fractal parameter h can be kept constant. Since the average h value for the fractal fit function of the transient reflectance at 500 nm of PC105 is located around 0.5, h was set to 0.5. This enables the investigation of the effect of laser intensity on the fractal rate constant, since the fractal rate constant $k_{2,f}$ is the only remaining fitting parameter (cf. **Figure 4.10**). The fitting parameters are given in the appendix (**Table S7**).

Figure 4.10 shows that the fractal rate constant decreases slightly for higher laser intensities. The high laser intensity of 5 mJ/cm² results in a lower fractal rate constant indicating a decrease in the recombination speed at higher laser intensities.

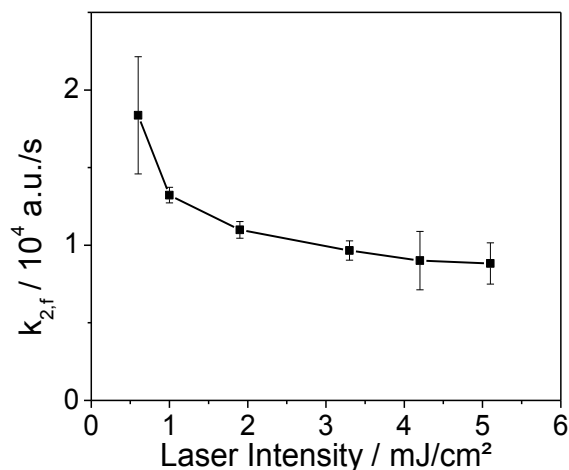


Figure 4.10: Fractal rate constant $k_{2,f}$ of the fractal kinetics fit applied to the transient reflectance signals of charge carriers photo-generated in PC105 measured at 500 nm for different laser intensities (0.6-5 mJ/cm²; $h = 0.5$). The experiments were performed in triplicates and the error bars indicate the standard deviation.

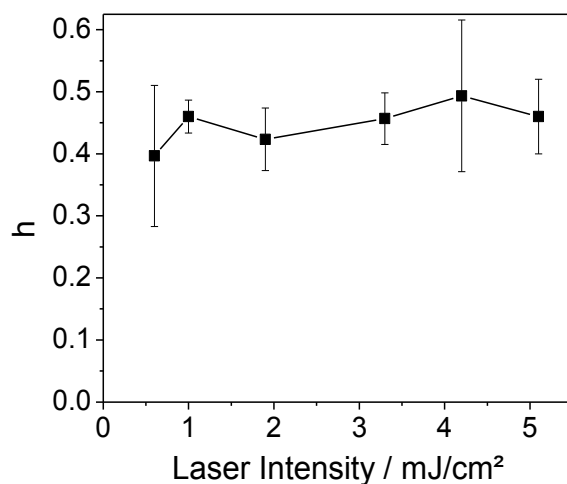


Figure 4.11: Fractal parameter h of the fractal kinetics fit applied to the transient reflectance signals of charge carriers photo-generated in PC105 measured at 500 nm for different laser intensities after normalization of the signals (0.6-5 mJ/cm²). The experiments were performed in triplicates and the error bars indicate the standard deviation.

Such a trend was also observed for the second order fit with baseline carried out at different laser intensities (cf. **Figure 4.6**). A new process in the charge carrier

recombination mechanism might be responsible for the change in the fractal rate constant. Undoubtedly, the rise of the laser intensity leads to a higher occupation of trap states with relatively vague impact on the charge carrier kinetics. Overall, relatively small changes in the laser intensity displayed only minor effects on the rate constants obtained by both fit functions.

On the other hand, in contrast to the kinetic analysis with locked h value, the fractal kinetic analysis employing different laser intensities can be carried out with a free calculation of the h value. This facilitates the study of the fractal parameter h at different laser intensities. The full set of the fitting parameters can be found in the appendix (**Table S8**).

Figure 4.11 illustrates the obtained h parameters for the kinetic analysis of the transient reflectance signals at 500 nm of PC105. The fractal parameter h of the fractal kinetics fit of the transient reflectance signals at 500 nm observed for PC105 stays constant for all laser intensities employed. Since the h parameter is related to the geometrical fractal structure of the sample, it can be assumed that h is an intrinsic property of the sample not changing with the laser intensity.

4.1.4 Photocatalytic NO degradation

The photocatalytic NO conversion Δc_{NO} and the photonic efficiencies ξ_{NO} determined employing the commercial TiO₂ materials are listed in **Table 4.2**. The commercial TiO₂ powders with small particle sizes (PC105 and PC500) showed high photonic efficiencies of 0.82 to 0.86 %. Kronos1001, on the other hand, which contains particles with a much larger primary particle size, displayed a smaller photonic efficiency of 0.45 %.

Table 4.2: Photocatalytic conversion of NO and photonic efficiencies calculated from the photocatalytic NO degradation of the commercial TiO₂ powder samples. Adapted from Ref. 48.

Material	$\Delta c_{NO} / \text{ppmv}$	$\xi_{NO} / \%$
	Untreated	Untreated
PC500	0.124	0.86
PC105	0.117	0.82
Kronos1001	0.065	0.45

In the literature, studies on the photocatalytic NO degradation over TiO₂ surfaces have already been published. Bloh *et al.*, for instance, reported a photonic efficiency of 0.31 %

for PC500 and a photonic efficiency 0.36 % for PC105, respectively.¹⁴³ Unfortunately, the ISO conditions were not applied in the reported study. Subsequently, the photonic efficiencies of up to 0.86 % of the same untreated samples observed in this study (cf. **Table 4.2**) can be explained by the difference in the NO concentration and the gas flow. Freitag *et al.*, indeed, observed a photonic efficiency of 0.5 % for UV100 (which is a commercial anatase TiO₂ with the same particle size as PC500) under similar conditions as those employed here.⁸² This value is very close to the photonic efficiencies around 0.8 % obtained here. Unfortunately, the sample area employed in their study was five times higher ($5 \cdot 10^{-3} \text{ m}^2$) in comparison to the geometrical sample area employed here.⁸² However, since in both cases photonic efficiencies have been employed (cf. **Equation 3.4**), the surface area should not show any influence on the results.

4.2 TiO₂ powders with binary particle size distribution

4.2.1 Structure of the TiO₂ agglomerates

Typically, TiO₂ powder samples contain agglomerates formed upon physical attraction of small primary nanoparticles. Splitting of these agglomerates is required to enable the formation of mixed agglomerates with mostly binary particle size distribution. The samples were prepared according to the ultrasound mixing procedure described in **Chapter 3.2 (Mixed TiO₂ powder samples)** and the microstructure was assessed by TEM imaging. As an example, two of the prepared samples are illustrated in **Figure 4.12**.

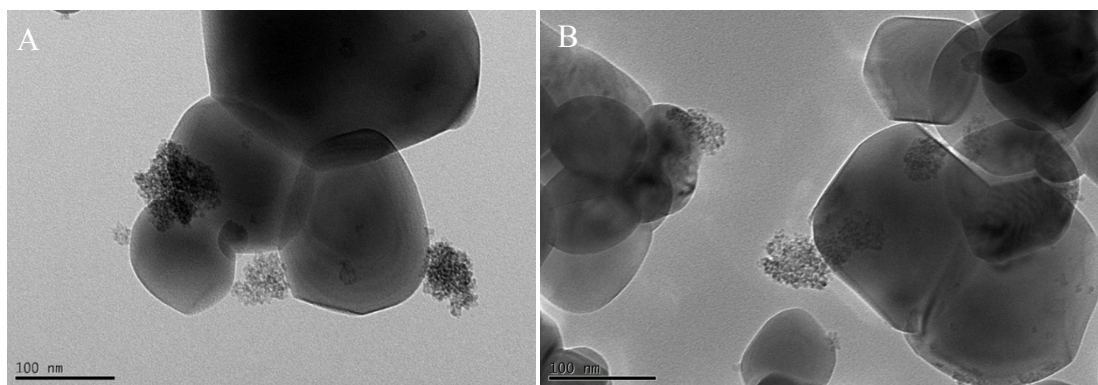


Figure 4.12.: TEM image of 5 % small PC500 particles (A) and 20 % small PC500 particles (B) on large Kronos1001, prepared via sonication (340 W/L) of aqueous ethanolic suspensions of TiO₂. Reprinted from Ref. 144.

The TEM images reveal that agglomerates of small PC500 and PC105, respectively, deposited on the larger Kronos1001 particles were achieved. This study aimed for intimate

contact between the differently sized particles, thus leading to an unrestricted charge transfer between the particles. Fortunately, the first step of the ultrasound treatment separated the small TiO₂ agglomerates and the addition of the larger particles in the second step lead to the formation of agglomerates having a binary particle size distribution. The TEM images displayed solely these mixed agglomerates.

4.2.2 Transient reflectance signals observed for the TiO₂ agglomerates

In this study two series of TiO₂ powders with varying particle size were synthesized and the transient reflectance signals at 500 nm were analyzed employing the second order fit with baseline and the fractal-like kinetics fit function (**Equation 4.2**).

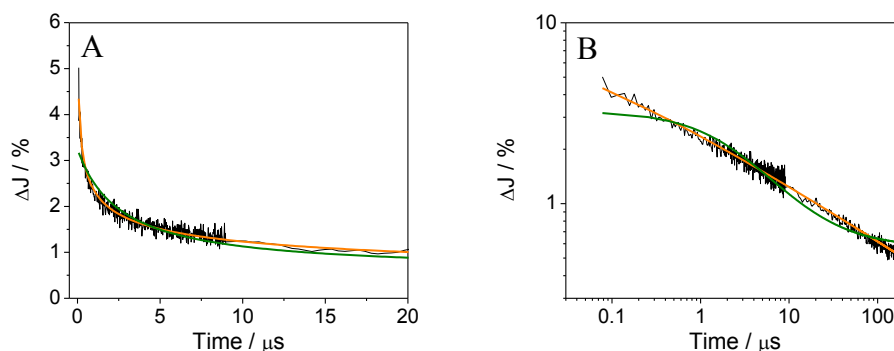


Figure 4.13: Transient reflectance signals of charge carriers photo-generated in (black) in 70 % PC105 mixed with Kronos1001 measured at 500 nm after laser excitation with second order fit (green) and fractal kinetics fit (orange) plotted from 0 μs to 20 μs (A) and double logarithmic plot over the full observed time-scale (B).

Figure 4.13 displays the transient reflectance signal at 500 nm of 70 % PC105 after laser excitation and both respective fit functions. The fitting parameters can be found in the appendix (**Table S1** and **Table S5**). The experimental trace of the transient reflectance has been combined from two separately recorded sets of data points in two time-scales (10 μs and 200 μs). The fit functions were conducted over the full time-scale. The fractal fit curve seems to show a better correlation with the experimental data points.

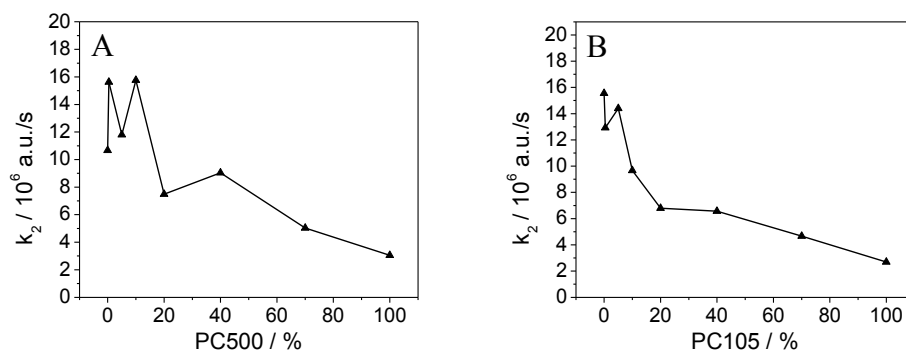


Figure 4.14: Second order decay constants k_2 calculated from the transient reflectance signals of charge carriers photo-generated in PC500 (A) and PC105 (B) mixed with Kronos1001 (N_2 -saturated samples, laser excitation with 2 mJ/pulse, $\lambda_{ex}=355 \text{ nm}$). Adapted from Ref. 48.

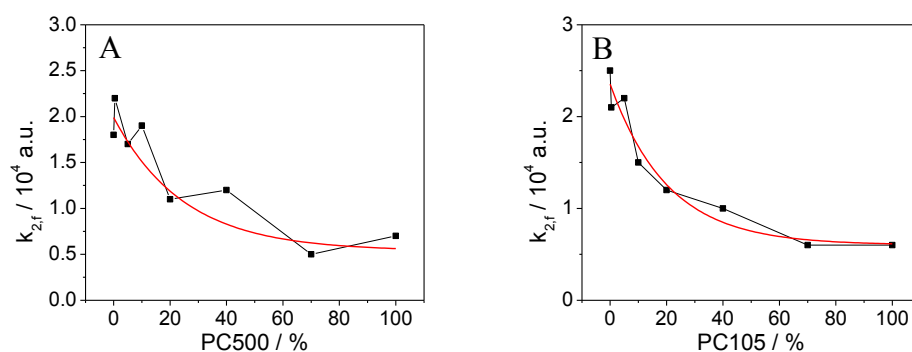


Figure 4.15: Fractal rate constants $k_{2,f}$ calculated from the transient reflectance signals of charge carriers photo-generated in PC500 (A) and PC105 (B) mixed with Kronos1001 at 500 nm (N_2 -saturated samples, laser excitation with 2 mJ/pulse, $\lambda_{ex}=355 \text{ nm}$, fractal parameter $h=0.5$, time domain 6-200 μs , with exponential fit function (red line). Adapted from Ref. 48.

For a better comparison of the two fit functions and the analysis of the effect of the binary particle size distribution, the second order rate constants and the fractal rate constants are shown in **Figure 4.14** and **Figure 4.15**, respectively. The fitting parameters of the two respective fit functions applied to the transient reflectance signals of PC500 are given in the appendix (**Table S9** and **Table S2**).

The second order decay constants obtained from the second order kinetics fit decreased for the samples containing more small particles of PC105/PC500. Particularly for the samples with low content of PC500, a large scattering of the second order decay constant was observed. This might be related to the disagreement of the experimental data points and the fit function (cf. **Figure 4.13**).

Like the second order decay constants, the fractal rate constants are lower for samples containing more small particles (cf. **Figure 4.15**). The complete list of fitting parameters can be found in the appendix (**Table S6** and **Table S10**). However, in comparison to the second order decay constants the fractal rate constants show less scattering and can be represented by an exponential function. The second order rate constants, on the other hand, display a more linear trend for samples containing higher amounts of small particles.

4.2.3 Photocatalytic NO degradation by the TiO₂ agglomerates

According to **Equation 3.4** the photonic efficiencies for the obtained NO degradation employing the mixed TiO₂ agglomerates were calculated (experimental details are described in **Chapter 3.4.2**). The photonic efficiencies ξ_{NO} of the TiO₂ reference materials with and without ultrasound treatment are compared in **Table 4.3**.

Table 4.3: Photocatalytic conversion of NO and photonic efficiencies calculated from the photocatalytic NO degradation of the ultrasound treated TiO₂ samples compared with the photonic efficiencies of the untreated basic TiO₂ materials. Adapted from Ref. 48.

Material	$\Delta c_{NO} / \text{ppmv}$	$\xi_{NO} / \%$	$\xi_{NO} / \%$
	Ultrasound treated	Ultrasound treated	Untreated
PC500	0.156	1.08	0.86
PC105	0.167	1.16	0.82
Kronos1001	0.091	0.63	0.45

Comparison of the photonic efficiencies for the untreated and ultrasound treated reference materials shows that the ultrasound procedure increased the photocatalytic activity of the samples. The washing and drying processes remove undesired compounds originating from residues of the technical synthesis of commercial TiO₂ powders. The TiO₂ powders contain chlorides, sulfates or phosphates due to the production *via* chloride or sulfate process, respectively. Since the TiO₂ powders employed here were made in the sulfate process, sulfate and phosphate were expected to be found on the surface of TiO₂. It has been reported that these ions strongly coordinate to the catalyst surface blocking active sites and, subsequently, reduce the photocatalytic activity.^{97,145} Hence, the increased photocatalytic activity after the ultrasound procedure can be explained by the removal of these ions from the TiO₂ surface.

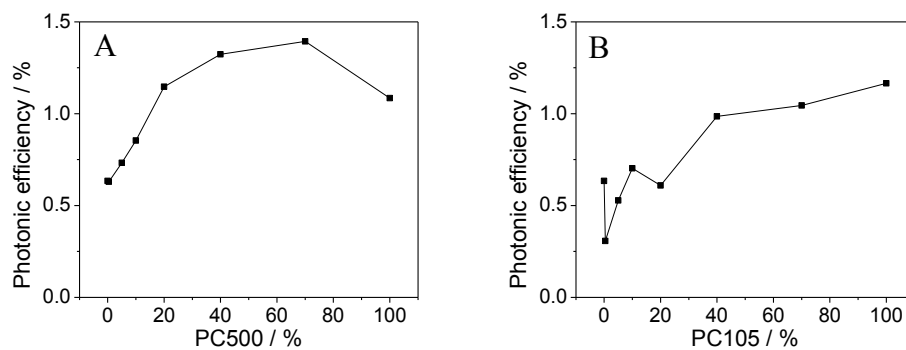


Figure 4.16: Photonic efficiencies obtained from the photocatalytic NO degradation employing PC500 (A) and PC105 (B) mixed with Kronos1001. Adapted from Ref. 48.

This thesis investigates two series of mixed TiO_2 samples with varying particle size distribution. Similar to the results shown above, the photonic efficiencies were calculated (**Figure 4.16**). The photonic efficiencies taken from the photocatalytic NO degradation of the TiO_2 samples with binary particle size distribution increased with higher loadings of both employed small particles (PC500/PC105). A maximum in activity was observed for mixtures containing 70 % PC500. This sample and the samples with 20 and 40 % PC500 had higher photonic efficiencies than the pure PC500 or pure Kronos1001 materials. The photonic efficiencies obtained for the TiO_2 series containing PC105 (**Figure 4.16B**) show analog trends to the samples containing PC500. Both series display an increasing trend in photocatalytic activity with higher content of small particles. Nonetheless, no mixed sample containing PC105 outperformed the pure PC105, which showed the highest photonic efficiency of this series. Overall, the results of this study confirm that PC105 and PC500 both possess a high photocatalytic activity for the removal of NO.

4.2.4 Surface area of the TiO_2 agglomerates

The BET surface areas of the two series of mixed TiO_2 were determined (**Figure 4.17**). The BET surface area increases linearly with the content of smaller particles (PC500/PC105). Pure Kronos1001 shows a BET surface area of $10 \text{ m}^2/\text{g}$, while the samples with PC105 and PC500 display a BET surface area of $78 \text{ m}^2/\text{g}$ and $305 \text{ m}^2/\text{g}$, respectively. However, the BET surface area might not always be a perfect tool for the quantification of the active surface area, since the detection is based on the complete removal of adsorbates, such as surface-adsorbed water. Therefore, the adsorbed amount of NO on the TiO_2 powder surfaces was determined experimentally (cf. **Chapter 3.4.2**).

The results are shown in **Figure 4.18**. In contrast to the large effect of the particle size observed for the BET surface area (cf. **Figure 4.17**), the amount of adsorbed NO only increases by a factor of 1.5-2 for the two series with binary particle sizes distribution.

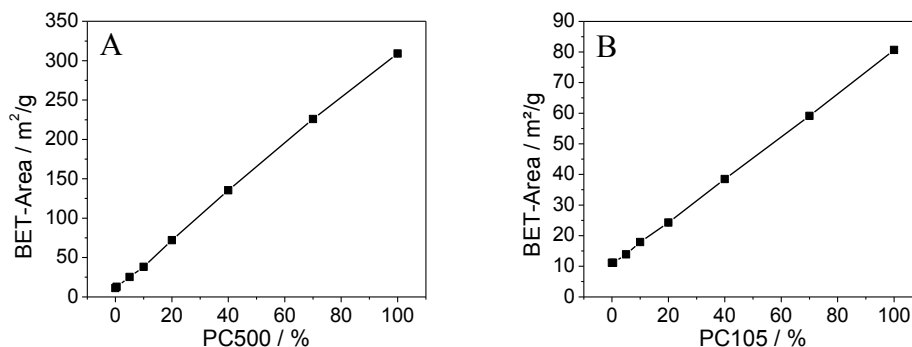


Figure 4.17: BET surface area of PC500 (A) and PC105 (B) mixed with Kronos1001 (average from three measurements). Reprinted from Ref. 48.

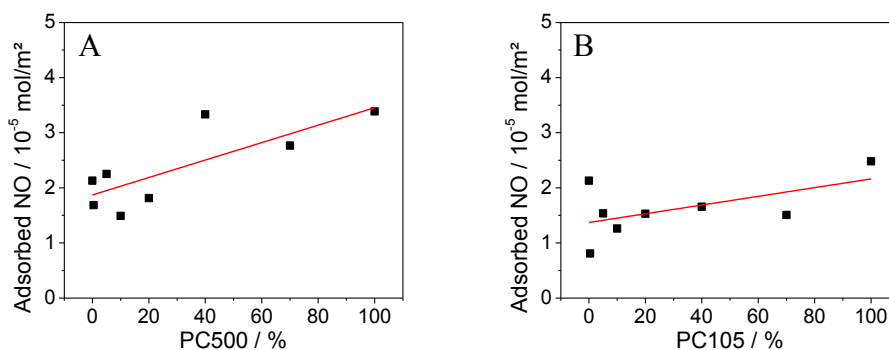


Figure 4.18: Adsorbed amount of NO normalized to the geometrical surface area on PC500 (A) and PC105 (B) mixed with Kronos1001 (the linear fits in red are a guide to the eye). Reprinted from Ref. 48.

Identical to the trends observed for the BET surface area, a higher PC500 content lead to higher NO adsorption compared to samples containing identical amounts of PC105. This is caused by the larger difference in the particle size between Kronos1001 and PC500 (125 nm and 7 nm) in contrast to the particle size difference of Kronos1001 and PC105 (125 nm and 17 nm).

4.3 TiO₂ powders mixed with additives

The effects of single additives, such as BaSO₄, Na₂CO₃ and CaCO₃, mixed with TiO₂ (KronoClean 7050) on the photocatalytic NO degradation and on the charge carrier

kinetics were investigated by means of UV-Vis absorption measurements and transient reflectance spectroscopy.

4.3.1 TiO₂-BaSO₄

Transient signals of charge carriers photo-generated in TiO₂-additive powder samples

The TiO₂-additive samples, which were prepared by simple grinding of TiO₂ powder with the respective additive (cf. **Chapter 3.2**), were analyzed by transient reflectance spectroscopy.

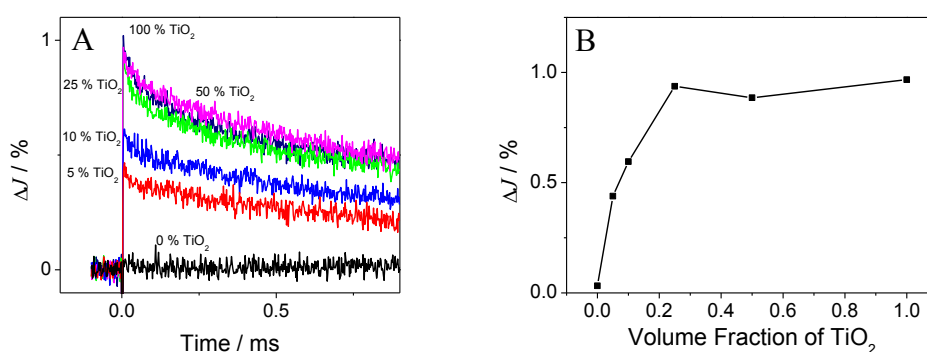


Figure 4.19: Transient reflectance signals of charge carriers photo-generated in TiO₂-BaSO₄ powder mixtures measured at 500 nm (N₂-saturated samples, laser excitation with 2 mJ/pulse, λ_{ex} =355 nm) (A) and height of the transient reflectance signals of charge carriers photo-generated in TiO₂-BaSO₄ measured at 500 nm 5-10 μ s after the excitation (B). Adapted from Ref. 135.

Figure 4.19A displays the transient reflectance signals of the TiO₂-BaSO₄ powder samples after laser excitation. Clearly, the height of the transient reflectance signal of the photo-generated charge carriers in TiO₂ decreases in the presence of high amounts of BaSO₄ (0-10 % remaining TiO₂). The signals can easily be compared by employing the signal heights, which were achieved by averaging the signal over a short period of time (5-10 μ s), to remove noise. The result of this procedure was named the height of the transient reflectance and is shown in **Figure 4.19B**.

The transient reflectance signals were analyzed with the fractal kinetics fit (cf. **Equation 4.2**). The fitting parameters are given in the appendix (**Table S11**). Prior to this analysis, the signals were normalized, since the TiO₂ content changes over a broad range of volume fractions (from 0 % to 100 % TiO₂). **Figure 4.20** illustrates such a fractal fit function applied to the transient change in reflectance at 500 nm of KronoClean7050.

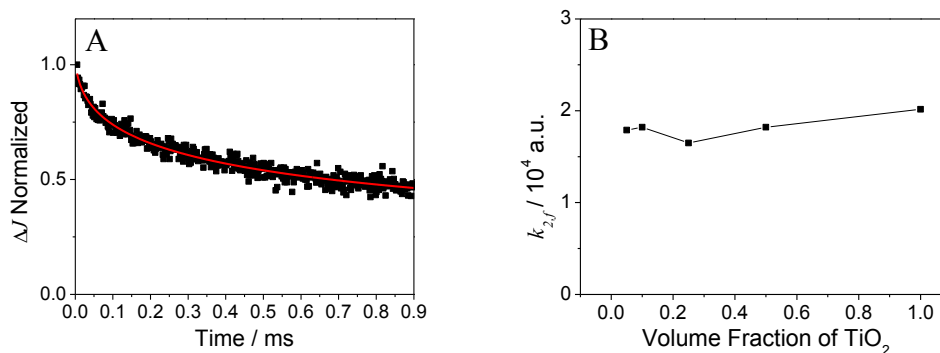


Figure 4.20: Transient reflectance signals of charge carriers photo-generated in TiO₂ (KronoClean 7050) measured at 500 nm and fractal fit (red) from the transient reflectance measurements after laser excitation (A) and fractal rate constant $k_{2,f}$ taken from the normalized transient reflectance signals of charge carriers photo-generated in TiO₂-BaSO₄ measured at 500 nm after laser excitation (N₂-saturated samples, $h = 0.5$, laser excitation with 2 mJ/pulse, $\lambda_{ex}=355$ nm) (B). Reprinted from Ref. 135.

The normalized transient reflectance signals observed for the TiO₂-additive samples could successfully be fitted with the fractal charge carrier kinetics fit. Analogue to the results observed for the pure TiO₂ samples and the TiO₂ samples with binary particle size distribution, the fractal fit shows an excellent agreement with the experimental data points.

Photonic efficiency of the NO degradation by the TiO₂-additive powder samples

More effects of BaSO₄ on TiO₂ in the TiO₂-additive mixtures could be detected by the photocatalytic NO degradation experiments (cf. **Chapter 3.4.2**). The resulting photonic efficiency is shown in **Figure 4.21A**. Furthermore, the UV-light absorptions of the samples at 365 nm were detected (cf. **Figure 4.21A**). These absorption values were used for the calculation of the apparent quantum yields (cf. **Figure 4.21B**), according to **Equation 3.5**.

Despite the low content of photocatalyst, the samples with 5-50 % TiO₂ displayed quite high photocatalytic NO conversion. The samples consisting of 20 % TiO₂ mixed with BaSO₄ exhibited 70 % of the photonic efficiency observed for the pure photocatalyst (0.6 % and 0.84 %, respectively). The high photocatalytic activities could be related to the high UV-light absorption of the samples.

The photonic efficiencies are based on the incident light intensity and, hence, are not suitable for the assessment of the absolute photocatalytic activity. In contrast to the photonic efficiency, the quantum yield considers how much light is absorbed and employed for the observed photocatalytic effect. The apparent quantum yield was

4. Results

calculated to enable the analysis of the photocatalytic performance normalized to the amount of the absorbed UV-light (cf. **Figure 4.21B**).

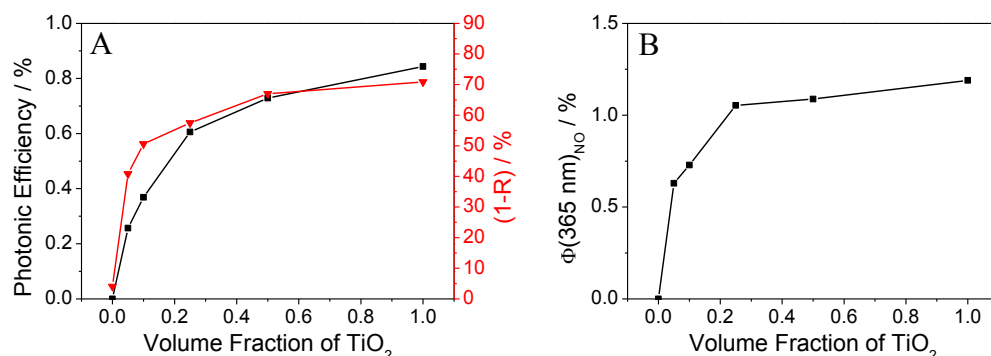


Figure 4.21: Photonic efficiencies obtained from the photocatalytic NO degradation and light absorption values of TiO₂-BaSO₄ powder mixtures calculated from the non-reflected light (1-R) at 365 nm (A) and apparent quantum yields $\Phi(365 \text{ nm})$ obtained from the photocatalytic NO degradation employing TiO₂-BaSO₄ powder mixtures as a function of the TiO₂ volume fraction. Reprinted from Ref. 135.

The quantum yield of the samples containing 25 % to 100 % TiO₂ is nearly constant. Hence, a comparable amount of absorbed UV-light causes a constant photocatalytic effect for these samples. The samples with 5 % and 10 % TiO₂ revealed a smaller quantum yield, corresponding to a smaller amount of photocatalytic activity for the same amount of absorbed UV-light.

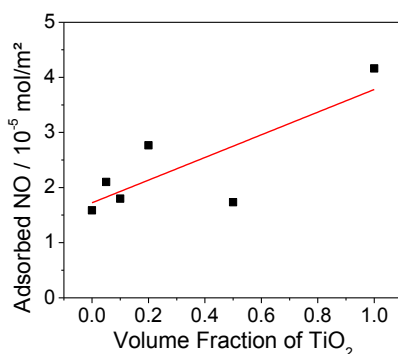


Figure 4.22: Adsorbed amount of NO normalized to the geometrical surface area on the TiO₂-BaSO₄ powder samples (the linear fit in red is a guide to the eye).

Figure 4.22 shows that the adsorbed amount of NO on the TiO₂-BaSO₄ powder samples is a linear function of the TiO₂ content. Indeed, similar to the results illustrated in **Figure 4.18**, large amounts of small TiO₂ particles in the mixed samples facilitate higher NO adsorption onto the sample surface.

4.3.2 TiO₂-Na₂CO₃ and TiO₂-CaCO₃

Transient signals of charge carriers photo-generated in TiO₂-additive powder samples

For the evaluation of the charge carrier kinetics in these samples, transient reflectance measurements were carried out. The heights of the transient reflectance signals of the mixed TiO₂-additive samples are shown in **Figure 4.23**.

Figure 4.23A shows the results for the TiO₂-Na₂CO₃ samples. The transient signal height of these samples decreases with a decreasing amount of TiO₂. On the other hand, the TiO₂-CaCO₃ samples revealed much higher transient reflectance signals (**Figure 4.23B**). The highest transient reflectance signal was observed for the sample consisting of 25 % of CaCO₃ mixed with TiO₂. In comparison to the results observed for TiO₂-Na₂CO₃, all respective TiO₂-CaCO₃ samples with the same amount of photocatalyst show higher transient reflectance signals.

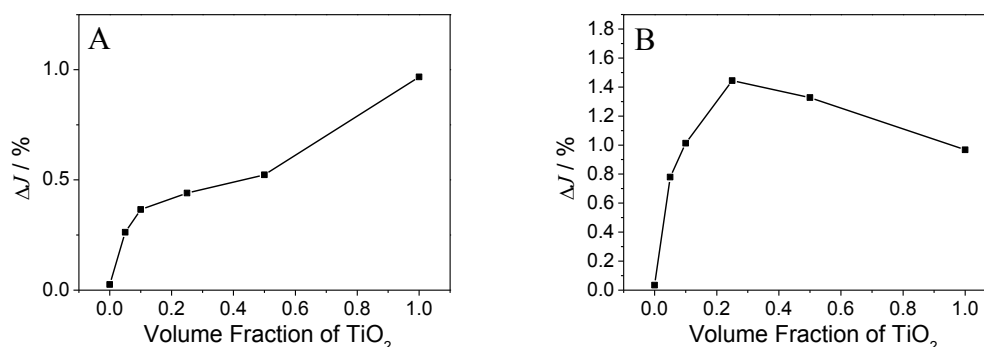


Figure 4.23: Height of the transient reflectance signals of charge carriers photo-generated in TiO₂-Na₂CO₃ (A) and TiO₂-CaCO₃ (B) powder mixtures measured at 500 nm 5-10 μs after the laser excitation (N₂-saturated samples, laser excitation with 2 mJ/pulse, λ_{ex}=355 nm). Adapted from Ref. 135.

The fractal rate constants detected for the TiO₂-Na₂CO₃ samples are shown in **Figure 4.24A**. The fitting parameters for both carbonate samples are listed in the appendix (**Table S12** and **Table S13**). A higher fraction of TiO₂ in the TiO₂-Na₂CO₃ samples resulted in smaller fractal rate constants in comparison to the samples containing more Na₂CO₃. The samples containing CaCO₃ displayed a different trend (cf. **Figure 4.24B**).

All TiO₂-CaCO₃ samples displayed a rather stable fractal rate constant between 1.5 and 2.0 · 10⁴ a.u. The smallest rate constant was detected for the sample containing 25 % of CaCO₃ mixed with TiO₂.

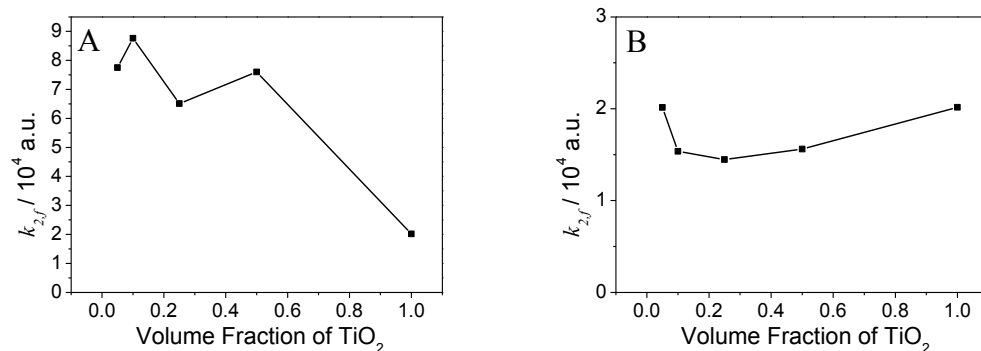


Figure 4.24: Fractal rate constant $k_{2,f}$ taken from the transient reflectance signals of charge carriers photo-generated in $\text{TiO}_2\text{-Na}_2\text{CO}_3$ (A) and $\text{TiO}_2\text{-CaCO}_3$ (B) measured at 500 nm after laser excitation as a function of the volume fraction of TiO_2 (N_2 -saturated samples, $h = 0.5$, laser excitation with 2 mJ/pulse, $\lambda_{ex}=355$ nm). No meaningful kinetic analysis could be carried out for the transient reflectance signals of the two samples not containing any TiO_2 . Adapted from Ref. 135.

Photonic efficiency of the NO degradation by the TiO_2 -additive powder samples

Similar to the $\text{TiO}_2\text{-BaSO}_4$ samples, the UV-light absorption and the apparent quantum yield taken from the NO degradation were detected for the additives Na_2CO_3 and CaCO_3 . The results are shown in **Figure 4.25A** and **Figure 4.25B**, respectively.

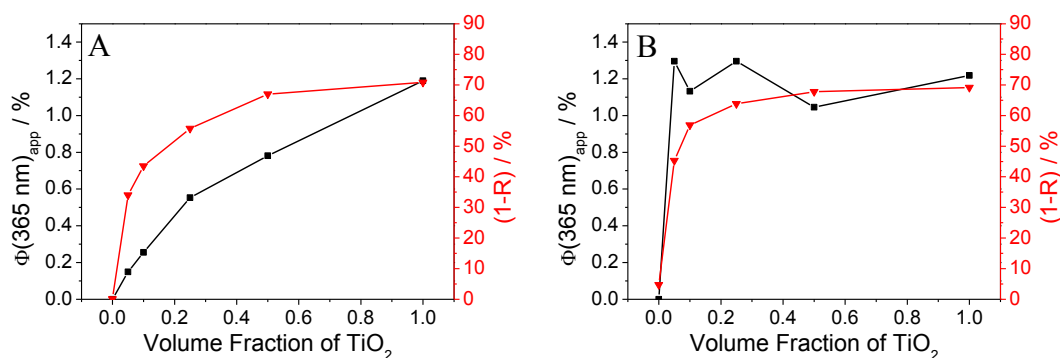


Figure 4.25: Apparent quantum yields $\Phi(365 \text{ nm})$ obtained from the photocatalytic NO degradation and absorption values, measured as the non-reflected light (1-R) at 365 nm for the $\text{TiO}_2\text{-Na}_2\text{CO}_3$ (A) and $\text{TiO}_2\text{-CaCO}_3$ (B) powder mixtures. Reprinted from Ref. 135.

All of the tested additives lead to a quite strong UV-light absorption for the TiO_2 -additive mixtures. A TiO_2 volume fraction of 0.1 proved to be sufficient for high UV-light absorptions at 365 nm of 43 % and 57 % for $\text{TiO}_2\text{-Na}_2\text{CO}_3$ and $\text{TiO}_2\text{-CaCO}_3$, respectively. These values are close to the UV-light absorption of the pure photocatalyst (70 %). However, the two carbonates revealed diverging trends for the apparent quantum yields.

While the $\text{TiO}_2\text{-Na}_2\text{CO}_3$ samples displayed a nearly linear decrease of the quantum yield for increased carbonate content, the TiO_2 samples mixed with CaCO_3 showed a small increase in the quantum yield to 1.3 % for the samples containing 5 % and 25 % CaCO_3 (**Figure 4.25B**).

Figure 4.26 shows the adsorbed amount of NO on the surface of the TiO_2 samples mixed with one of the carbonates. It is apparent, that all of the samples mixed with sodium carbonate displayed low amounts of adsorbed NO (cf. **Figure 4.26A**), while the $\text{TiO}_2\text{-CaCO}_3$ samples revealed a linear dependency between the amounts of adsorbed NO and the volume fraction of TiO_2 (cf. **Figure 4.26B**). This linear dependency was observed for the $\text{TiO}_2\text{-BaSO}_4$ samples as well (cf. **Figure 4.22**).

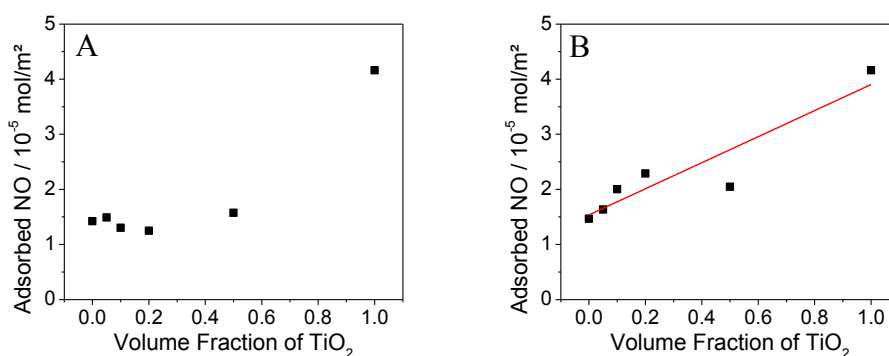


Figure 4.26: Adsorbed amount of NO normalized to the geometrical surface area on the $\text{TiO}_2\text{-Na}_2\text{CO}_3$ (A) and $\text{TiO}_2\text{-CaCO}_3$ (B) powder mixtures (the linear fit in red is a guide to the eye).

4.4 TiO_2 paints

In addition to the investigation of pure TiO_2 photocatalyst powders and mixed TiO_2 -additive powder samples, a series of TiO_2 paints was studied. The silicate paints were provided by the same paint company and share a nearly identical composition. Each paint sample contains the same weight fraction of photocatalyst and some inorganic binder. Overall, the paints do not contain many organic additives in the paint matrix, since these materials could act as undesired targets for the photocatalytic process. Identical to the other materials, the correlation of charge carrier kinetics and photocatalytic NO degradation was analyzed.

One of the main difficulties of the analysis of the TiO_2 paints is their complex structure. Every additive has many potential interdependencies with the basic reactions of the

photocatalytic process, such as light absorption, probe molecule adsorption, charge carrier generation, charge carrier transfer, and product desorption. In particular, the TiO₂ paints containing another semiconductor material or dyes display additional transient signals, which hamper the kinetic analysis of the charge carrier signal observed for TiO₂.

The transient spectra of the TiO₂ paints in the time-scale ranging from 58 ns to 2 μs are shown in **Figure 4.27**. Interestingly, the paints containing iron and cobalt displayed large transient signals at 500 nm (**Figure 4.27B and E**). However, these bands could be related to transient signals of the employed additives and were identified in pure iron oxide and cobalt oxide samples as well. Hence, these signals do not represent the charge carrier signals observed for TiO₂ and the kinetic analysis of the charge carrier recombination in these TiO₂ paint samples is challenging.

One possible approach for the kinetic analysis of the transient signals observed for TiO₂ in the paint matrix would be the subtraction of the overlapping signal caused by the respective additive (iron oxide or cobalt oxide). However, this simple approach might be solely applicable for binary mixtures with known composition and absorption/scattering coefficients of the two components, while the separation of the complex signals observed for TiO₂ paints is not possible.

The problem of the overlapping transient signals could also be solved by the analysis of the signal in a longer time-scale, ranging from 5 μs to 200 μs. The respective spectra are shown in **Figure 4.28**.

In contrast to the spectra obtained at time-scales closer to the laser excitation, the transient signals after 5 μs are less influenced by the large transient signals of the additives. If the decay kinetics of the transient signals observed for iron oxide and cobalt oxide are significantly faster in comparison to the decay kinetics of the trapped charge carriers in TiO₂, the decay kinetics of the transient signals a long period after the excitation are solely influenced by the recombination kinetics of trapped charge carriers.

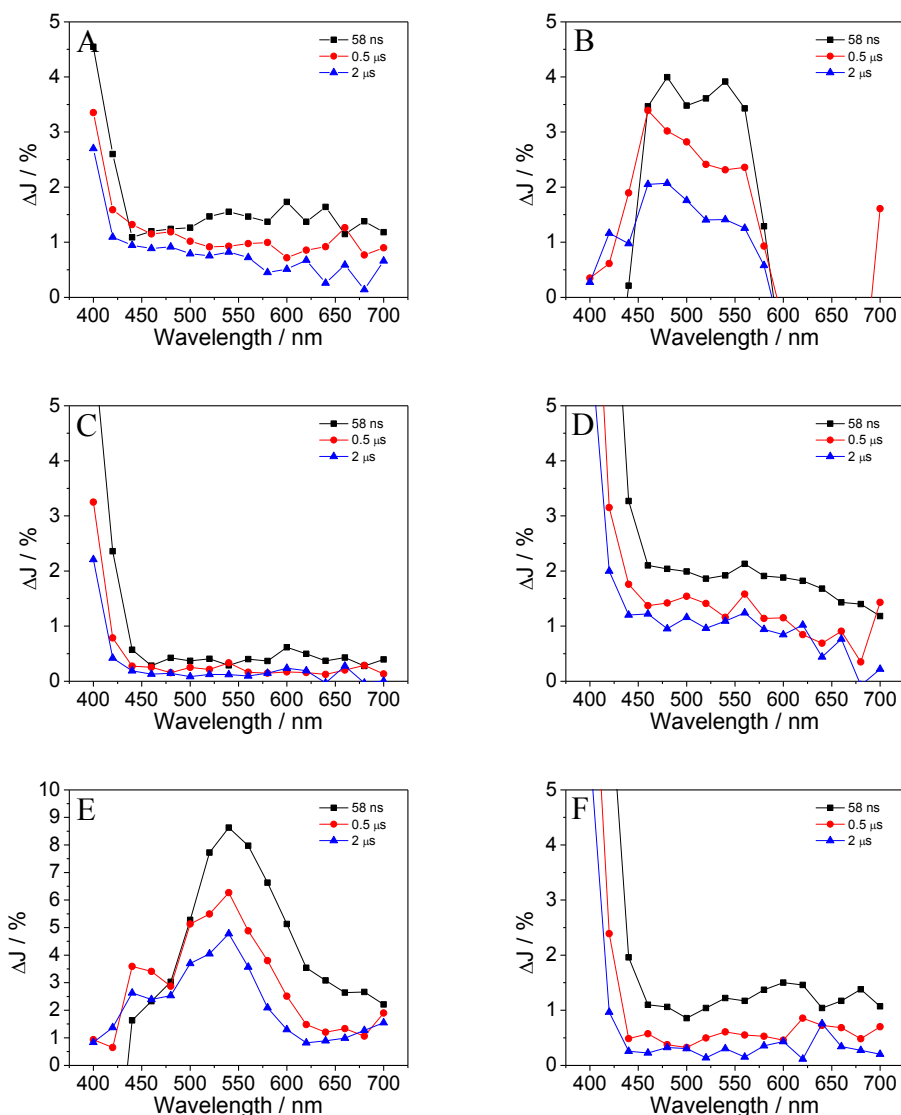


Figure 4.27: Transient reflectance spectra of charge carriers photo-generated in TiO₂ paints at 58 ns (black), 0.5 μs (red), and 2 μs (blue) after the laser excitation (N₂-saturated samples, laser excitation with 2 mJ/pulse, λ_{ex} =355 nm). The paints contained the following ions or additives: lithium (A), iron (B), copper (C), zinc (D), cobalt (E), and reference sample without additives (F).

Therefore, the kinetic analysis of the charge carrier recombination in TiO₂ paints with the fractal kinetics fit was carried out in the time-scale ranging from 5 to 200 μs. The complete list of the fitting parameters of the fractal kinetics fit is shown in the appendix (**Table S14**). The fractal rate constant of the transient reflectance signal of the photo-generated charge carriers is given in **Table 4.4**. Additionally, the photocatalytic NO degradation experiments were carried out and the resulting photonic efficiencies are shown in **Table 4.4** as well.

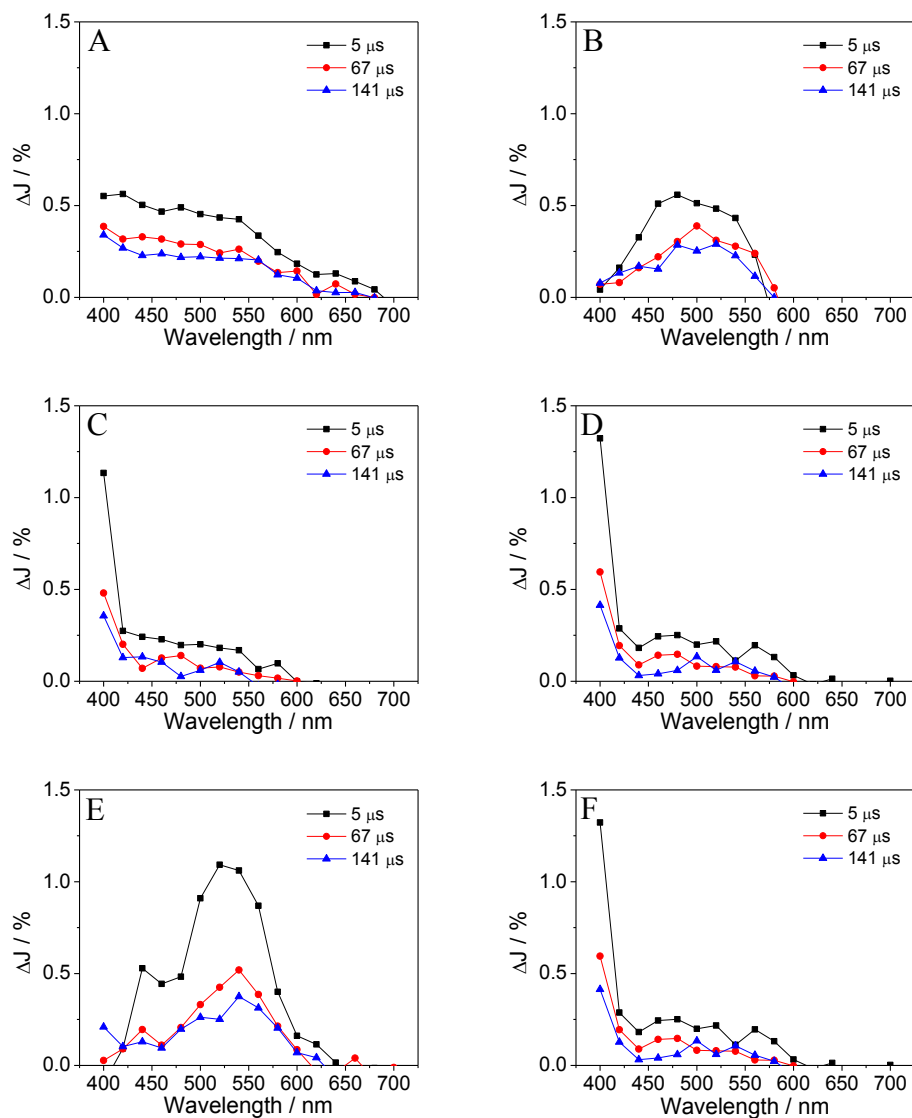


Figure 4.28: Transient reflectance spectra of carriers photo-generated in TiO₂ paints at 5 μs (black), 67 μs (red), and 141 μs (blue) after the laser excitation (N₂-saturated samples, laser excitation with 2 mJ/pulse, λ_{ex} =355 nm). The paints contained the following ions or additives lithium (A), iron (B), copper (C), zinc (D), cobalt (E), and reference sample without additives (F).

Table 4.4: Fractal rate constant calculated for the transient reflectance signals of charge carriers photo-generated in TiO₂ paints measured at 500 nm after laser excitation (N₂-saturated samples, laser excitation with 2 mJ/pulse, λ_{ex} =355 nm) and photonic efficiencies calculated from the photocatalytic NO degradation of the TiO₂ paints.

Additive	Lithium	Iron	Copper	Zinc	Cobalt	Reference
$k_{2,f}/10^4$ a. u.	1.0	0.7	2.9	0.8	1.5	5.9
ξ_{NO} / %	0.12	0.09	0.02	0.05	0.06	0.04

The adsorption of NO on the surface of the TiO₂ paint samples is shown in **Figure 4.29**. Overall, the adsorption of NO on the paint surfaces was much smaller than the adsorption of NO on the TiO₂ powder samples. Moreover, except the paint containing lithium, most paint samples displayed quite similar NO adsorption.

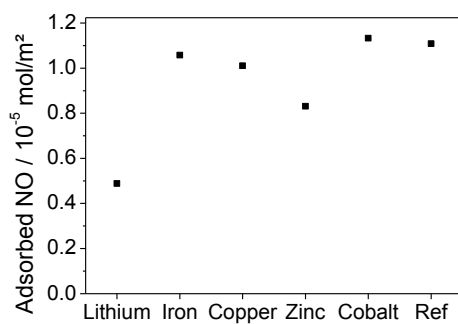


Figure 4.29: Adsorbed amount of NO normalized to the geometrical surface area on the TiO₂ paint samples.

5. Discussion

This chapter first focuses on the transient reflectance signals typically observed after the laser excitation of the TiO₂ powder samples. The effects of the experimental characteristics, such as laser intensity and excitation wavelength, on the signals are analyzed. Furthermore, the different kinetic models for the mathematical analysis of charge carrier recombination in TiO₂ were employed to fit the experimental data and are discussed and compared in the following chapter. More specifically, the relevance and the feasibility of the fractal kinetics fit are examined in detail. Subsequently, the fractal kinetics fit function is utilized for the analysis of the charge carrier recombination in TiO₂ samples with binary particle size distribution and TiO₂ samples ground with various additives. Finally, the correlation between the charge carrier recombination dynamics obtained for the TiO₂ samples and the apparent quantum yields taken from the photocatalytic NO degradation are discussed.

5.1 Transient reflectance signals in TiO₂

5.1.1 Identification of trapped charge carriers

The photo-generated charge carriers in TiO₂ were detected by transient absorption spectroscopy, carried out in diffuse reflectance. In transient absorption spectroscopy, the height of the transient reflectance signal is a linear function of the charge carrier concentration, provided that certain conditions are maintained.^{139,142,146} One requirement is that the change in reflectance needs to be smaller than 10%.¹³⁹ This enables the direct correlation of the transient signals with respective trapped charge carrier concentrations. Unfortunately, the absolute concentration is only available if the molar absorption coefficient of the transient species has been identified.

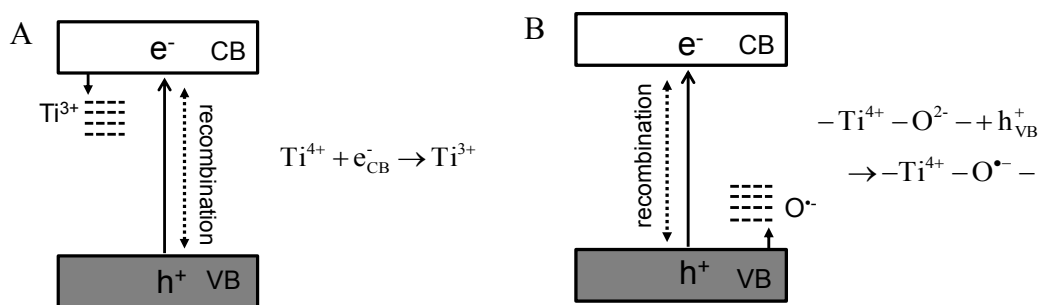


Figure 5.1: Trapping of photo-generated electrons (A) and holes (B) in TiO₂.

Figure 5.1 illustrates the trapping processes of photo-generated charge carriers in TiO_2 which result in the formation of such species (Ti^{3+} and O^\bullet radicals). The photo-generated electrons are trapped as Ti^{3+} centers and the photo-generated holes are trapped as oxygen-centered radicals originating from bridging or surface oxygen atoms.^{32,33,110,147}

Unfortunately, the direct calculation of the molar absorption coefficients of trapped holes and electrons is impossible due to the unknown concentration of trapped charge carriers.⁶⁹ However, some studies have estimated values between 600 and $800 \frac{\text{L}}{\text{mol}\cdot\text{cm}}$ for trapped electrons at 850 and 700 nm, respectively.^{114,148} An absorption coefficient of $9.2 \cdot 10^3 \frac{\text{L}}{\text{mol}\cdot\text{cm}}$ at 475 nm has been reported for trapped holes.^{28,141} **Figure 5.2** shows the wavelength regions of the transient absorption of the trapped charge carriers¹⁰⁹ in the transient reflectance spectra obtained in this study.

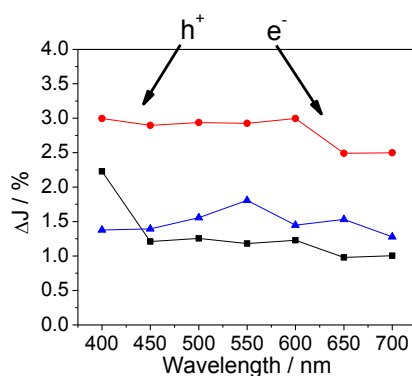


Figure 5.2: Transient reflectance spectra of photo-generated charge carriers in the three TiO_2 samples (Kronos1001 (black), PC105 (red), PC500 (blue)) after laser excitation with 2 mJ/pulse, $\lambda_{ex}=355$ nm. This image has been adapted from **Figure 4.2**.

The charge carrier recombination obtained for the TiO_2 samples is assessed by the mathematical analysis of the decay of the transient reflectance signals. This correlation requires that under the employed inert N_2 gas conditions solely charge carrier recombination kinetics is observed and no charge transfer to adsorbed chemicals or scavenger molecules occurs. In the presence of alcohols as electron donors, for instance, the charge carrier signals will show diverging decay kinetics.

5.1.2 Choice of experimental parameters

Unfortunately, previous studies seldom discuss the effect of laser intensity and excitation wavelength. Hence, it is not always well-known why specific experimental characteristics

were selected. This chapter aims to shed more light on these factors by discussing, in particular, the influence of the laser intensity, laser wavelength, and the analyzing wavelength.

Laser intensity and laser damage

In the present study, small laser intensities between 1-2 mJ/cm² were employed for the excitation of the TiO₂ powder samples. In agreement with the findings of Schneider *et al.*,¹¹⁷ higher laser pulse intensities result in permanent damage to the sample. One indicator of this permanent damage is represented by the fact that at very high laser energy densities the TiO₂ sample turns from white to grayish. Furthermore, at high photon flux (above 2-4 mJ/cm²) a large peak located at around 400 nm grows in the transient reflectance spectra (cf. **Figure 5.3A**). This observation has been made in the literature as well.¹⁴⁹ The influence of this irreversible change on the transient absorption spectroscopy, on the other hand, is shown and discussed here. In particular, the following observations were reported for the first time. The long-lasting effect, for instance, was confirmed by experiments monitoring the transient reflectance signal of the laser exposed sample. The damaged sample (exposed to 20 mJ/cm²) retains the large transient reflectance signal at 400 nm, even if small laser intensities of around 1 mJ/cm² are used (cf. **Figure 5.3B**).

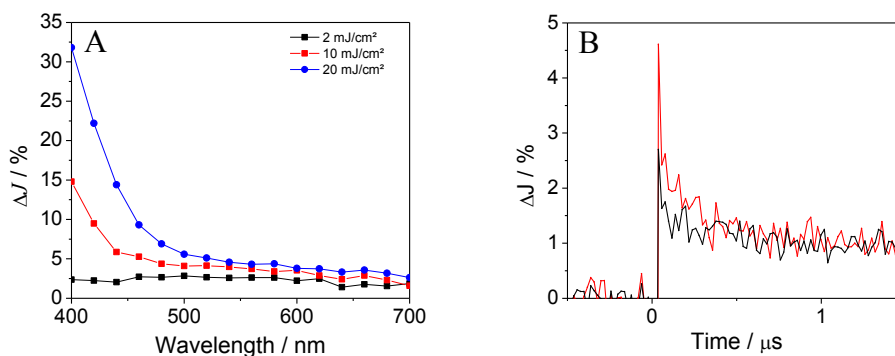


Figure 5.3: Transient reflectance spectra of charge carriers photo-generated in the TiO₂ powder sample (KronoClean7050) observed 80 ns after laser excitation with 2 (black), 10 (red) and 20 mJ/cm² (blue) (A) and transient reflectance signal at 400 nm of the TiO₂ powder sample (KronoClean7050) after laser excitation with 1 mJ/cm² either before (black) or after exposure to laser pulses with 20 mJ/cm² (red) (B).

The impact of the laser damage is mainly detected at the beginning of the signal (cf. **Figure 5.3B**). In the first 500 ns the transient reflectance signal is much larger after the exposure to high laser intensities, while the signal remains almost unchanged after the

exposure to high photon fluxes after 1 μs . Schneider et al. proposed a possible mechanism for the formation of these large 400 nm signals.^{117,149} The authors related the 400 nm signal to the formation of non-reactive electron species and observed the laser-induced transformation of anatase to rutile. The non-reactive Ti^{3+} centers in rutile increase the signal of photo-generated holes by coulomb interactions. Indeed, permanent damage to the sample and the accumulation of charge carriers in the sample caused by the energy transfer from the laser pulses to the TiO_2 lattice are valid assumptions and can explain the transient reflectance signals in the wavelength region between 400 and 500 nm detected in this study.

The accumulated exposure of a TiO_2 sample to 2000 laser pulses with 2 mJ/cm^2 did not cause any permanent damage to the sample. Therefore, in this work laser intensities in the range of $1\text{-}2 \text{ mJ/cm}^2$ were employed.

Several researchers also recommended the use of low laser intensities for the kinetic analysis of charge carrier recombination observed for TiO_2 .^{109,128,131,133} However, Yoshihara *et al.*, proposed that at small laser excitation intensities of $10\text{-}50 \mu\text{J/cm}^2$, the laser excitation has no influence on the charge carrier kinetics.¹⁰⁹ Nonetheless, the study displayed comparable changes of the charge carrier kinetics in the whole observed range of laser intensities. Furthermore, Tang *et al.* and Wang *et al.* assumed that at high laser intensities, higher than those employed in their studies, the charge carrier recombination follows a different kinetic model of charge carrier recombination.^{131,133} They suggested monoexponential or second order decays under this condition. Moreover, diverging time-scales are observed in the literature, despite the fact that the recombination mechanism can change at different times after the laser excitation.^{128,130,131}

The experimental setup, employed in this study for the observation of the transient reflectance signals, is unfortunately limited to a minimum excitation intensity of 0.5 mJ. Nevertheless, the following discussion will show that the laser intensity chosen here does not have an effect on the observed decay kinetics.

Excitation wavelength

In most experiments, the TiO_2 powder samples were excited with a 355 nm Nd-YAG Laser, since the bandgap energy of TiO_2 (3.0 to 3.4 eV) equals a minimum excitation wavelength of 365-415 nm.^{52,53} Nevertheless, excitation with energy exceeding the

bandgap may be possible. Laser excitation with wavelengths corresponding to higher energies, for instance 266 nm, might trigger additional energy levels and promote electrons to high energetic states. On the other hand, upon illumination with wavelengths higher than 415 nm, the electrons in TiO₂ cannot be excited from the VB into the CB. Therefore, no transient reflectance signal is expected for the utilization of visible light. The transient reflectance signals measured at 500 nm after laser excitation with 2 mJ/cm² employing excitation wavelengths of 266 nm, 355 nm, and 420 nm are shown in **Figure 5.4A**.

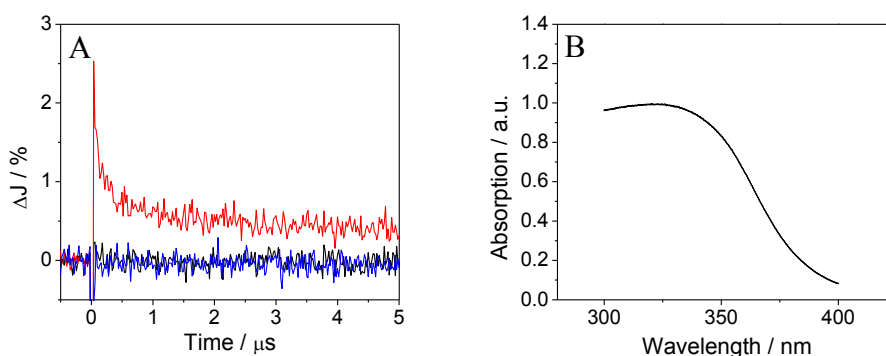


Figure 5.4: Transient reflectance signals of charge carriers photo-generated in the TiO₂ powder sample (KronoClean7050) measured at 500 nm after laser excitation with 2 mJ/cm² (λ_{ex} =266 nm (black), 355 nm (red), 420 nm (blue)) (A) and UV-Vis reflectance spectrum of TiO₂ (KronoClean7050) (B).

Despite the previously mentioned expectations for excitation with 266 nm, neither 266 nm nor 420 nm laser excitation were able to produce a transient reflectance signal of charge carriers in TiO₂ absorbing at 500 nm. Only with 355 nm laser excitation could the typical transient reflectance signal be obtained. Hence, the formation of trapped charge carriers in TiO₂ requires excitation with light which matches the bandgap energy of the semiconductor (cf. **Figure 5.4B**). Upon excitation with shorter wavelength no comparable amounts of trapped charge carriers are generated, possibly due to the 50 times lower penetration depths for 266 nm laser light in comparison to 355 nm laser light.¹⁵⁰ Indeed, Schneider also obtained a smaller transient reflectance signal for lower excitation wavelengths.¹⁴⁹ She correlated this observation with the higher number of oxygen vacancies produced upon illumination with higher energy. The number of oxygen vacancies, consequently, changes the alkalinity and the absorption coefficient of the trapped charge carriers.^{151,152}

It remains possible that excitation with 266 nm only generates a smaller fraction of trapped charge carriers in TiO₂. Nevertheless, repetition of the experiment employing higher laser

intensities did not change the trends detected in **Figure 5.4**. However, TRMC and PL measurements of TiO₂ were successfully carried out after excitation with 266 nm.^{115,133} Tamaki *et al.* also employed laser excitation with 266 nm for their transient absorption studies in the femtosecond time-scale.³³ Nonetheless, the authors used very small laser intensities of around 10 μJ /cm², and were therefore probably able to avoid the damage mechanisms mentioned above. The absence of a transient reflectance signal in the case of excitation with 420 nm proves that the transient signals are not generated by a simple thermal effect of the laser on the sample.

Analyzing wavelength

In this work, every TiO₂ powder sample employed shows broad transient reflectance signals between 400 and 700 nm decaying with a wavelength independent speed (cf. **Figure 4.2**). The transient signals at 500 nm are analyzed as representatives; therefore, the results obtained by the kinetic analysis of other wavelengths are expected to be comparable. This is confirmed by the fractal kinetics fit carried out for different analyzing wavelengths covering the range from 400 to 700 nm. The resulting fit parameters are shown in the appendix (cf. **Table S15**). Following the reported absorption coefficients of trapped holes and electrons by Friedmann *et al.*, the transient reflectance signal at 500 nm can be assigned to a 1:1 mixture of trapped electrons and trapped holes.¹⁴¹ **Figure 5.3A** confirms the assumption that a large signal of trapped holes is detected mostly below 400 nm, especially at laser intensities exceeding 2-3 mJ/cm².

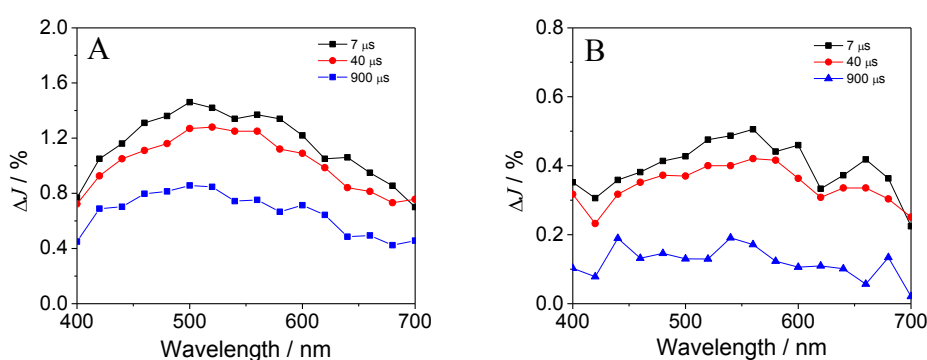


Figure 5.5: Transient reflectance spectra of charge carriers photo-generated in KronoClean7050 (A) and PC500 (B) observed at 7 μs (black), 40 μs (red), and 900 μs (blue) after laser excitation with 2 mJ/cm².

The conditions employed in this study, namely the inert N₂ atmosphere and the absence of scavenger molecules, result in a broad signal that represents a sum of the transient

reflectance signals of trapped electrons and trapped holes.⁴⁷ Nevertheless, at relatively long times after the laser excitation or at very low laser intensities, the transient reflectance spectra of PC500 and KronoClean7050 display a distinct band located around 500 nm (**Figure 5.5**).

The 500 nm band is observed in particular when small TiO₂ particles are employed. In the literature, this characteristic spectrum has been observed many times for colloidal TiO₂ samples or TiO₂ powder samples after excitation with low laser intensities.^{22,28,32,69,107,131} PC500 and KronoClean7050 contain TiO₂ particles with a primary particle size of 5-10 nm. Subsequently, the band might be related to the trapping of charge carriers on the TiO₂ surface. Moreover, this is in good agreement with the general finding that the trapping sites, such as surface hydroxyl groups, are mainly localized at the particle surface.^{133,153,154} The high surface/bulk ratio of PC500 and KronoClean7050 causes a higher number of charge carriers to be stabilized at the surface of these materials.

As mentioned in **Chapter 4.1.1**, discrimination between the different charge carrier species is not essential for the kinetic analysis of the recombination kinetics. Consequently, the transient reflectance signals are analyzed with the help of the following fit functions.

5.2 Analysis of charge carrier recombination kinetics

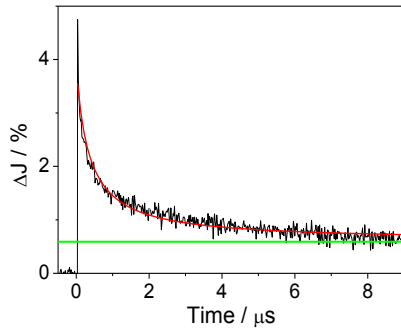
The following section discusses the different fit functions employed in this study. In particular, the differences between the second order fit, a fractal fit function, and a fit function based on a power law are investigated. The second order and the power law fits are discussed as border cases of the fractal kinetics model. Finally, the feasibility of the fractal kinetics fit function is analyzed for the recombination kinetics of photo-generated charge carriers in TiO₂.

5.2.1 Second order decay kinetics vs. fractal kinetics

Second order decay kinetics

The second order fit function with baseline (**Equation 4.1**) is utilized for the analysis of the transient reflectance signals at 500 nm observed for TiO₂. **Figure 5.6** illustrates that the second order fit function is not able to represent charge carrier signals in TiO₂ perfectly. Moreover, the level of agreement displayed is only achieved by the utilization of the baseline, shown in green. In the second order fit, the baseline is adjusted to maximize the

correlation of the data points and the fit function. The baseline was introduced in consideration of the fact that the signals are visually not decaying to zero,²² and to account for the permanent optical damage caused by the laser illumination.¹¹⁷



Second order fit function:

$$\Delta J = \frac{A}{1 + A \cdot k_2 t} + B$$

Figure 5.6: Transient reflectance signals of charge carriers photo-generated in N₂-saturated PC105 measured at 500 nm in the time domain 40 ns to 9 μs excitation (black), with second order kinetics fit with baseline (red).

However, the experimental conditions employed in this study were chosen to intentionally avoid any permanent changes to the material. In fact, even the accumulation of 2000 laser shots did not lead to any permanent optical change or remaining influence on the transient reflectance signals (cf. **Chapter 5.1.2**).

Despite the frequent application of this fit function including a baseline,^{22,30} the use of an arbitrary baseline is an inherent disadvantage. If the signals are observed for a longer time period, for instance, the signal decays further and approaches zero. Nevertheless, the transient charge carrier signal does not reach zero, which is in good agreement with the slower charge carrier recombination caused by the fractal-like kinetics.

In **Figure 5.7** the signal is shown on a longer time-scale until 900 μs and the figure includes the baseline (green) taken from the second order fit of the shorter time-scale (baseline of the fit shown in **Figure 5.6**).

Fitting of the transient reflectance signal shown in **Figure 5.7** leads to a new baseline, which does not agree with the baseline obtained by the second order fit shown in **Figure 5.6**. The baseline taken from the second order fit of one time-scale is obviously not equal to the baseline obtained by the second order fit in other time-scales. This inconsistency for different time windows was already discussed in **Chapter 4.1.2** and **4.1.3**.

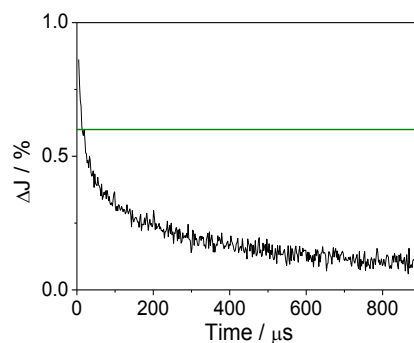


Figure 5.7: Transient reflectance signals of charge carriers photo-generated in N_2 -saturated PC105 measured at 500 nm in the time domain 6 μs to 1 ms after laser excitation, with baseline of the second order kinetics fit of the time domain 40 ns to 9 μs after excitation.

It should be mentioned here that the second order kinetics is based on free diffusion observed in classical homogeneous systems (cf. **Chapter 2.2.2**). This represents a main disadvantage, possibly limiting the application of the second order fit function to such systems. Hence, the second order fit function with baseline is not the best choice for the mathematical analysis of charge carrier recombination in TiO_2 powder samples.

Fractal-like kinetics in TiO_2 samples

In contrast to the second order approach, the fractal fit function (cf. **Equation 4.2**) shows excellent agreement with the experimental data points without requiring a baseline (cf. **Figure 4.7**). The fractal fit function employed in this study is based on the second order fit function and was improved by the multiplication of the rate constant with a time-dependent term.

The application of this fit function requires some assumptions. First, the fractal model proposes that the recombination of charge carriers on the TiO_2 surface can hardly be compared to similar reactions carried out in solution. The geometrical shape of the surface defined by the probability distribution of the trapped charge carriers after photo generation is not trivial. In addition to the complex nanostructured surface of one TiO_2 particle, more potential pathways for the charge carriers are provided by the contact of nearby nanoparticles. Similar to the antenna mechanism, which was proposed by Wang *et al.* in 2006, the charge carrier transfer between different TiO_2 particles plays an important role in the fractal model. The antenna mechanism presumes that the transfer of charge carriers between different TiO_2 particles is possible in agglomerates found in particulate

suspensions (**Figure 5.8**).¹⁵⁵ As discussed later in **Chapter 5.3.2.**, a similar mechanism is proposed for the powder samples employed in this work, where the adsorbed water molecules supports the formation of large TiO₂ agglomerates as well.

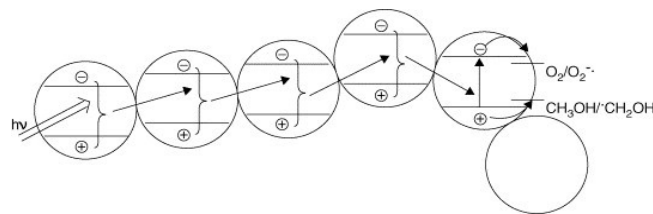


Figure 5.8: Antenna mechanism - Charge carrier transfer in TiO₂ networks. Reproduced from Ref. 156 with permission from The Royal Society of Chemistry.

Figure 2.8A shows such a fractal structure based on the assumption that in agglomerated clusters the charge carriers are trapped at the surface of the TiO₂ particles and that the charge carriers can easily be transferred to adjacent TiO₂ particles. Consequently, according to the model described by Kopelman (cf. **Chapter 2.2.3**), batch reactions on these fractal surfaces follow a time dependent rate constant k .¹¹⁶ In Kopelman's model, the time dependency of the rate constant is described by the multiplication of the rate constant with the time to the power of $-h$. The corresponding fractal parameter h is defined by the fractal dimension of the sample and typical h -values of fractal surfaces are $h = \frac{1}{3}$ and $h = \frac{1}{2}$.¹¹⁶

Kinetic analysis with the help of fractal models was employed beforehand; **Chapter 2.2.3** gives some examples from the studies found in the literature dealing with TiO₂ or similar systems. A few are named here to stress that agreeing time dependencies were detected in these studies. In 1983, Toussaint and Wilczek discussed an asymptotic $t^{-1/2}$ dependency of the second order rate coefficient for second order reactions on square lattices.^{36,157} Similarly, a $t^{-1/2}$ dependence of the second-order rate coefficient was reported by Grella and Colussi in 1996.^{36,116} In addition, the analysis of a random walk on fractal structures lead to an asymptotic t^α behavior for the mean-square displacement.¹⁵⁸ Just like the h parameter, the exponent α is a tool to describe the fractal geometry. In this case, α represents the ratio between the spectral and the fractal dimensions of the system. In summary, the fractal kinetics fit has seldomly been applied in photocatalysis, but the reports in the literature all point to a rather identical time dependency.

In **Chapter 4.1.3** the main advantages of the fractal kinetics fit, in contrast to the second order fit function with baseline, are given. In particular, the minimum number of fit parameters each possessing a distinct physical interpretation is one key argument in favor of the fractal kinetics fit. Further, the higher degree of accordance with the experimental transient reflectance signals, in the case of kinetic analysis employing the fractal kinetics model, should convince researchers to prefer the fractal model. Importantly, high conformity can be achieved without the need of a baseline. The typically employed arbitrary baseline covers part of the signal diverging from pure second order kinetics. Moreover, there is no reason for the signal to stabilize on a value unequal to zero, as long as small laser intensities are used. Only when high laser intensities are used, the permanent damage might cause the optical properties of the sample to differ from the starting conditions.¹¹⁷ The low laser intensities of 1-2 mJ/cm² employed in this study do not generate a permanent change in the sample in the observed time-scale; hence, a kinetic analysis omitting a baseline, such as the fractal kinetics fit, should be favored.

Dependency of the second order fit and the fractal fit on the time window

In contrast to the inconsistent fitting parameters obtained employing the second order fit function in different time-scales, which is described in **Chapter 4.1.2** and **4.1.3**, the results of the fractal kinetics fit function prove to be more reliable (cf. **Figure 4.9**). The fractal rate constant displays only a small deviation (10-20 %) for the analysis of the same signal in two time domains, while the change in the second order rate constant under the same conditions is 100-200 %. Furthermore, the coefficients of determination \bar{R}^2 observed for the application of the fractal fit function on the experimental data in the full time-scale of 40 ns to 1 ms are higher than the coefficients of determination of the second order fit function. The fitting parameters of the fractal fit function also display less scattering than the parameters of the second order fit function.

Despite the benefits of the fractal fit function listed above, both fitting models display a considerable change in the fit parameter A if the two time-scales are compared (cf. **Figure 5.9**). Identical to the observations made for the rate constants, the change in the fitting parameter A in the case of the second order fit function is slightly larger than for the fractal fit function. While the second order fit leads to a change of A in the order of 92 %, the fractal kinetics fit applied to the transient reflectance signals of the TiO₂ shows a 77 % change of the parameter A .

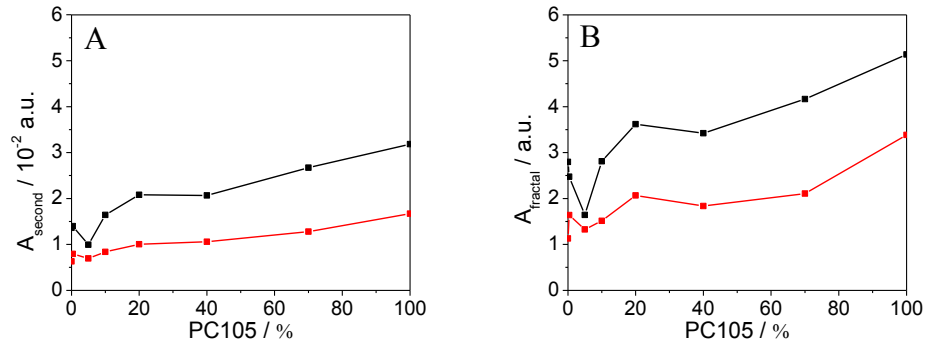


Figure 5.9: Fitting parameter A_{second} of the second order fit (A) and fitting parameter $A_{fractal}$ of the fractal kinetics fit (B) of the transient reflectance signals of charge carriers photo-generated in TiO₂ series containing PC105 and Kronos1001 measured at 500 nm employing the time-scale 5 μ s to 1 ms (red) and the full time-scale of 40 ns to 1 ms (black).

Generally, the literature employs second order decay functions particularly for the initial part of the charge carrier signal.³⁰ As long as the very beginning of the charge carrier signal is investigated, for instance in femtosecond studies, relatively short time-scales are observed. Subsequently, the variation of the time during the course of the experiment is negligible ($\Delta t \approx 0$).

$$k_f \approx k_{2,f} \cdot const \quad t^{-h} \approx const \quad for \quad \Delta t \approx 0 \quad (5.1)$$

Equation 5.1 shows that for small time changes the influence of the fractal kinetics on the decay constant is negligible and, hence, classical second order kinetics is observed (c.f. **Equation 4.1**). The long-lasting components of the signal containing more complex kinetics are hidden by the baseline (cf. **Chapter 5.2.1**). Therefore, the second order fit function represents a border case of the fractal kinetics fit for comparatively small time-scales.

Dependency of the second order fit and the fractal fit on the laser intensity

An increase in laser intensity leads to faster decay rates of the transient reflectance signals. This trend of faster decay rates for higher laser intensities can be explained by the bimolecular reaction mechanism. According to the second order mechanism, the recombination rate depends on the charge carrier concentration. The greater amount of light generates more charge carriers in the material and, therefore, a faster recombination speed is detected. Indeed, higher laser intensities generate more charge carriers per semiconductor particle (cf. **Figure 4.5**) and decrease the detected half-life of the signal.

Theoretically, the detected recombination constants should not be influenced by the variation of the laser intensity. Indeed, the analysis of the transient reflectance signals under varying laser intensities (0.6-5 mJ/cm²) reveals relative constant values for the second order rate constant and the fractal rate constant (cf. **Figure 4.6** and **Figure 4.10**). This is in good agreement with the second order recombination mechanism mentioned above. The higher concentration of charge carriers leads to a faster decrease in the transient signal, but demonstrates a rather steady recombination constant.

Nonetheless, a slight trend towards lower recombination constants at higher laser intensities was observed for the second order rate constant. Similarly, the analysis of the charge carrier recombination with the help of the fractal fit function shows lower fractal rate constants at higher laser intensities as well (cf. **Figure 4.10**). However, the higher rate constants for the smallest laser intensities of 0.6 mJ/cm² and 1 mJ/cm² might be influenced by the lower signal-to-noise ratio of the respective transient signals. The low signal height of the transient signal detected at 0.6 mJ/cm² indeed worsens the correlation between the fit function and the data points ($\bar{R}^2 = 0.85$). The transient signals obtained at higher laser intensities displayed much larger reduced coefficients of determination ($\bar{R}^2 > 0.94$). The respective transient signals and the correlating fit functions for 0.6 mJ/cm² and 5.1 mJ/cm² are shown in the appendix (**Fig. S16**).

In the absence of the above-described influence of the low signal-to-noise ratio, a uniform fractal rate constant for varying laser intensities is expected for the fractal kinetics fit and the second order fit. Within the area of laser intensities utilized in this study (1-2 mJ/cm²), the fitting process leads to nearly constant values for the decay constants. Thus, the influence of the variation of the laser intensity on the kinetic constants is expected to be small.

Similarly, the rise of the laser intensity causes no detectable influence on the fractal parameter h (cf. **Figure 4.11**). The change of the fractal parameter h would correspond to a change in the fractal structure. Since a constant fractal parameter h was detected, the fractal parameter might be an intrinsic property of the sample.

Nonetheless, only relatively small variations in the laser intensity were tested here. At higher laser intensities, the fractal parameter obtained for PC105 might differ from the value observed at lower laser intensities. This change could then be related to a

transformation in the spatial probability distribution of the trapped charge carriers. Indeed, at higher laser intensities a trap-filling effect has been reported.¹²⁸ After exposure to high laser intensities, the larger amount of photo-generated charge carriers occupy many trap states.¹⁰⁹ Due to the limited availability of traps, the mobility of free charge carriers increases.¹³³ In this case, the spatial distribution of the charge carriers is, logically, a function of the laser intensity. A significantly higher concentration of free and trapped charge carriers in the material enhance the coulomb interactions between the charged particles.¹⁴⁹ Hence, at higher laser intensities the coulomb interactions can change the effective fractal surface resulting in modification of the fractal parameter h . The higher charge carrier population might cause a higher fraction of trapped states being located in the bulk instead of on the surface of the particles. In short, at higher excitation intensities the effect might be abstracted as a shift of the surface/bulk ratio of trapped charge carriers.

Indeed, after exposure of the sample to high photon fluxes of 20 mJ/cm^2 different kinetic parameters are obtained for the fractal kinetics fit applied to the transient reflectance signal at 400 nm of TiO_2 after laser excitation with 1 mJ/cm^2 (**Figure 5.10**). In comparison to the other fitting results observed for KronoClean7050, a large fractal parameter of 0.85 and a low coefficient of determination ($\bar{R}^2 = 0.33$) were obtained. The change of the fractal parameter can be correlated with a change of the fractal geometry of the sample, while the low coefficient of determination indicates that the charge carrier kinetics in the TiO_2 sample after exposure to 20 mJ/cm^2 might not correlate with the fractal model anymore.

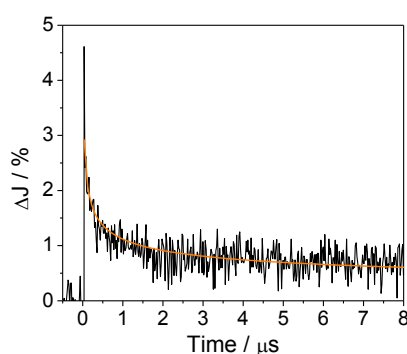


Figure 5.10: Transient reflectance signal at 400 nm of the TiO_2 powder sample (KronoClean7050) after laser excitation with 1 mJ/cm^2 after exposure to 20 mJ/cm^2 laser pulses (black) with fractal kinetics fit (orange).

5.2.2 Fractal kinetics vs. power law decay

In addition to the utilization of a fractal fit function or a second order fit function, the charge carrier recombination in TiO₂ can be described according to a power law model (**Equation 5.2**). This model was developed by Shuttle *et al.* and the characteristic linear function observed in double logarithmic plots is illustrated in **Chapter 2.2.4**.¹²⁹ Before the mathematical correlation between the fractal kinetics model and the power law model can be discussed, the fundamental differences need to be clarified.

$$\Delta J = At^{-x} \quad (5.2)$$

The basic assumptions of the power law model diverge from those assumptions made for the fractal fit function (cf. **Chapter 2.2.3**). First, the power law model excludes the transfer of charge carriers between different particles and supposes immobile hole species.¹²⁸ Furthermore, according to Shuttle *et al.*, the model is applicable for small laser intensities and at long times after the excitation.^{129,131} Unfortunately, the authors do not provide information concerning the time interval between charge carrier excitation and the observation time required for the application of their model. Furthermore, the power law model does not consider that the recombination reaction is also influenced by structural parameters (e.g. the random walk mechanism) at short times after the generation of charge carriers.¹²⁸

Apart from the different assumptions of the two fit functions, the mathematical relationship between the fractal kinetics model and the power law model should also be discussed here. Generally, the power law approach displays the charge carrier signal over a broad range of time-scales in double logarithmic plots. The double logarithmic plot can also be utilized to show the transient reflectance ΔJ in the course of time for the fractal fit function (cf. **Equation 4.2**).

$$\log(\Delta J) = \log(A(1-h)) - \log((1-h) + Ak_{2,f}t^{1-h}) \quad (5.3)$$

The power law is typically applied a long period of time after laser excitation $t \gg 0$, subsequently, $Ak_{2,f}t^{1-h} \gg 1-h$, and $(1-h) + Ak_{2,f}t^{1-h} \approx Ak_{2,f}t^{1-h}$. Hence, **Equation 5.3** can be simplified to **Equation 5.4** revealing a linear dependence between the logarithmic change in reflectance and the logarithmic time.

$$\log(\Delta J) = \log(A(1-h)) - (1-h) \cdot \log(Ak_{2,f}t) \quad \text{for } t \gg 0 \quad (5.4)$$

Consequently, the fractal kinetics model displays a linear function in the double logarithmic plot a long period of time after the excitation, comparable to the power law approach. The power law model can be seen as the border case a long period of time after the laser excitation and employing low laser intensities.¹²⁹ The slope of the linear function x in the double logarithmic plot of the charge carrier population against the time is equal to $-(1 - h)$ (**Equation 5.5**).

$$x = -(1 - h) \quad (5.5)$$

Similarly, if the second order rate constant is plotted against the time in double logarithmic plots, **Equation 2.11** is linearized to **Equation 5.6**.

$$\log(k_2) = \log(k_{2,f}) + (-h) \cdot \log(t) \quad 0 \leq h \leq 1 \quad (5.6)$$

The slope of the linear function in the double logarithmic plot of the rate constant against the time consequently equals $-h$.

The transient reflectance measurements of the TiO₂ samples in this thesis were carried out under relatively low laser intensities of 1-2 mJ/cm² and were observed between 40 ns and 1 ms. Therefore, the applied experimental conditions are nearly identical to the requirements mentioned above for the application of the power law model. Subsequently, a linear trend for the charge carrier signals over the course of time employed is expected for the double logarithmic presentation.¹²⁹

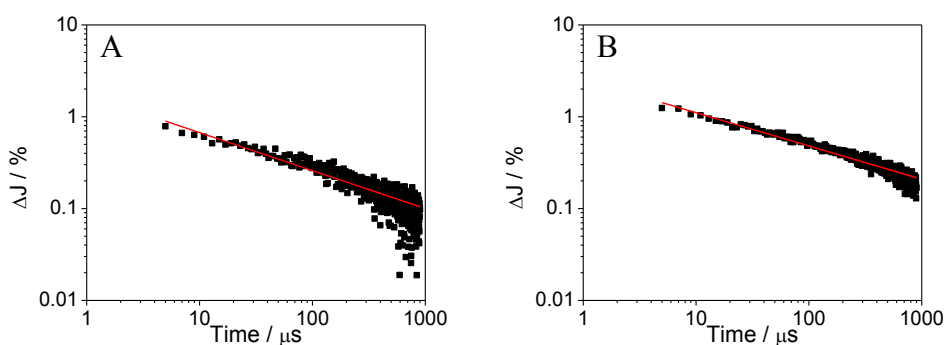


Figure 5.11: Double logarithmic plot of the transient reflectance signals of charge carriers photo-generated in PC105 measured at 500 nm (black) and power law fit (red) after excitation with 0.6 mJ/cm² (A) and 5.1 mJ/cm² (B) ($\lambda_{ex} = 355 \text{ nm}$). Reprinted from Ref. 134.

Indeed, the experimental results obtained in this study illustrated in double logarithmic plots (**Figure 4.8** and **Figure 4.13**) indicate such a linear tendency. Hence, the power law

fit is applied to the transient reflectance signal at 500 nm observed for PC105. **Figure 5.11** illustrates the corresponding double logarithmic plots of the change in reflectance and the power law fit functions ($\Delta J = At^{-x}$) at high and low laser intensities (5 mJ/cm² and 0.6 mJ/cm², respectively). The complete set of fitting parameters is given in the appendix (**Table S17**).

The power law fit of the transient reflectance signal obtained for PC105 reveals a relatively fair agreement with the experimental data points (**Figure 5.11**). The slope of the linear fit functions x is -0.36 and -0.41 for the laser intensities of 5.1 mJ/cm² and 0.6 mJ/cm², respectively. This suggests that a smaller laser intensity leads to a more negative exponent x . This correlates well with the asymptotic $t^{-1/2}$ dependency reported by Toussaint and Wilczek.¹⁵⁷ Following the simplification made in **Equation 5.3**, the exponent of -0.5 from their model correlates with an h -parameter of 0.5. Hence, for such bimolecular reactions on square lattices observed a long period of time after the excitation $h = 0.5$. Clearly, the exponent obtained employing the smaller laser intensity shows a better correlation with the predictions made by Toussaint and Wilczek. This is excellent evidence for the limitation that the model is only applicable for small laser intensities and a long period of time after the excitation.^{129,131}

The fractal model and power law kinetics are both based on bimolecular recombination dynamics. Subsequently, to explain the observed differences, the discrepancies between the two models need to be discussed. Instead of the assumption of mobile electrons and stationary targets (holes), which are expected in the power law model, the fractal model supposes that both trapped charge carriers show an identical mobility.^{130,134} In addition, the electrons in the power law approach need to be detrapped thermally, and an exponential distribution of trap states is assumed.¹²⁸⁻¹³⁰ The fractal kinetics fit, on the other hand, adopts a spatial segregation of charge carriers leading to a deviation from classical second order kinetics. In sum, similar processes are the basis of both models, but some general assumptions contradict each other.

Consequently, these experimental results indicate that charge carrier signals obtained by employing high laser intensities such as 5.1 mJ/cm² should not be fitted with the power law model. Furthermore, both transient reflectance signals in **Figure 5.11** display a rather unsatisfactory fit with the experimental data points. Indeed, the slope of the data points over the course of time in the double logarithmic plot changes. A linear fit function is not

able to represent the data points over a broad time-scale. **Figure 5.12** displays the linear fit function of the transient reflectance observed for PC105 in the double logarithmic plot in the time-scale between 40 ns and 1 ms.

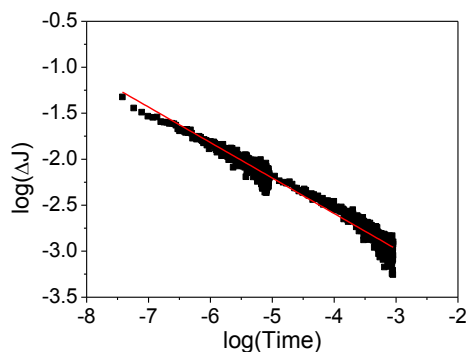


Figure 5.12: Double logarithmic plot of the transient reflectance signals of charge carriers photo-generated in PC105 measured at 500 nm (black) and linear fit based on a power law (red) in the time domain 40 ns to 1 ms.

In contrast the fractal kinetics fit function (cf. **Figure 4.8**), the simple power law ($\Delta J = At^{-x}$) is not able to describe the charge carrier recombination kinetics at the selected laser intensity and time window, as shown above. Nevertheless, the power law model has been identified as a border case of the fractal model, provided that low laser intensities below 1 mJ/cm² are used and given that the signals are observed a long period of time after charge carrier generation (millisecond to second time-scale). Hence, the asymptotic linear behavior of the charge carrier signals observed in the double logarithmic plot correlates well with the fractal kinetics approach shown in **Equation 4.2**.

5.2.3 Model of charge carrier segregation on surfaces

In addition to the theoretical, mathematical, and experimental comparison of the fractal fit function with the second order fit or the power law model, a pure empirical model is analyzed here. The model represents a sum of surfaces, each following second order kinetics. The concentration of charge carriers on each surface is not uniform, based on the potential distribution of charge carriers after segregation.

The nanostructured surface of the TiO₂ particles and the microstructure generated by the agglomeration of particles defines the area available for the movement of the trapped charge carriers. This area can be described by employing fractal dimensions and such fractal surfaces are well known for causing segregation of the reactive species.¹¹⁶

Consequently, the effect of segregation on the second order kinetics is modeled by employing the sum of ten surfaces or ten separated particles. Each surface has a different starting concentration of charge carriers but solely follows second order recombination kinetics, while the sum of the hole species is always identical to the number of electrons. This inhomogeneous distribution of charge carriers can easily be generated by the inhomogeneous absorption coefficient of UV-light in the material.¹⁵⁹ Indeed, the analysis of optical properties generally includes the assumption that the whole sample has homogeneous optical properties, which is not true for the materials employed in this study.^{160,161}

All parameters of the model are given in **Table 5.1**. The results obtained employing the model of multiple bimolecular reactions after segregation are shown in **Figure 5.13** to **Figure 5.15**. In each figure the modeled total number of charge carriers is given over the course of time and in each figure another fit function or linearization of a fit function is employed.

Table 5.1: Parameters of the model of a bimolecular reaction on a surface after segregation. Reprinted from Ref. 134.

	Values
Rate law	$-d[e^-]/t=k[e^-][h^+]$
Initial trapped charge carrier concentrations	5000; 3500; 1000; 499; 50; 20; 10; 5; 2; 1 charge carrier particle ⁻¹
Rate constant	10 particle charge carrier ⁻¹ s ⁻¹
Step size	1 μs
Number of steps	2000

Figure 5.13A shows the linearization of a single exponential function. In the case of a first order reaction, a linear trend should be visible in the logarithmic plot of the number of charge carriers. This displays that the data do not follow first order kinetics.

On the other hand, **Figure 5.13B** illustrates the inverse plot of the number of charge carriers over the course of time. In the case of second order kinetics, the graph in **Figure 5.13B** should easily be represented by a straight line. The experimental results show that

even though the model is based on a sum of second order reactions, the modeled number of charge carriers does not agree with second-order kinetics.

The red line in **Figure 5.13B** indicates the linear trend of the modeled charge carrier population at the beginning of the time scale (0 μs to 50 μs). The linear trend line indicates the deviation of the aforementioned linear trend at long times (between 150 μs and 200 μs). In this time-scale, the time dependency of the inverse charge carrier population does not show the second order behavior. The remaining number of charge carriers at the end is larger than expected for the long-term trend of a second order reaction. Hence, the decay of the signal or overall recombination of charge carriers is slower at the end of the selected time-scale.

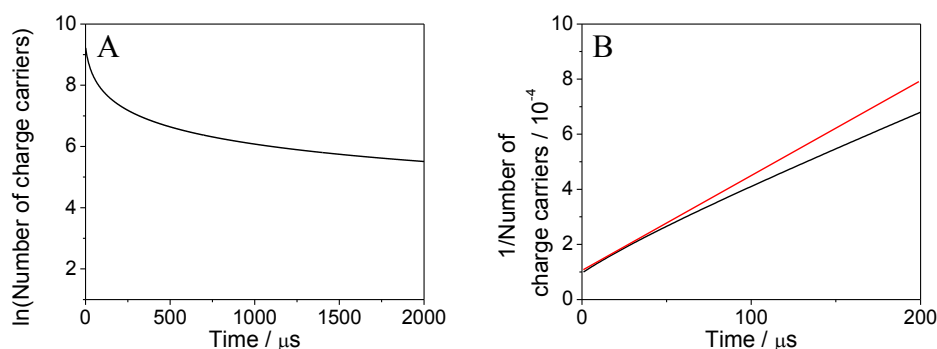


Figure 5.13: Logarithmic plot of the modeled charge carrier population (A) and inverse plot of the modeled charge carrier population (black) with linear fit (red) (B). The data points were taken from the model of a bimolecular reaction on the surface after segregation as defined in **Table 5.1**. Adapted from Ref. 134.

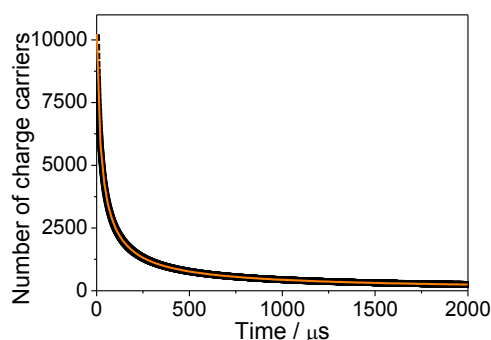


Figure 5.14: Course of the number of charge carriers taken from the model of a bimolecular reaction on the surface after segregation (black) and bimolecular fit based on fractal-like kinetics (orange). Reprinted from Ref. 134.

Table 5.2: Results of the second order fit with (Equation 4.1) and without baseline and the fractal-like kinetics fit (Equation 4.2) applied to the model of a bimolecular reaction on the surface after segregation. Adapted from Ref. 134.

Fit function	Second order without baseline	Second order with baseline	Fractal kinetics
$k / 10^4 \text{ a. u.}$	13.4	15.7	3.7
$A / 10^{-2} \text{ a. u.}$	18	9	22
h	0	0	0.14
\bar{R}^2	0.992	0.998	0.999

The observations are in good agreement with the findings observed for the application of the second order fit shown in Chapter 5.2.1. In small time periods, such as at the very beginning of the signal, the signal can be fitted with second order kinetics, since the change in the rate coefficient during that time is negligible. However, a second order fit is not able to describe the charge carrier recombination over a long time-scale.

Figure 5.14 shows the modeled number of charge carriers against time together with the corresponding fractal kinetics fit function. Table 5.2 illustrates the fitting parameters of the fractal kinetics fit and the second order fit with baseline and without baseline.

Interestingly, the model of bimolecular charge carrier recombination on ten surfaces with different starting concentrations of charge carriers results in a deviation of the second order kinetics, which could successfully be fitted to the fractal-like kinetics approach (Figure 5.14).

While the pure second order fit function without a baseline showed a correlation of $\bar{R}^2 = 0.992$, the fractal kinetics fit revealed a higher correlation of $\bar{R}^2 = 0.9999$. Due to the small number of modeled particles, the discrepancy between the two fit functions is small. However, Figure 5.13B and Figure 5.14 demonstrate that the fractal fit function represents a better description of the results obtained from the modeled charge carrier population. The small disparity between the two fit functions causes a relatively small fractal parameter h (0.14). Subsequently, a higher complexity in the modeled charge carrier population, such as a greater number of different particles/surfaces in the model, is expected to correlate with higher fractal parameters.

At last, the modeled charge carrier population is analyzed employing a power law decay. Such power law decays can be identified as linear functions in the double logarithmic plot. Hence, the modeled charge carrier population is shown in such a double logarithmic plot in **Figure 5.15**.

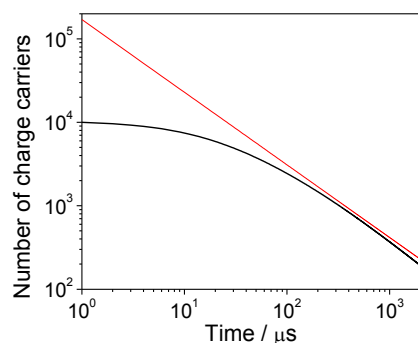


Figure 5.15: Double logarithmic plot of the charge carrier concentration taken from the model of a bimolecular reaction on the surface after segregation (black) and straight line with slope -0.87 (representing a linear dependency derived from a power law function) (red). Reprinted from Ref. 134.

At first sight, the modeled charge carrier population does not follow a simple power law, since no linear trend is observed in **Figure 5.15**. However, for long reaction times a linear function with a slope of -0.87 (red line in **Figure 5.15**) is in good agreement with the modeled charge carrier population. According to **Equation 5.5**, the slope of the linear function is equal to a fractal parameter of 0.13 . This correlates well with the fractal parameter of 0.14 obtained from the fractal kinetics fit of the modeled charge carrier population (cf. **Table 5.2**).

In good agreement with the results obtained at high laser intensities of 5 mJ/cm^2 (cf. **Figure 5.11**), **Figure 5.15** shows that the modeled charge carrier population does not follow a power law decay at the very beginning of the observed time-scale. Identical to the finding in **Figure 5.13B**, the charge carrier recombination in this time period is slower than expected from the linear trend at long times. Finally, the linear trend of the charge carrier population at long times correlates well with the possible applications of the power law model at long times and low laser intensities.

At low laser intensities of 0.6 mJ/cm^2 an exponent of 0.41 is obtained (cf. **Figure 5.13**), which is comparable to the theoretical value of 0.5 for $A+B$ reactions on square lattices.¹⁵⁷ Hence, the power law model proves to be applicable mainly at such low laser intensities.

Data obtained at laser intensities equal to or smaller than 1 mJ/cm^2 and in time domains beginning in the microsecond scale can be fitted to the power law model.

Indeed, the observations made in this study agree with the findings of Tang *et al.* reporting that at very high laser intensities monoexponential decays, instead of power law kinetics, are required for the analysis of recombination kinetics in TiO_2 .¹³¹ Nonetheless, the fractal kinetics fit can be used under these conditions as well. The differences between the two models were already discussed in detail in **Chapter 5.2.2**.

Therefore, if laser intensities above 2 mJ/cm^2 and shorter time-scales (nanosecond time-scale) are employed, the fractal-like kinetics approach (**Equation 4.2**) facilitates the calculation of reliable and comparable fit parameters independent from the time-scale observed. In contrast, the power law fit is unable to do so. A detailed discussion of the physical meaning and the applicability of the fractal fit parameters can be found in **Chapter 5.2.5**.

To the best of the author's knowledge, there is currently no model described in the literature that is feasible for the analysis of charge carrier dynamics in both short and long time-scales and at low and high laser intensities. Therefore, the fractal kinetics fit derived from the work of Kopelman closes the gap between the fast initial second order processes of the charge carrier signals and the long-lasting power law decays.

5.2.4 Application of the fractal fit function on the experimental data

In the present study, the transient reflectance signals of charge carriers photo-generated in TiO_2 were detected at 500 nm and analyzed employing a fractal kinetics fit function. These charge carrier signals were selected as representatives. Nonetheless, the practicability of the fractal kinetics approach is investigated here by analyzing of the charge carrier signals observed for PC105 over a broad wavelength range (400 to 700 nm). The corresponding charge carrier signals were fitted with the fractal kinetics fit and the obtained parameters are listed in the appendix (**Table S15**).

Figure 5.16 displays the fractal parameter obtained from the fractal kinetic fit plotted against the wavelength employed. The analysis of the spectroscopic range (400 to 700 nm) reveals nearly identical kinetic parameters. Moreover, the coefficients of determination were all in the range of 0.95 to 0.98, only the fit functions carried out at the wavelengths

640-700 nm displayed smaller coefficients of determination between 0.8 and 0.9 (cf. **Table S15**). This lower accuracy can be explained by the lower signal-to-noise ratio of the employed photomultiplier at higher wavelengths. The average fractal parameter h obtained for PC105 in this wavelength region is 0.65 (cf. **Figure 5.16A**). Therefore, the fractal parameter is kept constant at 0.65 to investigate the change of the fractal rate constant at different analyzing wavelengths (cf. **Figure 5.16B**).

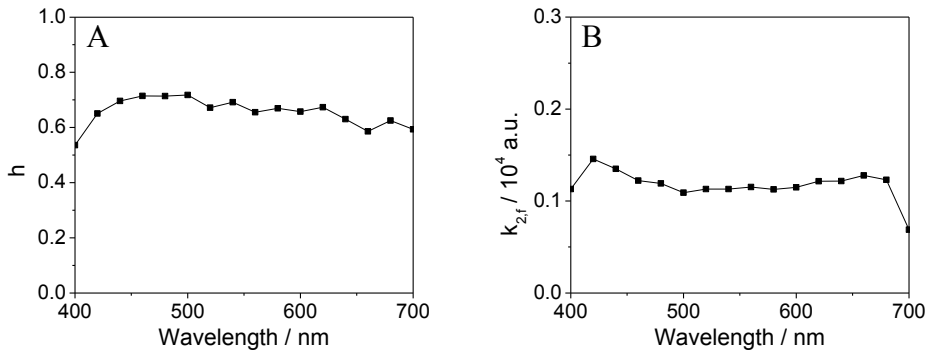


Figure 5.16: Fractal parameter h (A) and fractal rate constant $k_{2,f}$ (B) taken from the fractal kinetics fit of the transient reflectance signals of charge carriers photo-generated in TiO_2 (PC105) measured at 500 nm after laser excitation with 1 mJ/cm^2 ($\lambda_{ex} = 355 \text{ nm}$) plotted against the analyzing wavelength.

It appears that the analysis of the charge carrier kinetics leads to similar results for the analyzing wavelengths between 400 and 700 nm. The fractal rate constant stays constant for wavelengths between 460 and 680 nm and only small variations of the fractal rate constant are detected at the edges of the detected wavelengths area, namely, around 400 and 700 nm. Overall, the analysis of the charge carrier signals in the wavelength domain between 460 and 680 nm displays quite constant results. This proves that the same charge carrier signal is indeed detected at the chosen wavelength range, which was already assumed from the comparison of the transient reflectance spectra at different times after the laser excitation (cf. **Figure 4.2**).

As mentioned above, the average fractal parameter taken from the fractal fit of the transient reflectance observed for PC105 is 0.65 (cf. **Figure 5.16**). This value is very close to the theoretical value of $h = 0.5$ derived from the work of Toussaint and Wilczek.¹⁵⁷ The small deviation can be explained by the selection of the time-scale and the laser intensity of 1 mJ/cm^2 . In the previous chapter it was shown that the fractal parameter approaches the value of 0.5 at very small laser intensities, such as 0.6 mJ/cm^2 . The parameter 0.5 represents the ideal value for square lattices at long times. Nonetheless, the analysis of the

charge carrier recombination at a laser intensity of 0.6 mJ/cm^2 would not be optimal, since the signal-to-noise ratio is worse compared to the laser intensity of $1\text{-}2 \text{ mJ/cm}^2$ utilized in this work.

Moreover, the theoretical value of the fractal parameter is only expected for ideal bimolecular reactions on square lattices at long times. Real powder surfaces, such as those employed in this work, most certainly deviate from square even surfaces. This can lead to more complex behavior. This explains the observed exponent of 0.65 instead of 0.5 , since the h parameter is related to the structure of the sample.

Consequently, the effect of the fractal surface on the exponent h is tested by the investigation of charge carrier signals for different TiO_2 powders, such as the commercially available Kronos1001 and PC500 samples. **Figure 5.17** shows that, equivalent to PC105, a good agreement between the experimental data points and the fractal kinetics fit function is achieved for the two TiO_2 powders. Furthermore, the fit parameters of the two corresponding fit functions are given in **Table 5.3**.

In **Table 5.3** a large variation in the fractal rate constant is observed. Kronos1001 displayed a $k_{2,f}$ value of 1.6 , while PC500 showed a $k_{2,f}$ value of 0.04 . Moreover, the signal height A varies by a factor of 24 and the fractal parameters h change from 0.56 to 0.76 , while the fit functions of both samples revealed high coefficients of determination (0.92 to 0.94). Interestingly, the charge carrier signals in the three TiO_2 powders displayed a systematic change of the exponents h and the fractal rate constant. The influence of the sample properties on the charge carrier dynamics is investigated in detail in **Table 5.3**.

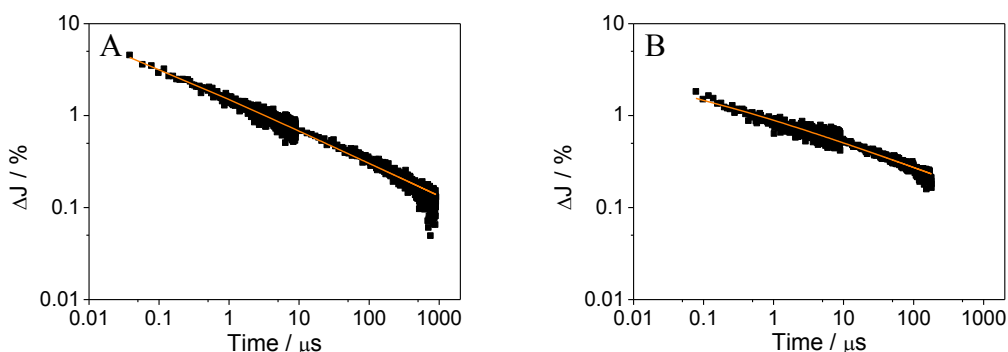


Figure 5.17: Transient reflectance signals of charge carriers photo-generated in Kronos1001 (A) and PC500 (B) measured at 500 nm after laser excitation ($\lambda_{ex} = 355 \text{ nm}$) (black) and bimolecular fit based on fractal-like kinetics (orange). Reprinted from Ref. 134.

Table 5.3: BET surface areas, primary particle sizes, and parameters obtained employing the fractal kinetics fit of the transient reflectance signals of charge carriers photo-generated in Kronos1001, PC105, and PC500 measured at 500 nm after excitation with 1 mJ/cm² ($\lambda_{ex} = 355 \text{ nm}$) in the time domain from 40 ns to 1 ms. Adapted from Ref. 134.

Sample	Kronos1001	PC105	PC500
$k_{2,f} / 10^4 \text{ a. u.}$	1.60	0.20	0.04
$A / \text{a. u.}$	4.1	7.6	48
h	0.56	0.62	0.76
\bar{R}^2	0.92	0.99	0.94
$\text{BET} / \text{m}^2 \cdot \text{g}^{-1}$	11	81	309
Primary particle size / nm	150	20	7.5

The sample properties and fitting parameters shown in **Table 5.3** prove the correlation between the sample properties and the charge carrier kinetics, analyzed with the help of the fractal kinetics fit. **Table 5.3** indicates an increasing trend in the fractal parameter and a decreasing trend in the fractal rate constant for the samples containing smaller particles. Subsequently, it can be deduced that the TiO₂ powder samples with various primary particle sizes exhibit different fractal surfaces and, subsequently, show a different fractal parameter h . Hence, the fractal parameter depends on the morphological properties of the sample. **Figure 5.18** displays the correlation of the fitting parameters taken from the fractal kinetics fit and the particle size of the commercial TiO₂ samples.

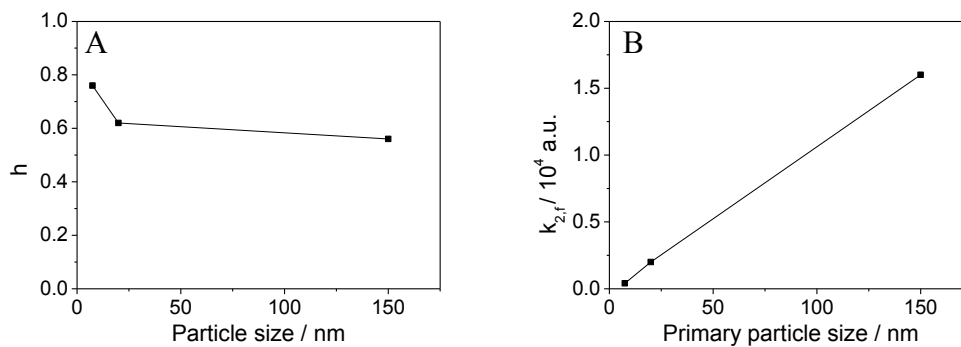


Figure 5.18: Fractal parameter h (A) and fractal rate constant (B) taken from the fractal kinetics fit of the transient reflectance signals of charge carriers photo-generated in commercial TiO₂ powder samples (Kronos1001, PC105, PC500) measured at 500 nm after laser excitation with 1 mJ/cm² ($\lambda_{ex} = 355 \text{ nm}$) plotted against the primary particle size.

Kronos1001, for instance, possesses the largest particle size and displays an h value of 0.47, in good agreement with the expected behavior on even surfaces. PC105 and PC500, on the other hand, display fractal parameters of 0.62 and 0.71, respectively (cf. **Figure 5.18A**). The higher h parameters are obtained for the samples consisting of small particles (PC105 and PC500). Hence, it can be concluded that the agglomeration of the small particles creates a fractal surface and, accordingly, the fractal parameter h changes from 0.47 (Kronos1001) over 0.63 (PC105) to 0.7 (PC500).

Figure 5.18B displays the almost linear trend in the fractal rate constant at different primary particle sizes. It appears that the smaller particle size in PC105 and PC500 causes a smaller fractal recombination constant. The smaller charge carrier recombination in smaller particles can be related to the beneficial surface/bulk ratio. The higher surface area of the particles facilitates efficient charge carrier trapping and reduces the observed recombination constant. The effects are further discussed in **Chapter 5.3.1** which deals with TiO₂ samples with binary particle size distribution.

5.2.5 Fractal kinetics fit as a meaningful kinetic analysis?

In the previous chapter, it was shown that the fractal kinetics fit can be utilized to achieve comparable and feasible fit parameters for the transient reflectance signals in TiO₂. For instance, the application of the fit function in the spectroscopic range between 400 and 700 nm revealed constant fit parameters. The fit function applied to the same transient reflectance signals, detected in two different time-scales, showed only small variations in the two kinetic fit parameters h and $k_{2,f}$. Moreover, in accordance with the present work, the stochastic fractal model of Grela and Colussi has been reported to successfully fit transient absorption signals of the charge carriers observed in TiO₂ colloids of different sizes and at different laser intensities.³⁶

Consequently, the fractal kinetics fit would be a very versatile model if it were applicable on every detected transient signal of charge carriers photo-generated in semiconductor materials. In the first step to evaluate the applicability of the fractal model, it must be assessed in this work whether the application of the fractal fit is limited to transient reflectance data observed for TiO₂. As mentioned in the theoretical background, the charge carriers photo-generated in TiO₂ can be detected by PL and TRMC as well. Furthermore, similar to the correlations made in this study, an elongated lifetime of the TRMC signal in

octahedral anatase nanoparticles has recently been correlated with the higher photocatalytic performance of the respective particles.¹⁶² The fractal kinetics fit function on TRMC data observed for TiO₂ is shown in **Figure 5.19** (the TRMC data of P25 under Ar or N₂, after laser excitation at 355 nm have been provided by Prof. Christophe Colbeau-Justin; Université Paris-Saclay).

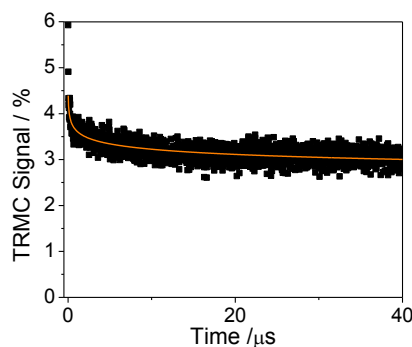


Figure 5.19: TRMC signal of P25 under Ar or N₂ after laser excitation ($\lambda_{ex} = 355 \text{ nm}$) (black) and fractal-like kinetics fit (orange).

Despite the visual concordance of the TRMC data and the fit function, the application of the fractal model on the TRMC data was not completely successful. The P25 sample displays an h parameter of 0.95 and a relatively low accuracy coefficient of determination (0.53). The other fit parameters are given in the appendix (**Table S18**). The observed differences might be influenced by the fact that P25 is not a pure anatase sample. P25 contains the two TiO₂ polymorphs anatase and rutile. However, recombination kinetics comparable to the anatase samples is expected for P25 investigated by TAS measurements. The results indicate that the fitting process is possible but the transient reflectance spectroscopy and the TRMC analysis results in the observation of physically different phenomena.¹⁶³

The problem might be that in the TRMC method mainly the free charge carriers in the semiconductor are detected, due to the larger influence of mobile free charge carriers on the microwave conductivity in comparison with free holes or trapped charge carriers.¹⁰⁵ Both studies (TRMC and TAS) detect charge carrier recombination. Nevertheless, in TRMC the trapping of free electrons and the recombination of free electrons and free or trapped holes is observed. TAS, on the other hand, shows the recombination of trapped electrons with trapped holes (**Figure 5.20A**). **Figure 5.20B** shows further that the

beginning of the TRMC signal does not correlate with the fractal or the power law fit function. Most likely, during the first 40-50 ns the signal decay might be influenced mainly by free charge carrier recombination instead of trapping processes.¹⁰⁶

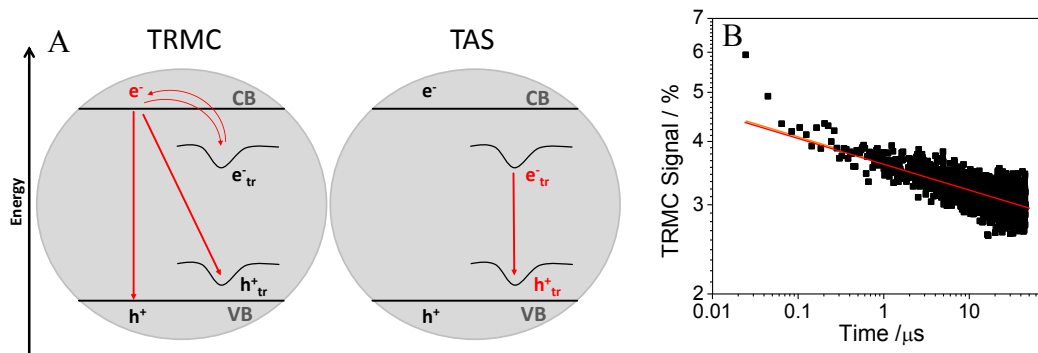


Figure 5.20: Charge carrier recombination mechanisms after laser excitation in TRMC and TAS (A) and double logarithmic plot of TRMC signal of P25 under Ar or N₂ after laser excitation ($\lambda_{ex} = 355 \text{ nm}$) (black) with power law fit (red) and fractal-like kinetics fit (orange) (B).

It is probable that the TRMC decay in TiO₂ is usually fitted to the power law fit due to the good agreement between the respective observed physical phenomena. While the fractal model focuses on the recombination of trapped electrons and trapped holes,¹³⁴ the power law model considers mobile electrons, which can be trapped or react with stationary targets.¹²⁹ Like the assumptions made in the power law model, the TRMC measurement detects free charge carriers in the material, which can be trapped or show recombination with holes.^{105,164}

Nevertheless, in the present case both fit functions of the TRMC data of P25 show similar linear trends in the double logarithmic plot (cf. **Figure 5.20B**). In the fractal model, the trapped charge carriers move on the surface of the particles and can be transferred to other particles, which can be described by multiple trapping and detrapping processes. The free electrons observed in TRMC can also be trapped, but the trapped electrons already have a smaller TRMC signal in comparison to the free electrons.¹⁶³ Therefore, the TRMC method displays a higher sensitivity to charge carrier trapping reactions in comparison to TAS, where the recombination of already trapped charge carriers is observed.^{28,111} This fundamental difference in sensitivity for the observed species in the material can cause the conflicts observed during the application of the fractal fit function.

Furthermore, the suitability of the fractal kinetics fit for the analysis of transient reflectance signals in other semiconductor materials was tested. The fractal fit is applied to transient reflectance signals of tungsten oxide and zinc ferrite (**Figure 5.21**) (the TAS data of tungsten oxide under N₂, after laser excitation at 355 nm was provided by M. Sc. Christoph Haisch; Leibniz University Hannover and the zinc ferrite sample was provided by Dr. Roland Marschall; University Giessen). Both analyzing wavelengths were selected to match the highest transient reflectance signal observed in the range of 400 to 700 nm.

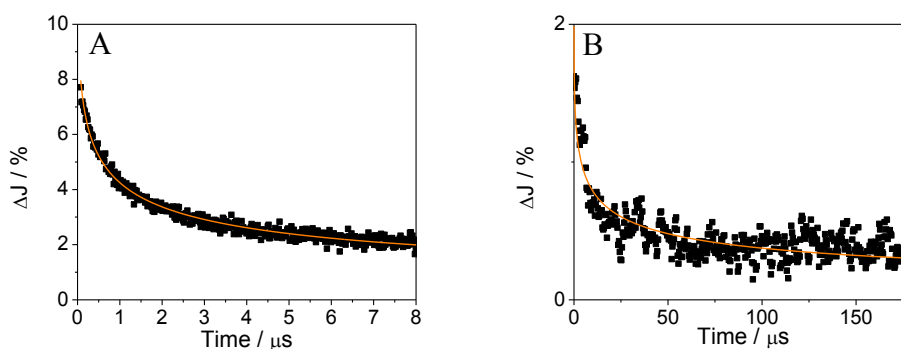


Figure 5.21: Transient reflectance signals of charge carriers photo-generated in N₂-saturated tungsten oxide (A) at 440 nm and in N₂-saturated zinc ferrite (B) at 540 nm after laser excitation with 2.6 mJ/cm² (A) and 2.4 mJ/cm² (B) ($\lambda_{ex} = 355\text{ nm}$), respectively. The experimental data is shown in black and fractal-like kinetics fit in orange.

The fractal fit of the transient reflectance signal obtained for tungsten oxide results in a fractal parameter of 0.52. All fit parameters are shown in the appendix (**Table S19**). Hence, the decay of the transient signal observed for tungsten oxide agrees with the charge carrier recombination kinetics observed for TiO₂. Complementary to the observations made for tungsten oxide, the fractal kinetics fit of the transient reflectance of zinc ferrite correlates with the results achieved for TiO₂ as well. The analysis of the decay kinetics of the transient charge carrier signal detected for zinc ferrite shows a fractal parameter of 0.55. The complete set of fitting parameters of the zinc ferrite sample is given in the appendix in **Table S20**.

It can therefore be concluded from the results observed for tungsten oxide and zinc ferrite that the fractal kinetics fit has the potential to provide a meaningful kinetic analysis of the transient reflectance signals of charge carriers in different semiconductors. The application does not seem to be limited to TiO₂. Nevertheless, only three semiconductors have been analyzed. Some semiconductor materials might show other recombination mechanisms

such as second order decay kinetics, especially if high laser intensities are employed. Despite this possibility, the fractal parameters obtained from the fractal kinetics fit could indicate a second order behavior and, therefore, demonstrate the suitability of the selected fit function.

Moreover, further evidence for the advantages of the fractal fit function in comparison to other fit functions would be the application of the fractal kinetics fit on transient reflectance or transient absorption data observed for TiO₂ found in the literature. Unfortunately, the mathematical analysis requires the data files of the measurements and no data files were available.

Although the fractal kinetics fit function displays high potential for the mathematical analysis of charge carrier recombination in TiO₂ samples, some ambiguities need to be discussed here. The fractal fit function enables mathematical analysis without the need for a baseline. Nevertheless, due to the introduction of the fractal parameter, the fractal kinetics fit requires the same number of fitting parameters as the second order fit with baseline.

The fractal kinetics fit is based on the assumption that the charge carrier recombination constant k_f gets smaller over the course of time. Therefore, the transient signal approaches zero. Nevertheless, improving the signal-to-noise ratio would, most likely, enable the observation of the transient reflectance signals in time domains longer than a couple of seconds. Nonetheless, it has not been observed whether or not that the signal indeed reaches zero. This thesis predicted that the fit process of the transient signal definitely requires no baseline. However, it remains unclear if the existing baseline is just too small to be detected.

Moreover, the physical meaning of the h -parameter is unclear. Even though Kopelman correlated the fractal parameter to the geometrical properties of certain samples (e.g., one dimensional pore systems),¹¹⁶ the physical interpretation in the case of an irregular powder sample remains questionable. It would be ideal if the experimentally obtained h -parameter could be correlated with the fractal geometry of the sample, such as by being analyzed by atomic force microscopy. The physical character of the fractal parameter has not been investigated yet. Furthermore, it is unknown whether the spatial probability distribution of the trapped charge carriers in TiO₂ (which is assumed to determine the h -parameter in this

study) can effectively be analyzed by topographic surface scanning methods. It is likely that the distribution of the trapped charge carriers in the material and the occupation of trapped states are defined by a combination of the nanostructure and the microstructure of the sample and cannot easily be detected by conventional analyses. Such assumptions about the distribution of trapped charge carriers in the material have indeed been made in the power law model and were confirmed for fractal models by Bisquert and Niklasson.^{118,130,165}

It should be mentioned here that the addition of the fractal parameter h into the second order rate law changes the second order rate constant k_2 to the fractal rate constant $k_{2,f}$ (cf. **Equation 2.11** and **Equation 4.2**). These constants are not identical and, hence, the rate constants obtained from the second order kinetics fit cannot simply be compared with the fractal rate constants. Furthermore, the previously time-independent rate constant is not constant anymore. The recombination kinetics of the trapped charge carriers in TiO₂ change over the course of time. Following the argumentation in **Chapter 5.2.3**, the segregation of the reactants results in the fact that the sum of the elementary processes cannot be represented by classical second order kinetics. At the beginning of the experiment, the recombination rate is high due to the modeled sections with initially larger charge carrier concentrations. A long period of time after the laser excitation, the recombination rate is much slower due to the sections with smaller initial concentrations of charge carriers.

Nevertheless, **Chapter 2.2.3** and the results shown in **Figure 4.14** and **Figure 4.15** indicate that the fractal rate constants can still be utilized to evaluate the charge carrier recombination. The experimental series consisting of TiO₂ with varied particle size distribution, for instance, revealed that the changes in the second order rate constants are similar to the results observed for the fractal rate constant. Unfortunately, no such comparative study could be found in the literature.

Despite the similarities observed in the application of the second order kinetics and the fractal model, the basic assumptions about the rate constant are different. In the classical second order kinetics approach the recombination kinetics of the trapped charge carriers need to be independent from the energetic distribution of states. One second order rate constant describes all recombination process unaffected by the existing uneven energetic distribution of trap states.¹³⁰ In the fractal kinetics approach, however, one parameter is not

enough to describe the recombination processes. The fractal parameter changes the fractal rate constant over the course of time. Instead of the dependence of the rate constant on the energetic distribution, the fractal parameter takes the structural variation of the recombination rate constant into account. Therefore, the fractal fit model includes the time dependency of the overall rate constant k_f caused by the overlap of multiple sections with diverging recombination rates. A similar concept for fractal kinetics being defined by the diffusion in disordered media has already been reported by Bisquert based on an energetic or spatial distribution of particles.¹⁶⁵ He also mentioned that the trapping of free charge carriers in semiconductors is defined by the energetic distribution of trap states and, subsequently, can be described by a fractal model.

In sum, the kinetic analysis of charge carrier recombination in TiO₂ employing the fractal fit function shows more benefits than disadvantages. The h parameter of 0.5 obtained for several semiconductor samples agrees well with the theoretical and experimental results reported in the literature.^{36,116,124,158} Hence, the fractal kinetics fit represents a feasible and meaningful approach for the analysis of charge carrier recombination in TiO₂ and other semiconductors.

5.3 TiO₂ samples with binary particle size distribution

In this chapter, two series of TiO₂ powders with binary particle size distribution are analyzed with the help of the fractal kinetics fit. In particular, the impact of the particle size distribution on the fitting parameters is discussed here. Additionally, the photocatalytic NO degradation of the two powder series is correlated with the charge carrier kinetics. In short, the preparation of the TiO₂ powder series was carried out by a simple two-step ultrasound procedure¹⁴⁴ and the synthesized materials consisted of small agglomerated nanoparticles deposited at the surface of larger TiO₂ particles (revealed by TEM imaging, cf. **Figure 4.12**).

5.3.1 Charge carrier kinetics

Figure 4.14 and **Figure 4.15** display the second order rate constant and the fractal rate constant, respectively, depending on the volume fraction of small particles (PC105 and PC500). The smaller scattering of the calculated rate constants and the better agreement of the fit function with the transient reflectance data (cf. **Figure 4.13**) indicate the benefits of the fractal kinetics fit.

A decrease of the rate constant for mixed TiO₂ samples with larger content of smaller particles is observed for both the second order fit function and the fractal kinetics fit (cf. **Figure 4.14** and **Figure 4.15**). However, the effect of the particle size distribution on the fractal parameter h needs to be investigated in detail and is only available through the application of the fractal fit. A change of the fractal parameter for varying particle sizes is expected, since the fractal parameter h is related to the fractal geometry of the sample.

Subsequently, the fractal kinetics fit of the transient reflectance signals at 500 nm was carried out with a free fractal parameter h and the results for the two mixed TiO₂ powder series are shown in **Figure 5.22**. All fitting parameters are given in the appendix (**Table S21** and **Table S22**).

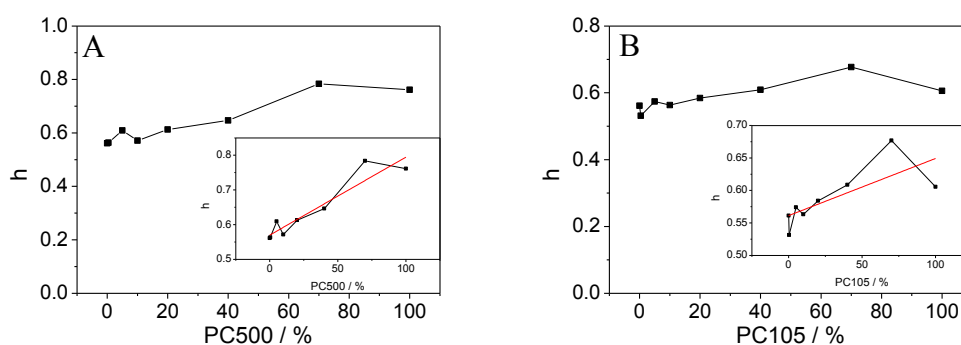


Figure 5.22: Fractal parameter h of the transient reflectance signals of charge carriers photo-generated in PC500 (A) and PC105 (B) mixed with Kronos1001 measured at 500 nm (N_2 -saturated samples, laser excitation with 1-2 mJ/pulse, $\lambda_{ex}=355$ nm). The insets show the curves with a linear fit (red).

The samples with the largest employed particle size (Kronos1001) display the smallest fractal parameter h ($h = 0.56$), while the samples containing the small particles of PC500 show a larger fractal parameter ($h = 0.76$ for the pure PC500) (cf. **Figure 5.22B**). This tendencies of samples containing smaller particles to show a higher fractal parameter were confirmed by the experimental results obtained for the series of Kronos1001 mixed with PC105 ($h = 0.62$ for pure PC105) (cf. **Figure 5.22A**). Since the fractal parameter is determined by the structure of the fractal surface, the falling trend in the fractal parameter for smaller TiO₂ particles can be explained by a change in the fractal structure of the TiO₂ surface of the powder samples.

The correlation between particle size and fractal parameter is in good agreement with the results discussed in **Chapter 5.2.4** indicating that the fractal parameter changes for

different commercial TiO₂ samples with varying particle sizes. Hence, the findings point out that the fractal parameter is indeed a parameter directly influenced by the sample properties. The insets in **Figure 5.22** show that the fractal parameter changes almost linearly with the change in the fraction of small particles. This means that mixing two TiO₂ powders with different fractal parameters leads to the arithmetic mean value for the fractal parameter of the mixture. However, the results depicted in **Figure 5.18A** indicate that the absolute h value for the non-mixed TiO₂ samples does not depend linearly on the particle size.

The effect of fractal parameter changes on the decay kinetics can be illustrated as follows: A larger exponent h leads to a faster decay of the rate coefficient k_f (**Equation 2.11**) and, subsequently, to longer charge carrier lifetimes. One possible explanation for the slower charge carrier decay for higher fractal parameters is the reduced probability of charge carrier recombination in agglomerated semiconductor particles with a high fraction of small particles. The depletion of trapped charge carriers in small particles could be one of the main driving forces leading to the segregation of the charge carriers. The model of a fractal surface (**Chapter 5.2.3**) proved that segregation induces long charge carrier lifetimes diverging from second order kinetics. Accordingly, a higher fraction of small particles causes a larger segregation, which in sum results in a larger exponent h correlating with a longer charge carrier lifetime.

A longer charge carrier lifetime for TiO₂ particles with smaller particle size was detected by Serpone *et al.* in 1995 for colloidal TiO₂ suspensions with primary particle sizes between 2 and 27 nm.²² However, they related the complex decay kinetics of the transient absorption signals to the sequential overlap and combination of different trapped charge carrier species. Subsequently, no correlation with photocatalytic efficiencies was carried out in their study.

The observed increase in the charge carrier lifetimes for a rising fraction of small particles in a sample can be related to two possible effects. First, a drop in the fractal parameter, caused by the change in the fractal surface with changing particle size distribution, can explain the reduced charge carrier recombination rate. Second, a reduction of the charge carrier rate constant $k_{2,f}$ (cf. **Equation 4.2**), due to a change of the charge carrier recombination mechanism in the different samples, can also cause the observed longer charge carrier lifetimes.

Discrimination between the two effects aforementioned is not simple. However, the fractal fit function enables the investigation of the transient reflectance signals of the mixed TiO₂ samples in two different ways. The first option is for the fitting process to be carried out with free variation of the h parameter. This leads to an optimum h value, as shown for each TiO₂ mixture in **Table S21** and **Table S22**. Another option is to select a constant parameter h for the analysis of the TiO₂ powder samples. For example, samples containing a large amount of PC105 or PC500 particles show the best fit at $h = 0.6-0.7$. Hence, a fractal parameter of 0.65 was selected for the kinetic analysis. **Table 5.4** illustrates the changes in the fractal rate constant $k_{2,f}$.

Table 5.4: Fractal rate constant $k_{2,f}$ of the fractal kinetics fit of the transient reflectance signals of charge carriers photo-generated in Kronos1001 mixed with PC105 or PC500 measured at 500 nm with $h = 0.65$.

PC105/PC500 content / wt.%	$k_{2,f} / 10^4 \text{ mol} \cdot \text{L}^{-1} \text{ s}^{-1}$ of PC105	$k_{2,f} / 10^4 \text{ mol} \cdot \text{L}^{-1} \text{ s}^{-1}$ of PC500
20	0.22	0.22
40	0.19	0.25
70	0.14	0.13
100	0.11	0.15

In the case of a fixed fractal parameter h , the fractal rate constants of both series of mixed TiO₂ samples show a decreasing trend. It appears that the mathematical analysis of the transient reflectance signals observed for TiO₂ by means of the fractal fit function does not discriminate between changes induced by different fractal surfaces or different charge carrier recombination mechanisms. For the observed trend of longer charge carrier lifetimes for samples containing a larger fraction of small particles, a fixed fractal parameter leads to a drop in the fractal rate constant and vice versa.

Unfortunately, the strategies of the fractal kinetics fit discussed in this paper do not allow for discrimination between pure changes in the fractal geometry and changes in the charge carrier recombination mechanism. It is likely that these two effects are intrinsically tied to each other.

The \bar{R}^2 values of the samples should be discussed here, since the samples containing large amounts of PC500 show smaller \bar{R}^2 values compared to the samples containing the same amount of PC105 (**Table S21** and **Table S22**). This smaller coefficient of determination

obtained for the samples containing PC500 was related to the 2.5 times smaller signal intensity of pure PC500 in comparison to PC105 (cf. **Figure 4.2**). The smaller S/N ratio causes the worse correlation between the fit function and the experimental data points.

Furthermore, it is possible and highly probable that more sample properties, such as the crystallinity, interfere with the charge carrier recombination speed and mechanism. Subsequently, these properties might change the observed fractal parameter and the fractal reaction constant. Therefore, a complete analysis of and assignment between the sample properties and the fractal fit parameters can hardly be achieved in this work. Nevertheless, the correlation of the available physical and photocatalytic properties with the fractal fit parameters are discussed in detail in the following chapter (**Chapter 5.3.2**).

Overall, the results of the fractal fit function applied to the two series of mixed TiO₂ (**Table S21** and **Table S22**) reveal that for all measured samples the average h value is between 0.56 and 0.76. These results correlate well with the asymptotic $t^{-1/2}$ dependence described in the literature.³⁶ Moreover, since the experiments with the two TiO₂ powder series were carried out under considerably low laser intensities of 1-2 mJ/cm², the requirements for the model of Shuttle *et al.* are also nearly fulfilled. Hence, a fractal parameter of 0.5 is expected to be the limiting case at long times and at low laser intensities.¹²⁹

5.3.2 Photocatalytic NO degradation

Aside from the effect of the binary particle size distribution on the charge carrier kinetics, the interplay of the particle size and the photocatalytic NO degradation is discussed here.

Antenna mechanism

A clear correlation between particle size and photocatalytic activity has not yet been achieved. Zhang *et al.*, for instance, reported that the sample with the medium particle size of 21 nm displayed the highest photonic efficiency for the photocatalytic chloroform degradation performed in TiO₂ suspensions.¹⁶⁶ Despite these findings, Gao and Zhang observed the highest photocatalytic degradation of phenol for the smallest TiO₂ particles with 7 nm particle size.¹⁶⁷ Other studies have shown that the effect of the crystallinity on the photocatalytic performance of TiO₂ powders is significant and can distort expected correlations between particle size and photocatalytic activity.^{58,168}

The results obtained in this study indicate rather small changes in the photocatalytic activity, despite the huge changes in the BET-surface area. This needs to be explained before further correlations can be made. As mentioned in **Chapter 4.2.4** the formation of agglomerates bound together by capillary attraction reduces the available surface area. However, the resulting photonic efficiencies (cf. **Figure 4.16**) can only be explained in combination with a charge transfer mechanism from the center of the agglomerates to the outer surface.

The differently sized TiO₂ nanoparticles in the mixed TiO₂ powder samples are in intimate contact, presumably enabling the transfer of charge carriers between the particles. This beneficial charge transfer between TiO₂ particles was already described by Wang *et al.* in 2006 (cf. **Figure 5.8**).¹⁵⁵ According to the antenna mechanism, the photo-generated charge carriers can be transferred along the network of agglomerated particles. This makes the degradation of adsorbed compounds locally independent from the position of the adsorption of photons.

The experiments carried in this study do not employ TiO₂ suspensions. TiO₂ powder samples in contact with air (50 % rel. humidity) were used. It appears that the charge transfer does not require the formation of TiO₂ networks in suspension. The formation of agglomerates, in which surface adsorbed water surrounds the primary particles, seems to be sufficient for a charge transfer between the TiO₂ particles.

Previous studies have shown that the TiO₂ surface under both wet and dry conditions is defined by terminal OH groups.¹⁶⁹ The dissociative adsorption of water molecules forms these surface sites. Moreover, especially on the predominant anatase (101) surface, a large fraction of undissociated water molecules are found.¹⁷⁰ These structured water layers can only be removed by prolonged heating.¹⁶⁹ In addition, the photo induced superhydrophilicity of TiO₂, which is based on the interaction of the photo-generated charge carriers on the TiO₂ surface with adsorbed water molecules, is observed similarly in TiO₂ suspensions and on TiO₂ powder surfaces.^{171–173}

Consequently, the structure of the interface between two TiO₂ agglomerates and the respective charge transfer processes are expected to be comparable for TiO₂ suspensions and powder samples. **Figure 5.23** shows the assumed charge transfer in spherical TiO₂ agglomerates schematically.

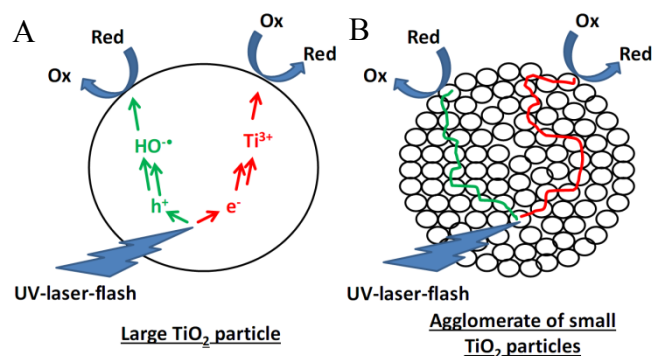


Figure 5.23: Charge transfer to adsorbed molecules in large TiO_2 particles (A) and synergetic charge transfer in TiO_2 agglomerates (B) following the antenna mechanism. Reprinted from Ref. 48.

It was therefore concluded that the charge carriers are trapped close to the particle surface and can be transferred between the surfaces of the different particles. Subsequently, the probability distribution of the trapped charge carriers in the agglomerated clusters of TiO_2 represents a complex fractal. Consequently, the fractal kinetics fit function was applied to the charge carrier signals of the mixed TiO_2 samples.

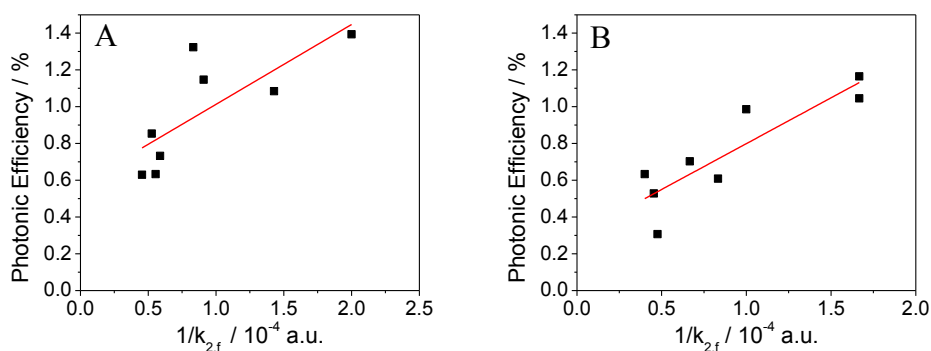


Figure 5.24: Photonic efficiencies of NO degradation plotted against the inverse fractal rate constants $k_{2,f}$ of the fractal kinetics fit of the transient reflectance signals of charge carriers photo-generated in the synthesized TiO_2 materials containing PC500 (A) and PC105 (B) mixed with Kronos1001 measured at 500 nm with $h = 0.5$ in the time domain 6-200 μs . The experimental data is given in black and linear fit function is shown in red. Reprinted from Ref. 48.

Moreover, the photocatalytic activity in terms of NO degradation was investigated. **Figure 5.24** compares the obtained results directly with the inverse fractal rate constant. The results in **Figure 5.24** confirm the assumption made in **Chapter 2.1.2** that a longer charge carrier lifetime correlates with a higher degree of photocatalytic activity. In the present work, the samples possessing a higher NO degradation reveal a longer transient reflectance signal as well. The charge carrier lifetime was simplified by the inverse fractal rate

constant. The real charge carrier half-life could have only been calculated for a pure second order reaction according to $t_{1/2} = \frac{1}{Ak_2}$. However, the inverse fractal rate constant can be used in the same manner to describe the lifetime of the charge carrier signal quantitatively.

The observed faster recombination kinetics of trapped charge carriers in large TiO_2 particles are identified in the complete nanosecond to microsecond time-scale. **Figure 5.25** illustrates the charge carrier recombination speed for the larger TiO_2 particles and for the TiO_2 agglomerates formed from small primary particles and its correlation with the photocatalytic degradation of NO.

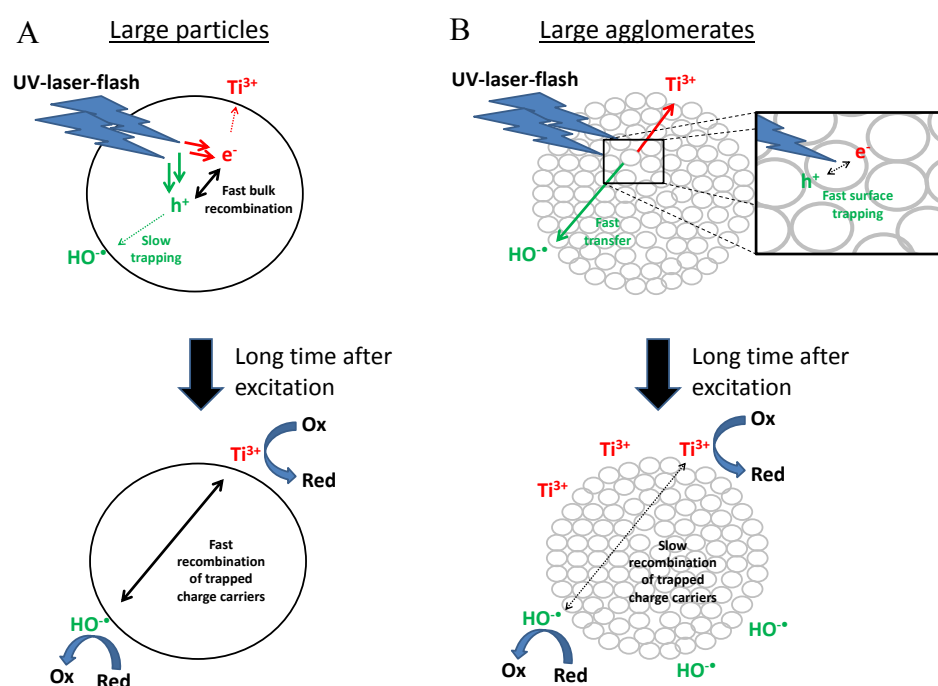


Figure 5.25: Correlation of charge carrier lifetime and photocatalytic degradation of adsorbed nitric oxide for large TiO_2 particles (A) and large TiO_2 agglomerates (B). Adapted from Ref. 48.

It appears that the beneficial charge transfer between small and large TiO_2 particles in TiO_2 agglomerates explains the observed NO degradation efficiency of the powder samples. Since the charge carrier transfer between the particles supports the charge carrier separation, an enhanced photocatalytic activity of the samples with binary particle size distribution is obtained. **Figure 5.25** shows the resulting dependency between the photocatalytic activity and the charge carrier lifetime. The correlation between the inverse fractal rate constant and photocatalytic NO degradation is observed for both series of

mixed TiO₂ powders. In short, the samples containing many small particles exhibit long charge carrier lifetimes and higher photonic efficiencies.²⁷

The faster charge carrier recombination kinetics in large TiO₂ particles (cf. **Figure 4.15**) can be explained by the predominant fast bulk recombination of the charge carriers. Subsequently, for both experimental mixed TiO₂ series a drop in the fractal rate constant to 25-50 % is observed, if the fractal rate constant obtained for the smallest particles is compared with the fractal rate constant of the largest particles (cf. **Figure 4.15**). At the same time, these samples show twice the photonic efficiency in the NO degradation experiments (cf. **Figure 4.16**).

The results clearly indicate a correlation between charge carrier lifetime and photocatalytic activity. This interplay between the charge carrier kinetics and the photocatalytic performance of a semiconductor materials has been predicated by theoretical calculations.²⁷ However, the correlation between these two quantities is not always observed in experiments, since the photocatalytic reaction is a complex multi-step process consisting of adsorption, desorption and charge transfer reactions. Hence, the simple correlation between charge carrier lifetime and photocatalytic activity is often hidden by side reactions.

A complete picture of the photocatalytic processes on the particle surface can only be obtained if the active surface areas are considered. As mentioned in **Chapter 4.2.4**, the active surface area can be estimated using different experimental set-ups. Unfortunately, the BET surface area did not show any correlation with the obtained results of the photocatalytic NO degradation. This is related to the unrealistic dry conditions during the BET measurement. Under standard conditions, the small TiO₂ particles form large agglomerated structures bound together by capillary forces. During the BET measurement the surface adsorbed water is removed and huge respective surface areas are obtained (cf. **Figure 4.17**). Under the experimental conditions of the photocatalytic experiment, on the other hand, most of this surface area is occupied by water molecules and not available for the degradation of NO.

Consequently, the detection of the adsorbed amount of NO represents a better method to justify the active surface area of the powder samples (cf. **Figure 4.18**). **Figure 4.18** illustrates a change in the active surface area by a factor of 1.5-2 for the TiO₂ powder

samples with binary particle size. Moreover, for the mixed TiO₂ series containing PC105 only a very small variation in the active surface area was observed. This was particularly true when the values obtained for the pure KronoClean7050 and the pure PC105 sample were compared. Therefore, the reported effects of the particle size distribution on the photocatalytic NO degradation are mainly related to the charge carrier recombination kinetics.

Nonetheless, Boujday *et al.* explained the photocatalytic process by a simple model composed of two subdivisions, namely the photo part (charge carrier generation and kinetics) and the catalysis part (surface radical formation).¹⁷⁴ Hence, the effect of the surface area on the photocatalytic process should not be underestimated. Indeed, particularly for the samples containing PC500 the combination of both surface area and charge carrier kinetics explains the effects observed upon mixing PC500 with Kronos1001.

5.4 TiO₂ samples mixed with additives

In contrast to the previous samples consisting of solely TiO₂, the samples discussed here were prepared by grinding TiO₂ with a single additive. These additives were selected as model compounds for building materials. Similar to the pure TiO₂ samples, the charge carrier recombination kinetics are analyzed and discussed here. Photocatalytic NO degradation experiments were carried out with these powder samples as well. The respective observations and potential relationships are then analyzed. The discussion of the results is divided into sections according to the additives employed.

5.4.1 Influence of BaSO₄

The photonic efficiencies of the TiO₂-BaSO₄ samples with varying content of photocatalyst were calculated according to **Equation 3.4** and the results are shown in **Figure 5.26**. Additionally, the expected correlation between photonic efficiency and the volume fraction of TiO₂ is indicated by a red line.

The red line in **Figure 5.26** is based on the assumption that the available photocatalytic surface area is a linear function of the TiO₂ content. This assumption represents the expected effect for the dilution of the photocatalyst. In fact, it is a rather obvious expectation that the substitution of 50 % of the active TiO₂ surface area with photocatalytically inactive BaSO₄ particles reduces the photocatalytic activity by a factor

of 2. Such a linear dependency on the volume fraction of TiO_2 has been observed between the active surface area, determined by the NO adsorption (cf. **Figure 4.22**).

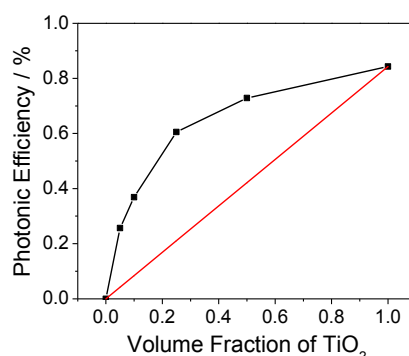


Figure 5.26: Photonic efficiencies of TiO_2 - BaSO_4 powder mixtures calculated from the photocatalytic NO degradation. The red line shows the expected dependency between the photonic efficiency and the amount of TiO_2 . Adapted from Ref. 135. The photonic efficiency of TiO_2 - BaSO_4 without the expected linear correlation has been shown in **Figure 4.21**.

However, the powder samples consist of TiO_2 nanoparticles and the variation of the fraction of particulate additive displays higher photocatalytic activities than expected by this simple approach. To explain the observed behavior, the optical properties of the sample need to be taken into account.

Indeed, the photocatalytic activity of the mixed TiO_2 - BaSO_4 samples can be explained by the combination of UV-light absorption and charge carrier concentrations of the mixed samples observed in this study. Every sample which displayed relatively high photonic efficiencies revealed high UV-light absorptions as well (cf. **Figure 4.21A**). Hence, the apparent quantum yields shown in **Figure 4.21B**, which represent the normalization of the photocatalytic activity to the amount of absorbed light, indicate a rather linear trend for all of the mixed TiO_2 - BaSO_4 samples. An identical amount of absorbed photons cause the same photonic efficiency in these samples. A chemical effect of BaSO_4 would lead to a deviation from this consistent trend. In short, this solely optical effect of BaSO_4 on the photocatalytic process is supported by the constant quantum yields of the respective TiO_2 - BaSO_4 samples. The main question is: What did cause the high UV-light absorption in the mixed samples? Subsequently, the strong scattering of UV light by BaSO_4 particles was identified as the reason for the improved UV-light absorption. **Figure 5.27** illustrates the light scattering in the pure TiO_2 and in the mixed TiO_2 - BaSO_4 samples schematically.

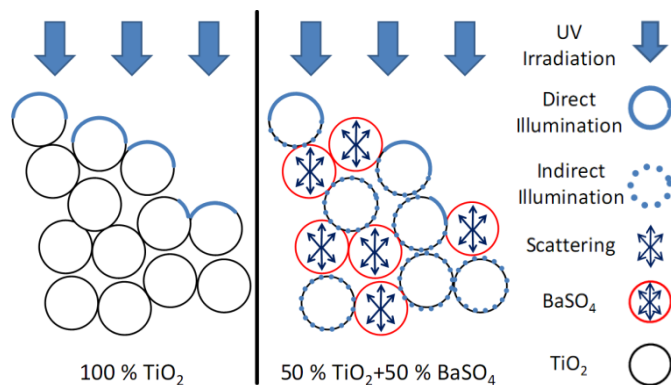


Figure 5.27: Scheme representing the scattering of the UV-light in TiO_2 - BaSO_4 samples. The scattering results in an improved absorption of light in mixtures with a low content of photocatalyst. Reprinted from Ref. 135.

The BaSO_4 particles inside the TiO_2 - BaSO_4 powder samples scatter the UV-light strongly. Hence, the penetration depth of the UV-light increases with a larger content of BaSO_4 and previously dark inactive TiO_2 surface areas are now participating in the photocatalytic reaction.

To justify the assumptions made here, the charge carrier concentrations in the mixed TiO_2 - BaSO_4 samples were analyzed. For instance, that equal charge carrier recombination kinetics in the mixed samples is in agreement with the presumptions stated above. The fractal kinetics fit is employed for the analysis of the charge carrier recombination kinetics of the respective samples.

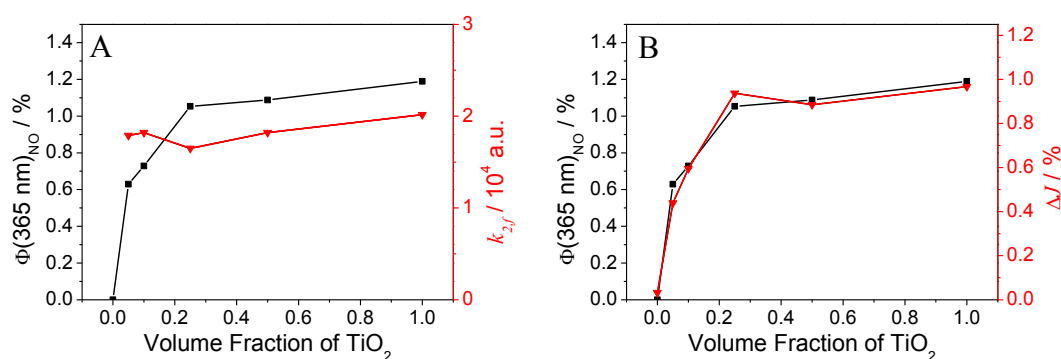


Figure 5.28: Apparent quantum yield $\Phi(365 \text{ nm})$ obtained from the photocatalytic NO degradation and fractal rate constant $k_{2,f}$ taken from the normalized transient reflectance signals of charge carriers photo-generated in TiO_2 - BaSO_4 measured at 500 nm after laser excitation (N_2 -saturated samples, $h = 0.5$, laser excitation with 2 mJ/pulse, $\lambda_{ex} = 355 \text{ nm}$) (A) and apparent quantum yield obtained from the photocatalytic NO degradation and height of the transient reflectance signals of charge carriers photo-generated in TiO_2 - BaSO_4 measured at 500 nm 5-10 μs after the excitation (B). Reprinted from Ref. 135.

Figure 5.28 shows the obtained fractal rate constant of the fractal kinetics fit of the transient signals observed for TiO₂-BaSO₄ powder samples. Clearly, the fractal rate constant of the decay of the transient charge carrier signals in TiO₂-BaSO₄ remains constant for all volume fractions of TiO₂ employed in this study. Consequently, the observed charge carrier recombination speed and the respective charge carrier lifetime do not change upon variation of the BaSO₄ content. These results prove that the addition of BaSO₄ to TiO₂ does not interfere with the charge carrier recombination kinetics.

Furthermore, a linear correlation between the amount of trapped charge carriers in the material and the quantum yield would correlate with the previous assumptions about the inert character of the BaSO₄ as well. Hence, deeper insight into observed photocatalytic reactions were obtained by the correlation of the apparent quantum yields and the height of the transient reflectance signals in the TiO₂-BaSO₄ samples shown in **Figure 5.28B**. An excellent correlation between the height of the transient signal and the quantum yield taken from the photocatalytic NO degradation is observed. This linear correlation between the two quantities is illustrated in detail in **Figure 5.29A**. The height of the transient signal represents the amount of generated charge carriers in the material. Hence, the excellent agreement between the photocatalytic performance illustrated by the apparent quantum yields and the charge carrier concentration is further evidence for the proposed mechanism presented above (**Figure 5.27**). It is apparent that the concentration of charge carriers in the TiO₂-BaSO₄ samples is a direct indicator for their ability to degrade NO during the photocatalytic experiments.

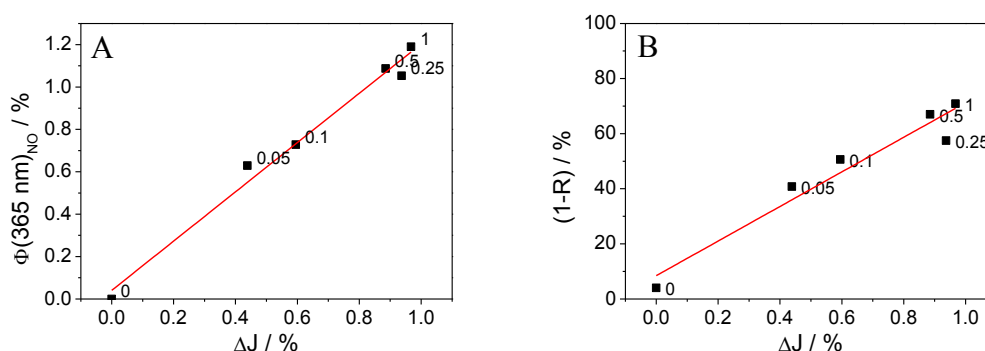


Figure 5.29: Apparent quantum yield $\Phi(365 \text{ nm})_{\text{NO}}$ obtained from the photocatalytic NO degradation (A) and absorption at 365 nm (1-R) (B) of TiO₂-BaSO₄ as a function of the transient reflectance signals of charge carriers photo-generated in TiO₂-BaSO₄ measured at 500 nm 5-10 μs after the excitation with linear fit (red). The labels of the data points indicate the volume fraction of TiO₂. Adapted from Ref. 135.

Figure 5.29B shows that the concentration of the charge carriers in the respective $\text{TiO}_2\text{-BaSO}_4$ samples is connected to the absorption of UV-light at 365 nm. Interestingly, the samples containing 25-100 % TiO_2 show similar UV-light absorption, photocatalytic NO degradation, and charge carrier concentration. Only the samples with 5 and 10 % TiO_2 reveal lower quantum yields and lower corresponding charge carrier signals.

As a consequence of this non-linear dependency between photocatalytic activity and TiO_2 content, it is questionable whether high loadings of photocatalyst are required to achieve excellent photocatalytic performances. Obviously, smaller amounts of photocatalyst can lead to the same photocatalytic activity as when the pure photocatalyst is used. The main objective is that high UV-light absorption needs to be maintained. Overall, the chemically inert character of BaSO_4 as an additive for TiO_2 was confirmed in this work. Nevertheless, the optical properties of the sample can be improved by UV-light scattering. This scattering generates a high UV-light absorption of the mixed TiO_2 samples, which reduces the required quantity of photocatalyst for a given photocatalytic degradation of NO.

5.4.2 Influence of carbonates

Similar to the study on TiO_2 ground with BaSO_4 , the effects of the additives Na_2CO_3 and CaCO_3 on the optical and photocatalytic properties of the mixed TiO_2 powder samples are discussed here. The correlation between the apparent quantum yield and the height of the transient reflectance signals of the mixed TiO_2 -additive samples is illustrated in **Figure 5.30**.

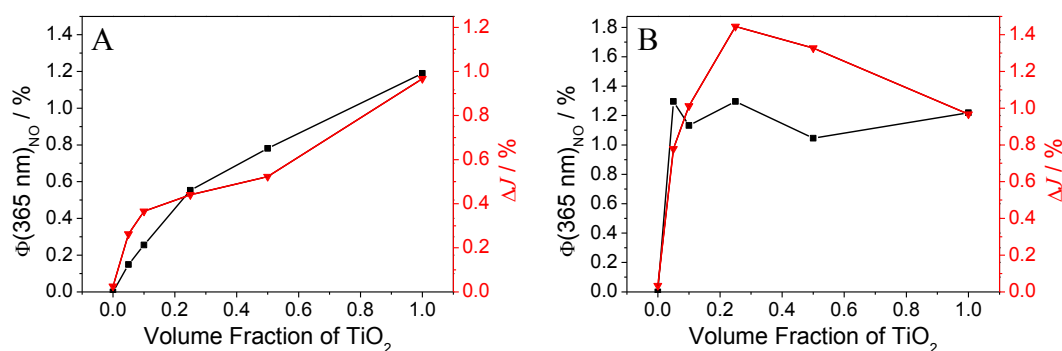


Figure 5.30: Apparent quantum yield $\Phi(365 \text{ nm})$ obtained from the photocatalytic NO degradation and height of the transient reflectance signals of charge carriers photo-generated in $\text{TiO}_2\text{-Na}_2\text{CO}_3$ (A) and in $\text{TiO}_2\text{-CaCO}_3$ (B) powder mixtures measured at 500 nm 5-10 μs after the laser excitation (N_2 -saturated samples, laser excitation with 2 mJ/pulse, $\lambda_{\text{ex}}=355 \text{ nm}$). Reprinted from Ref. 135.

Figure 5.30A shows that the same trends upon variation of the TiO_2 content were observed for the transient signal height and the quantum yield obtained for the $\text{TiO}_2\text{-Na}_2\text{CO}_3$ samples. Both parameters decrease for smaller volume fractions of TiO_2 . On the other hand, all respective $\text{TiO}_2\text{-CaCO}_3$ samples which contain the same amount of photocatalyst show higher quantum yields and higher transient reflectance signals in contrast to the $\text{TiO}_2\text{-Na}_2\text{CO}_3$ samples. Moreover, the mixed $\text{TiO}_2\text{-CaCO}_3$ samples with 25 % and 50 % TiO_2 displayed the largest transient reflectance signals and very high quantum yields as well.

Interestingly, the optical properties of all powder samples were quite similar (cf. **Figure 4.25**). However, the addition of the two carbonates revealed different trends for the photocatalytic performance of the respective TiO_2 samples. While the addition of Na_2CO_3 to TiO_2 reduced the photocatalytic NO degradation (**Figure 5.32A**), the samples containing CaCO_3 maintained considerably high photocatalytic activities even at very small loadings of TiO_2 (**Figure 5.32B**). Moreover, the active surface areas of the $\text{TiO}_2\text{-Na}_2\text{CO}_3$ and $\text{TiO}_2\text{-CaCO}_3$ samples, determined by the amount of adsorbed NO, displayed opposing trends as well (cf. **Figure 4.26**). While the addition of CaCO_3 caused a linear dependency between active surface area and TiO_2 content, the $\text{TiO}_2\text{-Na}_2\text{CO}_3$ samples showed very small and constant active surface areas.

Subsequently, the results do not equate to the observations made for $\text{TiO}_2\text{-BaSO}_4$. This discrepancy could be explained by the variation of charge carrier concentration (cf. **Figure 4.23**) and charge carrier recombination mechanism caused by the addition of the respective carbonates.

An example for this variation is that a chemical effect of CaCO_3 on the photocatalytic performance is expected, since very high charge carrier concentrations are detected for the respective samples in comparison to $\text{TiO}_2\text{-BaSO}_4$ and $\text{TiO}_2\text{-Na}_2\text{CO}_3$. The samples containing Na_2CO_3 , on the other hand, displayed smaller charge carrier concentrations in comparison to samples consisting of TiO_2 mixed with CaCO_3 or BaSO_4 , respectively. Similar to the $\text{TiO}_2\text{-CaCO}_3$ samples, a physical or chemical effect might be the reason for the diminished charge carrier concentrations observed for $\text{TiO}_2\text{-Na}_2\text{CO}_3$.

The first step in identifying chemical effects of carbonates on the photo induced processes in TiO_2 was the detailed investigation of the correlation between the charge carrier concentrations and the apparent quantum yields (**Figure 5.31**).

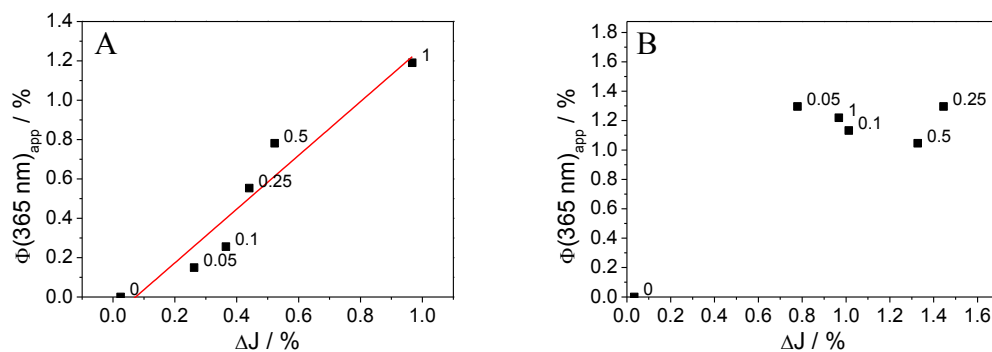


Figure 5.31: Apparent quantum yield $\Phi(365 \text{ nm})$ obtained from the photocatalytic NO degradation as a function of the height of the transient reflectance signals of charge carriers photo-generated in $\text{TiO}_2\text{-Na}_2\text{CO}_3$ (the red line represents a linear fit) (A) and the $\text{TiO}_2\text{-CaCO}_3$ (B) powder mixtures measured at 500 nm 5-10 μs after the laser excitation (N_2 -saturated samples, laser excitation with 2 mJ/pulse, $\lambda_{\text{ex}}=355 \text{ nm}$). The labels of the data points indicate the volume fraction of TiO_2 . Reprinted from Ref. 135.

Figure 5.31A reveals a linear correlation between the quantum yields of the $\text{TiO}_2\text{-Na}_2\text{CO}_3$ samples and the respective charge carrier concentrations. Hence, the same amount of charge carriers in the material leads to the same photocatalytic performance. The correlation between the transient signal height and the quantum yield of the carbonate-containing samples agree with the previously discussed correlation of these quantities observed for the $\text{TiO}_2\text{-BaSO}_4$ samples. This is strong evidence for the general connection of charge carrier concentration and photocatalytic activity observed for TiO_2 powder samples.

Subsequently, a lower charge carrier concentration, probably due to faster recombination of the charge carriers, was identified as the reason for the observed small photocatalytic activities of TiO_2 in the presence of Na_2CO_3 . This theory is supported by the results shown in **Figure 5.32**, which indicates the correlation between the apparent quantum yields and the fractal rate constant.

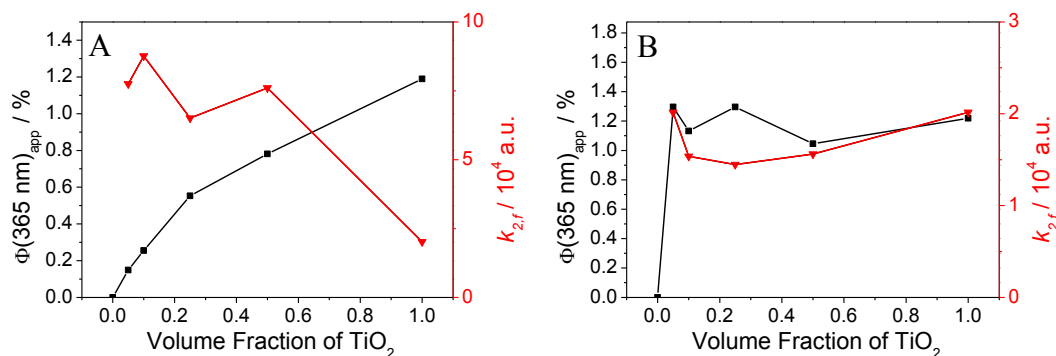


Figure 5.32: Apparent quantum yield $\Phi(365 \text{ nm})$ obtained from the photocatalytic NO degradation and fractal rate constant $k_{2,f}$ taken from the transient reflectance signals of charge carriers photo-generated in TiO₂-Na₂CO₃ (A) and TiO₂-CaCO₃ (B) measured at 500 nm after laser excitation as a function of the volume fraction of TiO₂ (N₂-saturated samples, $h = 0.5$, laser excitation with 2 mJ/pulse, $\lambda_{ex}=355 \text{ nm}$). No meaningful kinetic analysis could be carried out for the transient reflectance signals of the two samples not containing any TiO₂. Reprinted from Ref. 135.

Figure 5.32A reveals a much higher fractal rate constant for the samples containing Na₂CO₃ mixed with TiO₂. The fractal rate constant $k_{2,f}$ increases from $2 \cdot 10^4 \text{ a.u.}$ for pure TiO₂ to $9 \cdot 10^4 \text{ a.u.}$ for the sample containing 90 % Na₂CO₃. The corresponding factor of 4 between the fractal rate constants is similarly observed for the ratio of the quantum yield of these samples, which drops from 1.19 % to 0.26 %. Therefore, the results prove that a faster charge carrier recombination is the reason for the lower photocatalytic activities observed for TiO₂-Na₂CO₃.

The higher recombination rate of the photo-generated charge carriers in the presence of Na₂CO₃ might be explained by a new recombination mechanism provided by sodium ions. In fact, it has been reported that sodium ions can act as recombination centers in TiO₂ photocatalysts.¹⁷⁵ Nonetheless, at room temperature the intercalation of sodium ions into TiO₂ is considered to be highly unlikely, despite the fact that some researchers assume that the intercalation of ions is possible at relatively low temperatures as well.¹⁷⁶

Subsequently, the effects of Na₂CO₃ observed in this study are explained by a change in the reduction potential of the trapped electrons in the presence of sodium cations. Such effects of cations have been detected by Chamousis and Osterloh for the H₂-production reaction employing TiO₂ and by Meyer *et al.* for the reduction of organic mediators in TiO₂-based dye-sensitized solar cells (DSSCs).¹⁷⁷⁻¹⁷⁹ The authors reported that Li⁺, Na⁺ and K⁺ ions at the TiO₂ surface cause a higher reduction potential of the trapped electrons

in comparison to Ca^{2+} , Mg^{2+} and Sr^{2+} ions. It was found, indeed, that the charge density of the metal ions determine the reduction potential.^{51,180} Hence, the driving force of the charge carrier recombination of trapped electrons with trapped holes is larger for samples containing Li^+ , Na^+ or K^+ .

This influence of the ions present on the TiO_2 surface on the charge carrier lifetimes was detected by Wang and Peter in 2012 in a study employing DSSCs.¹⁸¹ The results of the photocatalytic experiments carried out in the present work can easily be transferred to the observations made for DSSCs, since both systems are very similar and employ redox active species on the semiconductor surface. Therefore, in both cases the change of the CB potential interferes with the whole charge transfer kinetics. Consequently, the higher reduction potentials of the trapped electrons in the presence of sodium ions explain the larger recombination rate constants observed for the samples containing NaCO_3 in comparison with the samples made by mixing of TiO_2 with CaCO_3 or BaSO_4 .

In contrast to the results discussed for $\text{TiO}_2\text{-Na}_2\text{CO}_3$, a diverging trend was observed for the addition of CaCO_3 to TiO_2 (cf. **Figure 5.32B** and **Figure 5.31B**). The $\text{TiO}_2\text{-CaCO}_3$ samples display much higher photocatalytic activities in comparison to the utilization of Na_2CO_3 . This correlates well with the above-described effect of the cations on the reduction potential of the trapped electrons. In the case of the Ca^{2+} ions, the driving force for the recombination is lower in comparison to samples including the presence of sodium ions.^{51,180} Nevertheless, the slower charge carrier recombination does not explain the beneficial effects observed upon mixing of TiO_2 and CaCO_3 in comparison to $\text{TiO}_2\text{-BaSO}_4$. Therefore, the results in **Figure 4.23B**, **Figure 5.32B**, and **Figure 5.31B** need to be investigated in detail to assess the beneficial properties of the $\text{TiO}_2\text{-CaCO}_3$ samples.

Interestingly, **Figure 4.23B** shows that the charge carrier concentrations for the samples containing 25-50 % CaCO_3 are larger than the charge carrier concentration of the pure TiO_2 sample. Moreover, **Figure 5.32B** displays a small change in the charge carrier recombination kinetics in these samples. The sample showing the highest charge carrier concentration possesses the smallest fractal rate constant. However, the change in the fractal rate constant is considerably small. Therefore, the main effect of the addition of CaCO_3 to TiO_2 is the increase of the charge carrier concentration. Overall, the results indicate a stabilization of the charge carriers on the surface of the semiconductor. **Figure**

5.33 illustrates two potential stabilization mechanisms of trapped charge carriers on the surface of TiO_2 in the presence of CaCO_3 .

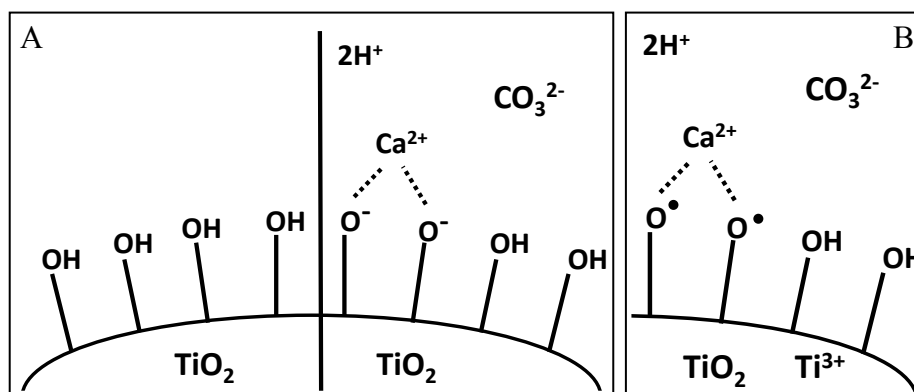


Figure 5.33: Deprotonation of the TiO_2 surface hydroxyl groups (A) and stabilized trapped charge carriers (Ti^{3+} centers and surface O^\bullet radicals) (B) by CaCO_3 . Adapted from Ref. 135.

The first stabilizing effect shown in **Figure 5.33A** is the deprotonation of the surface hydroxyl groups by alkaline additives such as carbonates. Indeed, the negatively charged surface of TiO_2 generated by the alkaline media increases the lifetime of the trapped charge carriers. Jing *et al.* reported in 2012 that the charged surface of TiO_2 , formed either by a high pH or by the adsorption of charged ions, results in an increase of charge carrier lifetime due to electrostatic interactions.¹⁵³

According to the above-mentioned findings, both CaCO_3 and Na_2CO_3 are expected to similarly reduce the charge carrier recombination in TiO_2 . However, it was shown here that the presence of Na_2CO_3 causes a higher charge carrier recombination rate due to an increase in the potential of the trapped electrons.

The faster recombination kinetics of TiO_2 - Na_2CO_3 can further be explained by the different solubilities of Na_2CO_3 and CaCO_3 . The solubility product of sodium carbonate in water is significantly higher than the solubility product of calcium carbonate in water (CaCO_3 at room temperature: $K_{sp} = 1.0 \cdot 10^{-8} \frac{\text{mol}^2}{\text{L}^2}$;¹⁸² Na_2CO_3 at room temperature: $K_{sp} = 0.16 \frac{\text{mol}^3}{\text{L}^3}$ ¹⁸³). The different solubilities cause a varying concentration of ions on the surface of TiO_2 . Subsequently, the large concentration of sodium and carbonate ions in the case of TiO_2 - Na_2CO_3 can lead to negative secondary effects, such as the blocking of active sites or the acceleration of the charge carrier recombination (as shown earlier in this section).

Therefore, the large concentration of ions at the surface of $\text{TiO}_2\text{-Na}_2\text{CO}_3$ in comparison to $\text{TiO}_2\text{-CaCO}_3$ reduces the obtained photocatalytic NO degradation.

The second stabilizing effect of charge carriers on the TiO_2 surface is shown in **Figure 5.33B**. The illustration displays the interaction between the trapped holes or electrons and ions present at or close to the surface of TiO_2 . The trapped charge carriers are localized and thus can be further stabilized by cations or anions at the surface of the semiconductor particle. The Ca^{2+} ions, for instance, coordinate the deprotonated hydroxyl groups, which serve as traps for the photo-generated holes in the photocatalytic process. The coordination of two deprotonated hydroxyl groups by Ca^{2+} ions increases the stabilizing effect in comparison to the coordination of only one group by sodium ions. Subsequently, in contrast to sodium ions, Ca^{2+} ions reduce the charge carrier recombination in TiO_2 to a higher extent, as shown previously in **Figure 5.32A**.

In general, the results obtained for the TiO_2 powder samples mixed with carbonates revealed different stabilization mechanisms for the trapped charge carriers by the two cations (calcium and sodium). The beneficial stabilization of trapped charge carriers by Ca^{2+} ions causes the observed higher photocatalytic performances of $\text{TiO}_2\text{-CaCO}_3$ samples. Overall, the analysis of the charge carrier recombination turned out to be a key element for the understanding of the photocatalytic process on TiO_2 surfaces.

Similar to the TiO_2 samples with binary particle size distribution discussed in **Chapter 5.3.2**, the TiO_2 -additive samples which revealed a high photocatalytic NO degradation displayed a large amount of adsorbed NO on the surface. Therefore, not solely the charge carrier kinetics defines the photocatalytic activity of the studied samples. Both subdivisions of photocatalysis (charge carrier generation/kinetics and surface radical formation) influence the photocatalytic process.

5.5 TiO_2 paints

The photocatalytic activity of the TiO_2 paints (cf. **Table 4.4**) was relatively small in comparison to the photocatalytic activity of pure TiO_2 powder surfaces (cf. **Figure 4.16**). The reason for this difference is the small fraction of photocatalyst present in the TiO_2 paint matrix. The photocatalytic activity of the TiO_2 paints is 5-10 % of the photocatalytic activity of the pure TiO_2 sample. This is in good agreement with the photocatalyst content of the TiO_2 paint samples (~10 %).

While the addition of copper in the paint matrix decreased the photonic efficiency, the addition of cobalt, zinc and iron slightly improved the NO degradation of the samples. Furthermore, the paint sample containing lithium displayed the highest photonic efficiency. Deeper analysis of the properties of the paint samples is required. Future scientific studies utilizing self-made paint samples with varying compositions should further investigate the observed changes in the photocatalytic NO degradation.

For example, the noble character of copper could lead to the reduction of copper ions into metallic copper. During this reduction process the consumed electrons are not available for photocatalytic NO degradation. However, the presence of noble metals, such as copper, platinum or gold, usually improves the photocatalytic reduction processes due to the transfer of the electrons in the CB of TiO₂ to the metal particles.¹⁸⁴ The utilization of lithium, on the other hand, might improve the photocatalytic process by secondary effects such as the reduction of the sodium ion amount in the sample. This result agrees with the previous results observed in this work for the TiO₂ samples mixed with Na₂CO₃.

In contrast to the previous studies on TiO₂-additive and mixed TiO₂ samples, all of the TiO₂ paint samples revealed quite constant NO adsorption (cf. **Figure 4.29**). Therefore, the paint samples have similar active surface areas and no effect of the surface area on the photocatalytic NO degradation is expected.

Despite the aforementioned assumptions dealing with the observed photocatalytic efficiencies of the different paint samples, correlations between the charge carrier recombination kinetics and the photocatalytic activity are identified in **Figure 5.34**. As explained in **Chapter 4.4**, the fractal kinetics fit was employed on the transient reflectance signal of the paint samples at 500 nm in the time-scale 6-200 μ s. In **Figure 5.34A** the obtained beginning height A , the fractal rate constants $k_{2,f}$, and the inverse fractal rate constants are plotted against the photonic efficiencies of the respective samples.

Figure 5.34 reveals identical connections between the charge carrier kinetics and the photocatalytic activity as observed for the other samples investigated in this study. Like the TiO₂-additive samples (cf. **Figure 5.30** and **Figure 5.28**), the TiO₂ paints with higher photocatalytic activity show larger transient reflectance signals, as indicated by the beginning height of the fractal kinetics fit in **Figure 5.34A**. The samples containing cobalt and zinc show a small deviation from the discussed trend. However, the parameter A of

these samples is influenced by the transient signals of the respective additives. Hence, the signal height is influenced by a photo-induced transient signal not belonging to TiO_2 .

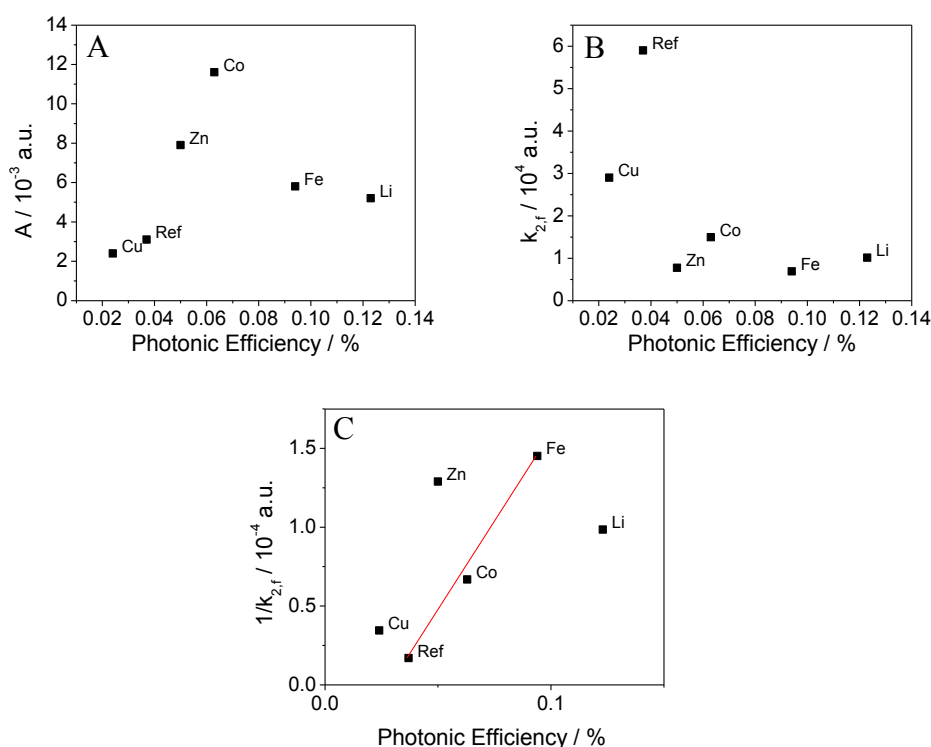


Figure 5.34: Beginning heights A (A), fractal rate constants $k_{2,F}$ (B), and inverse fractal rate constants (C) of the fractal kinetics fit of the transient reflectance signals of charge carriers photo-generated in TiO_2 paints measured at 500 nm after laser excitation (N_2 -saturated samples, laser excitation with 2 mJ/pulse, $\lambda_{ex}=355$ nm, fractal parameter $h=0.5$, time domain 6-200 μs) plotted against the respective photonic efficiency taken from the photocatalytic NO degradation with linear fit function (red line). The labels of the data points indicate the additive in the paint matrix.

The fractal rate constant, being an indicator for the charge carrier recombination kinetics, is lower for the TiO_2 paint samples exhibiting higher photonic efficiency. Therefore, the samples with slower charge carrier recombination kinetics display larger photocatalytic activities (**Figure 5.34B**).

Identical to the correlations made in **Figure 5.24** for the two series of TiO_2 with binary particle size distribution, the photonic efficiency was plotted against the inverse fractal rate coefficient in **Figure 5.34C**. The inverse fractal rate coefficient can be seen as a quantity to describe the charge carrier lifetime. And identical to the TiO_2 samples with binary particle size distribution, the paints revealed a correlation between the charge carrier lifetime and the photonic efficiency.

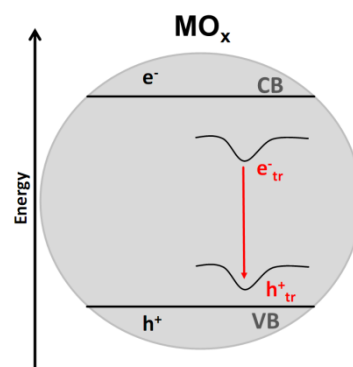
Although the additives employed in the TiO₂ paints displayed high transient signals at the first couple of microseconds, which overlap with the transient signals of the trapped charge carriers in TiO₂, the analysis of the charge carrier recombination in the time domain 6-200 μs was possible by the fractal kinetics fit. Moreover, even for such complex systems like commercial TiO₂ paints, a clear connection between charge carrier kinetics and photocatalytic NO degradation is found.

6. Summary and conclusions

Based on the fractal geometry of heterogeneous TiO₂ powder surfaces, the present study employs a fit function for the kinetic analysis of charge carrier recombination in TiO₂. In contrast to typically applied fit functions found in the literature, the proposed model was shown to successfully fit the transient reflectance signals observed for TiO₂ without the need of an arbitrary baseline. The observed fractal fit parameter h correlates with the particle size of the TiO₂ samples and is an intrinsic parameter, which is independent of laser intensity, analyzing wavelength and time-scale. Furthermore, the typically employed second order and power law fit functions were identified as border cases of the fractal kinetics fit, short and long periods of time after the laser excitation, respectively.

The good correlation between the experimental data and the fit function is strong evidence for the conformity of the physical background of the fractal fit function. This is particularly true because the fractal fit function has a minimum number of fit parameters and the signals were observed over long time-scales. Furthermore, the fractal fit parameters are connected to the physical properties of the sample and give further insight into the underlying mechanism of the charge carrier recombination reactions.

To the best of the author's knowledge, this fractal kinetics fit was employed to analyze the charge carrier recombination kinetics of mixed TiO₂ samples for the first time. Furthermore, the application of the fractal kinetics fit is not limited to TiO₂ samples.



→ Fractal recombination dynamics of photo-generated charge carriers in semiconductor powder samples

Figure 6.1: Fractal recombination kinetics of charge carriers photo-generated in different semiconductor powders observed by TAS after laser excitation ($\lambda_{ex} = 355 \text{ nm}$).

For instance, the model can be utilized for the kinetic analysis of charge carrier recombination in other semiconductors, such as ferrites and tungsten oxide (**Figure 6.1**). Interestingly, the fractal parameters of these two semiconductors are equivalent to the fractal parameters detected for TiO₂. This demonstrates that charge carrier trapping and recombination kinetics in different semiconductor powder samples are similar. Consequently, the mathematical analysis with the fractal fit function facilitates a deeper understanding of the photocatalytic processes in general and the fractal kinetics fit indeed represents a feasible model for a meaningful kinetic analysis of charge carrier recombination dynamics in photocatalytic systems.

Unfortunately, the fractal fit of a TRMC signal measured for P25 did not reveal the same fractal parameter as observed upon analysis of the TAS signals. It appears that different kinetics is observed due to the diverging underlying phenomena. Another drawback of the proposed fractal fit is the still existing uncertainty about the physical interpretation of the fractal parameter. The author recommends that the correlation between the sample properties and the fractal parameter should be a key element for future investigations.

Furthermore, the effects on the charge carrier recombination kinetics and photocatalytic activity observed upon mixing of TiO₂ powders with different particle size distributions were investigated in this study. Similar to the second order fit, the fractal kinetics fit function revealed a decrease in the recombination rate constant for the samples containing higher amounts of small particles. Hence, it was concluded that the changes in the second order rate constants can qualitatively be compared with the results observed for the fractal rate constant. However, the beneficial properties of the fractal kinetics fit, in comparison to the second order fit with baseline, were confirmed by a better correlation between the results of the photocatalytic NO degradation and the respective rate constants.

Since TiO₂ powder samples with binary particle size distributions were analyzed for the first time in this study, the present work contributes only a small piece to the complete understanding of the correlation between particle size and photocatalytic performance of TiO₂. Nevertheless, the results of the kinetic analysis correlate well with the obtained photocatalytic efficiencies. To the best of the author's knowledge, photocatalytic NO degradation was correlated with the kinetic analysis of the transient charge carrier signals for the first time. A slower recombination of trapped charge carriers in the TiO₂ mixtures with a larger content of small particles matches the larger photocatalytic NO degradation

of the respective samples (**Figure 6.2**). The formation of large agglomerates and the respective transfer of charge carriers in these agglomerates, according to the antenna mechanism, proved to be key factors influencing the observed photocatalytic activity of the samples.

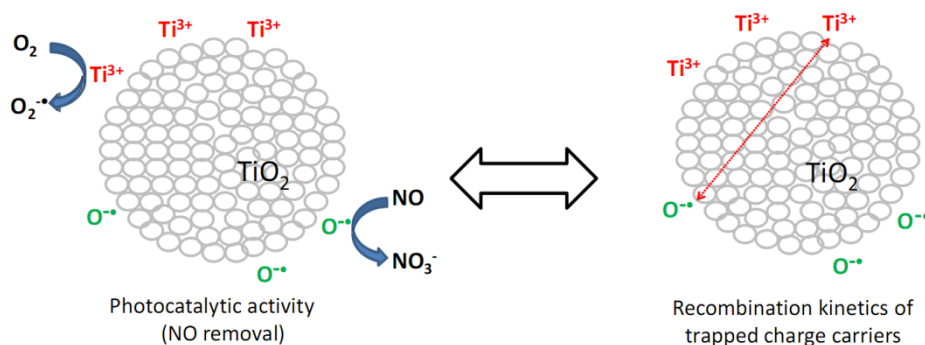


Figure 6.2: Correlation of the recombination kinetics of trapped charge carriers photo-generated in TiO₂ agglomerates and the respective photocatalytic activity of the TiO₂ samples determined by the photocatalytic NO degradation.

The surface area of the photocatalyst demonstrated only a small effect on the photocatalytic NO degradation. Moreover, the present study indicated that the adsorbed amount of the probe molecule under specific experimental conditions is a better tool for the quantitative analysis of the available surface area of powder samples than the utilization of the BET surface area. Therefore, a larger amount of NO adsorbed on the sample surface correlated with a higher photocatalytic NO decomposition. The photocatalytic performance of the two mixed TiO₂ series could overall be related to a combination of charge carrier lifetime and active surface area.

Apart from the investigation of pure TiO₂ samples, the NO degradation experiments and transient reflectance spectroscopy were carried out with TiO₂ powder samples ground with additives. These additives, two carbonates and a sulfate, were selected as model compounds for construction materials. BaSO₄ proved to be a chemically inert material, while mixing TiO₂ with Na₂CO₃ and CaCO₃ displayed two opposing trends.

The large photocatalytic performances of the TiO₂-BaSO₄ samples were caused by the strong scattering of UV light by the BaSO₄ particles. Despite the low contents of photocatalyst (between 5 and 50 % TiO₂), all respective powder samples displayed a high absorption of UV-light due to the strong scattering of light inside the samples. As a

consequence of the high scattering of UV light, the samples containing only 10-25 % TiO_2 displayed photocatalytic activities identical to the values obtained for the pure photocatalyst. Hence, by improving the UV light absorption, the required amount of photocatalyst can be minimized.

The present study reveals the importance of apparent quantum yields in contrast to photonic efficiencies. In particular, if additives are mixed with TiO_2 . Since the apparent quantum yields are normalized to the amount of absorbed light, samples with diverging optical properties can still be characterized. The quantum yields obtained in this work for TiO_2 -additive samples correlate well with the charge carrier kinetics. This is in good agreement with the same correlation of the quantum yields and charge carrier kinetics observed for pure TiO_2 samples.

With the help of the fractal kinetics fit applied to the charge carrier kinetics that was observed for the TiO_2 - Na_2CO_3 samples, a faster recombination of the charge carriers in TiO_2 - Na_2CO_3 samples was identified (**Figure 6.3**). CaCO_3 stabilizes the trapped charge carriers on the TiO_2 surface, which was identified by higher initial transient reflectance signals. Therefore, the TiO_2 samples ground with CaCO_3 showed increased photocatalytic activities, in contrast to the TiO_2 - Na_2CO_3 samples. Consequently, the application of CaCO_3 should be favored for the production of carbonate-containing photocatalytically active construction materials.

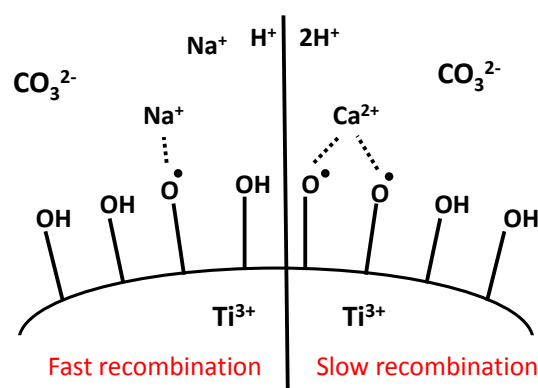


Figure 6.3: Effect of Na_2CO_3 and CaCO_3 on the stabilization of trapped charge carriers on the TiO_2 surface and the respective influence of the stabilized charge carriers on the charge carrier recombination kinetics.

The results obtained for the TiO_2 paints illustrate the viability of the fractal kinetics fit function as well. Even in such complex systems with overlapping transient signals, it was possible to correlate the charge carrier lifetimes in TiO_2 with the photocatalytic NO

degradation. This is a very important finding, since the application of TiO₂ on construction materials represents one of the few viable possibilities for utilizing a photocatalytic approach to air treatment on a large technical scale.

Throughout this work, a deeper understanding of the photocatalytic process occurring on the semiconductor surface was achieved. The present work clearly indicates that the kinetic analysis of the charge carrier signals in photocatalytic systems is essential, since the charge carrier concentration and the respective recombination kinetics represent key factors influencing the photocatalytic performance. Hence, these properties should not only be tested for TiO₂-composites employed in gas phase degradation experiments. Moreover, the fractal kinetics fit represents an effective tool for the analysis of the charge carrier recombination kinetics and for the assessment of the photocatalytic performance.

7. References

- (1) Jacobson, M. Z. The Short-Term Cooling but Long-Term Global Warming Due to Biomass Burning. *J. Clim.* **2004**, *17* (15), 2909–2926.
- (2) Easterling, D. R.; Meehl, G. A.; Parmesan, C.; Changnon, S. A.; Karl, T. R.; Mearns, L. O. Climate Extremes: Observations, Modeling, and Impacts. *Science* **2000**, *289* (5487), 2068–2074.
- (3) WHO. *WHO Air Quality Guidelines for Particulate Matter, Ozone, Nitrogen Dioxide and Sulfur Dioxide: Global Update 2005*; 2005.
- (4) *Inventory of U.S. Greenhouse Gas Emissions and Sinks: 1990-2015*; 2017.
- (5) Oldenkamp, R.; Van Zelm, R.; Huijbregts, M. A. J. Valuing the Human Health Damage Caused by the Fraud of Volkswagen. *Environ. Pollut.* **2016**, *212*, 121–127.
- (6) Mills, A.; Davies, R. H.; Worsley, D. Water Purification by Semiconductor Photocatalysis. *Chem. Soc. Rev.* **1993**, *22* (6), 417–425.
- (7) Bahnemann, D. W. Photocatalytic Water Treatment: Solar Energy Applications. *Sol. Energy* **2004**, *77* (5), 445–459.
- (8) Wright, J.; Gundry, S.; Conroy, R. Household Drinking Water in Developing Countries: A Systematic Review of Microbiological Contamination between Source and Point-of-Use. *Trop. Med. Int. Heal.* **2004**, *9* (1), 106–117.
- (9) Gadgil, A. Drinking Water in Developing Countries. *Annu. Rev. Energy Env.* **1998**, *23* (11), 253–286.
- (10) Huang, X.; Qu, Y.; Cid, C. A.; Finke, C.; Hoffmann, M. R.; Lim, K.; Jiang, S. C. Electrochemical Disinfection of Toilet Wastewater Using Wastewater Electrolysis Cell. *Water Res.* **2016**, *92*, 164–172.
- (11) Pattanaik, P.; Sahoo, M. K. TiO₂ Photocatalysis: Progress from Fundamentals to Modification Technology. *Desalin. Water Treat.* **2013**, *52* (34–36), 6567–6590.
- (12) Mills, A.; Le Hunte, S. An Overview of Semiconductor Photocatalysis. *J. Photochem. Photobiol. A Chem.* **1997**, *108* (1), 1–35.
- (13) Parida, B.; Iniyar, S.; Goic, R. A Review of Solar Photovoltaic Technologies. *Renew. Sustain. Energy Rev.* **2011**, *15* (3), 1625–1636.
- (14) Hoffmann, M. R.; Martin, S. T.; Choi, W.; Bahnemann, D. W. Environmental Applications of Semiconductor Photocatalysis. *Chem. Rev.* **1995**, *95* (1), 69–96.
- (15) Zhao, J.; Yang, X. Photocatalytic Oxidation for Indoor Air Purification: A Literature Review. *Build. Environ.* **2003**, *38* (5), 645–654.
- (16) Allen, N. S.; Edge, M.; Verran, J.; Stratton, J.; Maltby, J.; Bygott, C. Photocatalytic Titania Based Surfaces: Environmental Benefits. *Polym. Degrad. Stab.* **2008**, *93* (9), 1632–1646.
- (17) Khodadadian, F.; Nasalevich, M.; Kapteijn, F.; Stankiewicz, A. I.; Lakerveld, R.; Gascon, J. Photocatalysis: Past Achievements and Future Trends. In *Alternative Energy Sources for Green Chemistry*; 2016; pp 227–269.

- (18) Dionysiou, D. D.; Puma, G. L.; Ye, J.; Schneider, J.; Bahnemann, D. W. *Photocatalysis: Applications*; 2016.
- (19) Hernández-Alonso, M. D.; Fresno, F.; Suárez, S.; Coronado, J. M. Development of Alternative Photocatalysts to TiO₂: Challenges and Opportunities. *Energy Environ. Sci.* **2009**, 2 (12), 1231–1257.
- (20) Pelaez, M.; Nolan, N. T.; Pillai, S. C.; Seery, M. K.; Falaras, P.; Kontos, A. G.; Dunlop, P. S. M.; Hamilton, J. W. J.; Byrne, J. A.; O’Shea, K.; et al. A Review on the Visible Light Active Titanium Dioxide Photocatalysts for Environmental Applications. *Appl. Catal. B Environ.* **2012**, 125, 331–349.
- (21) Hu, Y.; Gao, X.; Yu, L.; Wang, Y.; Ning, J.; Xu, S.; Lou, X. W. Carbon-Coated CdS Petal-like Nanostructures with Enhanced Photostability and Photocatalytic Activity. *Angew. Chemie* **2013**, 52 (21), 5636–5639.
- (22) Serpone, N.; Lawless, D.; Khairutdinov, R.; Pelizzetti, E. Subnanosecond Relaxation Dynamics in TiO₂ Colloidal Sols (Particle Sizes $R_p = 1.0\text{--}13.4$ Nm). Relevance to Heterogeneous Photocatalysis. *J. Phys. Chem.* **1995**, 99 (45), 16655–16661.
- (23) Maggos, T.; Bartzis, J. G.; Liakou, M.; Gobin, C. Photocatalytic Degradation of NO_x Gases Using TiO₂-Containing Paint: A Real Scale Study. *J. Hazard. Mater.* **2007**, 146 (3), 668–673.
- (24) Gallus, M.; Akylas, V.; Barmpas, F.; Beeldens, A.; Boonen, E.; Boréave, A.; Cazaunau, M.; Chen, H.; Daele, V.; Doussin, J. F.; et al. Photocatalytic De-Pollution in the Leopold II Tunnel in Brussels: NO_x Abatement Results. *Build. Environ.* **2015**, 84 (2), 125–133.
- (25) Papailias, I.; Todorova, N.; Giannakopoulou, T.; Yu, J.; Dimotikali, D.; Trapalis, C. Photocatalytic Activity of Modified G-C₃N₄/TiO₂ Nanocomposites for NO_x Removal. *Catal. Today* **2017**, 280, 37–44.
- (26) Guillard, C.; Puzenat, E.; Lachheb, H.; Houas, A.; Herrmann, J.-M. Why Inorganic Salts Decrease the TiO₂ Photocatalytic Efficiency. *Int. J. Photoenergy* **2005**, 7, 1–9.
- (27) Liu, B.; Zhao, X. A Kinetic Model for Evaluating the Dependence of the Quantum Yield of Nano-TiO₂ Based Photocatalysis on Light Intensity, Grain Size, Carrier Lifetime, and Minority Carrier Diffusion Coefficient: Indirect Interfacial Charge Transfer. *Electrochim. Acta* **2010**, 55 (12), 4062–4070.
- (28) Bahnemann, D. W.; Henglein, A.; Lilie, J.; Spanhel, L. Flash Photolysis Observation of the Absorption Spectra of Trapped Positive Holes and Electrons in Colloidal Titanium Dioxide. *J. Phys. Chem.* **1984**, 88 (4), 709–711.
- (29) Kessler, R. W.; Wilkinson, F. Diffuse Reflectance Triplet-Triplet Absorption Spectroscopy of Aromatic Hydrocarbons Chemisorbed on [Gamma]-Alumina. *J. Chem. Soc., Faraday Trans. 1* **1981**, 77 (2), 309–320.
- (30) Ohtani, B.; Bowman, R. M.; Colombo Jr., D. P.; Kominami, H.; Noguchi, H.; Uosaki, K. Femtosecond Diffuse Reflectance Spectroscopy of Aqueous Titanium(IV) Oxide Suspension: Correlation of Electron-Hole Recombination Kinetics with Photocatalytic Activity. *Chem. Lett.* **1998**, No. 7, 579–580.
- (31) Barroso, M.; Pendlebury, S. R.; Cowan, A. J.; Durrant, J. R. Charge Carrier

- Trapping, Recombination and Transfer in Hematite (α -Fe₂O₃) Water Splitting Photoanodes. *Chem. Sci.* **2013**, *4*, 2724–2734.
- (32) Murakami, Y.; Nishino, J.; Mesaki, T.; Nosaka, Y. Femtosecond Diffuse-Reflectance Spectroscopy of Various Commercially Available TiO₂ Powders. *Spectrosc. Lett.* **2011**, *44* (2), 88–94.
- (33) Tamaki, Y.; Furube, A.; Katoh, R.; Murai, M.; Hara, K.; Arakawa, H.; Tachiya, M. Trapping Dynamics of Electrons and Holes in a Nanocrystalline TiO₂ Film Revealed by Femtosecond Visible/Near-Infrared Transient Absorption Spectroscopy. *Comptes Rendus Chim.* **2006**, *9* (2), 268–274.
- (34) Draper, R. B.; Fox, M. A. Titanium Dioxide Photosensitized Reactions Studied by Diffuse Reflectance Flash Photolysis in Aqueous Suspensions of TiO₂ Powder. *Langmuir* **1990**, *6* (32), 1396–1402.
- (35) Furube, A.; Asahi, T.; Masuhara, H.; Yamashita, H.; Anpo, M. Charge Carrier Dynamics of Standard TiO₂ Catalysts Revealed by Femtosecond Diffuse Reflectance Spectroscopy. *J. Phys. Chem. B* **1999**, *103*, 3120–3127.
- (36) Grela, M. A.; Colussi, A. J. Kinetics of Stochastic Charge Transfer and Recombination Events in Semiconductor Colloids. Relevance to Photocatalysis Efficiency. *J. Phys. Chem.* **1996**, *3654* (96), 18214–18221.
- (37) Farner Budarz, J.; Turolla, A.; Piasecki, A. F.; Bottero, J.-Y.; Antonelli, M.; Wiesner, M. R. Influence of Aqueous Inorganic Anions on the Reactivity of Nanoparticles in TiO₂ Photocatalysis. *Langmuir* **2017**, *33*, 2270–2279.
- (38) Barndok, H.; Hermosilla, D.; Cortijo, L.; Negro, C.; Blanco, A. Assessing the Effect of Inorganic Anions on TiO₂-Photocatalysis and Ozone Oxidation Treatment Efficiencies. *J. Adv. Oxid. Technol.* **2012**, *15* (1), 125–132.
- (39) Ryu, J.; Choi, W. Substrate-Specific Photocatalytic Activities of TiO₂ and Multiactivity Test for Water Treatment Application. *Environ. Sci. Technol.* **2008**, *42* (1), 294–300.
- (40) Boyjoo, Y.; Sun, H.; Liu, J.; Pareek, V. K.; Wang, S. A Review on Photocatalysis for Air Treatment: From Catalyst Development to Reactor Design. *Chem. Eng. J.* **2017**, *310*, 537–559.
- (41) Augugliaro, V.; Camera-Roda, G.; Loddo, V.; Palmisano, G.; Palmisano, L.; Soria, J.; Yurdakal, S. Heterogeneous Photocatalysis and Photoelectrocatalysis: From Unselective Abatement of Noxious Species to Selective Production of High-Value Chemicals. *J. Phys. Chem. Lett.* **2015**, *6* (10), 1968–1981.
- (42) Friedmann, D.; Hakki, A.; Kim, H.; Choi, W.; Bahnemann, D. W. Heterogeneous Photocatalytic Organic Synthesis: State-of-the-Art and Future Perspectives. *Green Chem.* **2016**, *18* (20), 5391–5411.
- (43) Chen, J.; Poon, C. S. Photocatalytic Construction and Building Materials: From Fundamentals to Applications. *Build. Environ.* **2009**, *44* (9), 1899–1906.
- (44) Hagfeldt, A.; Grätzel, M. Light-Induced Redox Reactions in Nanocrystalline Systems. *Chem. Rev.* **1995**, *95* (1), 49–68.
- (45) Fox, M. A.; Dulay, M. T. Heterogeneous Photocatalysis. *Chem. Rev.* **1993**, *93* (1),

- 341–357.
- (46) Bhatkhande, D. S.; Pangarkar, V. G.; Beenackers, A. A. C. M. Photocatalytic Degradation for Environmental Applications - A Review. *J. Chem. Technol. Biotechnol.* **2002**, *77* (1), 102–116.
- (47) Schneider, J.; Matsuoka, M.; Takeuchi, M.; Zhang, J.; Horiuchi, Y.; Anpo, M.; Bahnemann, D. W. Understanding TiO₂ Photocatalysis : Mechanisms and Materials. *Chem. Rev.* **2014**, *114*, 9919–9986.
- (48) Sieland, F.; Schneider, J.; Bahnemann, D. W. Photocatalytic Activity and Charge Carrier Dynamics of TiO₂ Powders with Binary Particle Size Distribution. *Phys. Chem. Chem. Phys.* **2018**, *20*, 8119–8132.
- (49) Granone, L. I.; Sieland, F.; Zheng, N.; Dillert, R.; Bahnemann, D. W. Photocatalytic Conversion of Biomass into Valuable Products- A Meaningful Approach? *Green Chem.* **2018**, *20*, 1169–1192.
- (50) Tachikawa, T.; Fujitsuka, M.; Majima, T. Mechanistic Insight into the TiO₂ Photocatalytic Reactions : Design of New Photocatalysts. *J. Phys. Chem. C* **2007**, *111* (14), 5259–5275.
- (51) Tachikawa, T.; Tojo, S.; Fujitsuka, M.; Majima, T. Influence of Metal Ions on the Charge Recombination Processes during TiO₂ Photocatalytic One-Electron Oxidation Reactions. *J. Phys. Chem. B* **2004**, *108* (30), 11054–11061.
- (52) Wunderlich, W.; Oekermann, T.; Miao, L.; Hue, N. T.; Tanemura, S.; Tanemura, M. Electronic Properties of Nano-Porous TiO₂- and ZnO-Thin Films-Comparison of Simulations and Experiments. *J. Ceram. Process. Res.* **2004**, *5* (4), 343–354.
- (53) Kandiel, T. A.; Feldhoff, A.; Robben, L.; Dillert, R.; Bahnemann, D. W. Tailored Titanium Dioxide Nanomaterials: Anatase Nanoparticles and Brookite Nanorods as Highly Active Photocatalysts. *Chem. Mater.* **2010**, *22* (6), 2050–2060.
- (54) Gupta, S. M.; Tripathi, M. A Review of TiO₂ Nanoparticles. *Chinese Sci. Bull.* **2011**, *56* (16), 1639–1657.
- (55) Carp, O.; Huisman, C. L.; Reller, A. Photoinduced Reactivity of Titanium Dioxide. *Prog. Solid State Chem.* **2004**, *32* (1–2), 33–177.
- (56) Viswanathan, B.; Raj, K. J. A. Effect of Surface Area, Pore Volume and Particle Size of P25 Titania on the Phase Transformation of Anatase to Rutile. *Indian J. Chem. - Sect. A Inorganic, Phys. Theor. Anal. Chem.* **2009**, *48* (10), 1378–1382.
- (57) Diebold, U. The Surface Science of Titanium Dioxide. *Surf. Sci. Rep.* **2003**, *48* (5–8), 53–229.
- (58) Tanaka, K.; Capule, M. F. V; Hisanaga, T. Effect of Crystallinity of TiO₂ on Its Photocatalytic Action. *Chem. Phys. Lett.* **1991**, *187* (1–2), 73–76.
- (59) Li, G.; Chen, L.; Graham, M. E.; Gray, K. A. A Comparison of Mixed Phase Titania Photocatalysts Prepared by Physical and Chemical Methods: The Importance of the Solid-Solid Interface. *J. Mol. Catal. A Chem.* **2007**, *275* (1–2), 30–35.
- (60) Hernández Rodríguez, M. J.; Pulido Melián, E.; González Díaz, O.; Araña, J.; Macías, M.; González Orive, A.; Doña Rodríguez, J. M. Comparison of Supported TiO₂ Catalysts in the Photocatalytic Degradation of NO_x. *J. Mol. Catal. A Chem.*

- 2016, 413, 56–66.
- (61) Hall, S.; Bradley, T.; Moore, J. T.; Kuykindall, T.; Minella, L. Acute and Chronic Toxicity of Nano-Scale TiO₂ Particles to Freshwater Fish, Cladocerans, and Green Algae, and Effects of Organic and Inorganic Substrate on TiO₂ Toxicity. *Nanotoxicology* **2009**, 3 (2), 91–97.
- (62) Tong, T.; Shereef, A.; Wu, J.; Binh, C. T. T.; Kelly, J. J.; Gaillard, J. F.; Gray, K. A. Effects of Material Morphology on the Phototoxicity of Nano-TiO₂ to Bacteria. *Environ. Sci. Technol.* **2013**, 47 (21), 12486–12495.
- (63) Friehs, E.; AlSalka, Y.; Jonczyk, R.; Lavrentieva, A.; Jochums, A.; Walter, J. G.; Stahl, F.; Scheper, T.; Bahnemann, D. W. Toxicity, Phototoxicity and Biocidal Activity of Nanoparticles Employed in Photocatalysis. *J. Photochem. Photobiol. C Photochem. Rev.* **2016**, 29, 1–28.
- (64) Nosaka, Y.; Fox, M. A. Kinetics for Electron Transfer From Laser-Pulse-Irradiated Colloidal Semiconductors to Adsorbed Methylviologen. Dependence of the Quantum Yield on Incident Pulse Width. *J. Phys. Chem.* **1988**, 92 (7), 1893–1897.
- (65) Wang, X.; Kafizas, A.; Li, X.; Moniz, S. J. A.; Reardon, P. J. T.; Tang, J.; Parkin, I. P.; Durrant, J. R. Transient Absorption Spectroscopy of Anatase and Rutile: The Impact of Morphology and Phase on Photocatalytic Activity. *J. Phys. Chem. C* **2015**, 119 (19), 10439–10447.
- (66) Pendlebury, S. R.; Wang, X.; Le Formal, F.; Cornuz, M.; Kafizas, A.; Tilley, S. D.; Grätzel, M.; Durrant, J. R. Ultrafast Charge Carrier Recombination and Trapping in Hematite Photoanodes under Applied Bias. *J. Am. Chem. Soc.* **2014**, 136 (28), 9854–9857.
- (67) Tamaki, Y.; Furube, A.; Murai, M.; Hara, K.; Katoh, R.; Tachiya, M. Dynamics of Efficient Electron Hole Separation in TiO₂ Nanoparticles Revealed by Femtosecond Transient Absorption Spectroscopy under the Weak-Excitation Condition. *Phys. Chem. Chem. Phys.* **2007**, 9 (12), 1453–1460.
- (68) Ohtani, B. Titania Photocatalysis beyond Recombination: A Critical Review. *Catalysts* **2013**, 3 (4), 942–953.
- (69) Bahnemann, D. W.; Hilgendorff, M.; Memming, R. Charge Carrier Dynamics at TiO₂ Particles: Reactivity of Free and Trapped Holes. *J. Phys. Chem. B* **1997**, 101 (21), 4265–4275.
- (70) Yang, X.; Tamai, N. How Fast Is Interfacial Hole Transfer? In Situ Monitoring of Carrier Dynamics in Anatase TiO₂ Nanoparticles by Femtosecond Laser Spectroscopy. *Phys. Chem. Chem. Phys.* **2001**, 3, 3393–3398.
- (71) Fujishima, A.; Rao, T. N.; Tryk, D. A. Titanium Dioxide Photocatalysis. *J. Photochem. Photobiol. C Photochem. Rev.* **2000**, 1 (1), 1–21.
- (72) Krumova, K.; Cosa, G. Chapter I: Overview of Reactive Oxygen Species. In *Singlet Oxygen : Applications in Biosciences and Nanosciences*; 2016; pp 3–21.
- (73) Shindell, D. T.; Rind, D.; Lonergan, P. Increased Polar Stratospheric Ozone Losses and Delayed Eventual Recovery Owing to Increasing Greenhouse-Gas Concentrations. *Nature* **1998**, 392, 589–592.

- (74) Ravishankara, A. R.; Daniel, J. S.; Portmann, R. W. Nitrous Oxide (N₂O): The Dominant Ozone-Depleting Substance Emitted in the 21st Century. *Science* **2009**, *326* (5949), 123–125.
- (75) Chan, C. C. An Overview of Electric Vehicle Technology. *Proc. IEEE* **1993**, *81* (9), 1202–1213.
- (76) Situ, L. Electric Vehicle Development: The Past, Present & Future. In *3rd Int. Conference on Power Electronics Systems and Applications*; 2009.
- (77) Lyu, J.; Zhu, L.; Burda, C. Considerations to Improve Adsorption and Photocatalysis of Low Concentration Air Pollutants on TiO₂. *Catal. Today* **2014**, *225*, 24–33.
- (78) Mo, J.; Zhang, Y.; Xu, Q.; Lamson, J. J.; Zhao, R. Photocatalytic Purification of Volatile Organic Compounds in Indoor Air: A Literature Review. *Atmos. Environ.* **2009**, *43* (14), 2229–2246.
- (79) Zhong, L.; Haghghat, F. Photocatalytic Air Cleaners and Materials Technologies - Abilities and Limitations. *Build. Environ.* **2015**, *91*, 191–203.
- (80) Mills, A.; Burns, L.; O'Rourke, C.; Elouali, S. Kinetics of the Photocatalysed Oxidation of NO in the ISO 22197 Reactor. *J. Photochem. Photobiol. A Chem.* **2016**, *321*, 137–142.
- (81) Likens, G. E.; Wright, R. F.; Galloway, J. N.; Butler, T. J. Acid Rain. *Sci. Am.* **1979**, *241* (4), 43–51.
- (82) Freitag, J.; Domínguez, A.; Niehaus, T. A.; Hülsewig, A.; Dillert, R.; Frauenheim, T.; Bahnemann, D. W. Nitrogen(II) Oxide Charge Transfer Complexes on TiO₂: A New Source for Visible-Light Activity. *J. Phys. Chem. C* **2015**, *119* (9), 4488–4501.
- (83) Laufs, S.; Burgeth, G.; Duttlinger, W.; Kurtenbach, R.; Maban, M.; Thomas, C.; Wiesen, P.; Kleffmann, J. Conversion of Nitrogen Oxides on Commercial Photocatalytic Dispersion Paints. *Atmos. Environ.* **2010**, *44* (19), 2341–2349.
- (84) Mills, A.; Elouali, S. The Nitric Oxide ISO Photocatalytic Reactor System: Measurement of NO_x Removal Activity and Capacity. *J. Photochem. Photobiol. A Chem.* **2015**, *305*, 29–36.
- (85) Ângelo, J.; Andrade, L.; Mendes, A. Highly Active Photocatalytic Paint for NO_x Abatement under Real-Outdoor Conditions. *Appl. Catal. A Gen.* **2014**, *484*, 17–25.
- (86) Maggos, T.; Plassais, A.; Bartzis, J. G.; Vasilakos, C.; Moussiopoulos, N.; Bonafous, L. Photocatalytic Degradation of NO_x in a Pilot Street Canyon Configuration Using TiO₂-Mortar Panels. *Environ. Monit. Assess.* **2008**, *136*, 35–44.
- (87) Sikkema, J. K.; Ong, S. K.; Alleman, J. E. Photocatalytic Concrete Pavements: Laboratory Investigation of NO Oxidation Rate under Varied Environmental Conditions. *Constr. Build. Mater.* **2015**, *100*, 305–314.
- (88) Gandolfo, A.; Bartolomei, V.; Gomez Alvarez, E.; Tlili, S.; Gligorovski, S.; Kleffmann, J.; Wortham, H. The Effectiveness of Indoor Photocatalytic Paints on NO_x and HONO Levels. *Appl. Catal. B Environ.* **2015**, *166–167* (2), 84–90.
- (89) Ballari, M. M.; Brouwers, H. J. H. Full Scale Demonstration of Air-Purifying Pavement. *J. Hazard. Mater.* **2013**, *254–255* (1), 406–414.

-
- (90) Guerrini, G. L.; Peccati, E. Photocatalytic Cementitious Roads for Depollution. In *International RILEM Symposium on Photocatalysis, Environment and Construction Materials - TDP 2007*; Cassar, P. B. and L., Ed.; RILEM Publications SARL, 2007; pp 179–186.
- (91) PICADA. European PICADA project, growth project GRD1-2001-40449. 2006. <http://www.picada-project.com/domino/SitePicada/Picada.nsf?> (accessed Nov 23, 2017).
- (92) Rijkswaterstaat Centre for Transport and Navigation. Dutch Air Quality Innovation Programme <http://www.ipl-airquality.nl/> (accessed Nov 23, 2017).
- (93) Tera. In Situ Study of the Air Pollution Mitigating Properties of Photocatalytic Coating, Tera Environment, (Contract Number 0941C0978). Report for ADEME and Rhone-Alpe Region. <http://www.air-rhonealpes.fr/site/media/telecharger/651413> (accessed Nov 23, 2017).
- (94) Mamaghani, A. H.; Haghghat, F.; Lee, C. S. Photocatalytic Oxidation Technology for Indoor Environment Air Purification: The State-of-the-Art. *Appl. Catal. B Environ.* **2017**, *203*, 247–269.
- (95) Ao, C. H.; Lee, S. C. Enhancement Effect of TiO₂ Immobilized on Activated Carbon Filter for the Photodegradation of Pollutants at Typical Indoor Air Level. *Appl. Catal. B Environ.* **2003**, *44* (3), 191–205.
- (96) Hay, S. O.; Obee, T. N.; Thibaud-Erkey, C. The Deactivation of Photocatalytic Based Air Purifiers by Ambient Siloxanes. *Appl. Catal. B Environ.* **2010**, *99* (3–4), 435–441.
- (97) Chen, H. Y.; Zahraa, O.; Bouchy, M. Inhibition of the Adsorption and Photocatalytic Degradation of an Organic Contaminant in an Aqueous Suspension of TiO₂ by Inorganic Ions. *J. Photochem. Photobiol. A Chem.* **1997**, *108*, 37–44.
- (98) Reynal, A.; Lakadamyali, F.; Gross, M. a.; Reisner, E.; Durrant, J. R. Parameters Affecting Electron Transfer Dynamics from Semiconductors to Molecular Catalysts for the Photochemical Reduction of Protons. *Energy Environ. Sci.* **2013**, *6* (11), 3291–3300.
- (99) Sze, S. M.; Ng, K. K. *Physics of Semiconductor Devices*; Wiley, 2007.
- (100) Le Formal, F.; Pendlebury, S. R.; Cornuz, M.; Tilley, S. D.; Grätzel, M.; Durrant, J. R. Back Electron-Hole Recombination in Hematite Photoanodes for Water Splitting. *J. Am. Chem. Soc.* **2014**, *136* (6), 2564–2574.
- (101) Wilkinson, F. Diffuse Reflectance Flash Photolysis. *J. Chem. Soc. Faraday Trans. 2* **1986**, *82* (12), 2073–2081.
- (102) Cowan, A. J.; Leng, W.; Barnes, P. R. F.; Klug, D. R.; Durrant, J. R. Charge Carrier Separation in Nanostructured TiO₂ Photoelectrodes for Water Splitting. *Phys. Chem. Chem. Phys.* **2013**, *15* (22), 8772–8778.
- (103) Serpone, N.; Lawless, D.; Khairutdinov, R. Size Effects on the Photophysical Properties of Colloidal Anatase TiO₂ Particles: Size Quantization versus Direct Transitions in This Indirect Semiconductor? *J. Phys. Chem.* **1995**, *99* (45), 16646–16654.
-

- (104) Yan, J.; Wu, G.; Guan, N.; Li, L.; Li, Z.; Cao, X. Understanding the Effect of Surface/Bulk Defects on the Photocatalytic Activity of TiO₂: Anatase versus Rutile. *Phys. Chem. Chem. Phys.* **2013**, *15* (26), 10978–10988.
- (105) Martin, S. T.; Herrmann, H.; Choi, W.; Hoffmann, M. R. Time-Resolved Microwave Conductivity. *J. Chem. Soc.* **1994**, *90* (21), 3315–3322.
- (106) Tahiri Alaoui, O.; Herissan, A.; Le Quoc, C.; Zekri, M. E. M.; Sorgues, S.; Remita, H.; Colbeau-Justin, C. Elaboration, Charge-Carrier Lifetimes and Activity of Pd-TiO₂ Photocatalysts Obtained by Gamma Radiolysis. *J. Photochem. Photobiol. A Chem.* **2012**, *242*, 34–43.
- (107) Katoh, R.; Tamaki, Y.; Furube, A. Primary Photocatalytic Reactions in TiO₂ Nanoparticles Studied by Time-Resolved Laser Spectroscopy. In *Proc. of SPIE*; 2011; Vol. 8109, pp 1–8.
- (108) Henglein, A. Colloidal TiO₂ Catalyzed Photo- and Radiation Chemical Processes in Aqueous Solution. *Berichte der Bunsengesellschaft/Physical Chem. Chem. Phys.* **1982**, *86* (3), 241–245.
- (109) Yoshihara, T.; Katoh, R.; Furube, A.; Tamaki, Y.; Murai, M.; Hara, K.; Murata, S.; Arakawa, H. Identification of Reactive Species in Photoexcited Nanocrystalline TiO₂ Films by Wide-Wavelength-Range (400–2500 Nm) Transient Absorption Spectroscopy. *J. Phys. Chem. B* **2004**, *108* (12), 3817–3823.
- (110) Howe, R. F.; Grätzel, M. EPR Study of Hydrated Anatase under UV Irradiation. *J. Phys. Chem.* **1987**, *91* (14), 3906–3909.
- (111) Zawadzki, P. Absorption Spectra of Trapped Holes in Anatase TiO₂. *J. Phys. Chem. C* **2013**, *117* (17), 8647–8651.
- (112) Feng, H.; Tan, S.; Tang, H.; Zheng, Q.; Shi, Y.; Cui, X.; Shao, X.; Zhao, A.; Zhao, J.; Wang, B. Temperature- and Coverage-Dependent Kinetics of Photocatalytic Reaction of Methanol on TiO₂(110)-(1x1) Surface. *J. Phys. Chem. C* **2016**, *120* (10), 5503–5514.
- (113) Bao, J.; Yu, Z.; Gundlach, L.; Benedict, J. B.; Coppens, P.; Chen, H. C.; Miller, J. R.; Piotrowiak, P. Excitons and Excess Electrons in Nanometer Size Molecular Polyoxotitanate Clusters: Electronic Spectra, Exciton Dynamics, and Surface States. *J. Phys. Chem. B* **2013**, *117* (16), 4422–4430.
- (114) Katoh, R.; Murai, M.; Furube, A. Electron-Hole Recombination in the Bulk of a Rutile TiO₂ Single Crystal Studied by Sub-Nanosecond Transient Absorption Spectroscopy. *Chem. Phys. Lett.* **2008**, *461*, 238–241.
- (115) Schindler, K. M.; Kunst, M. Charge-Carrier Dynamics in Titania Powders. *J. Phys. Chem.* **1990**, *94* (21), 8222–8226.
- (116) Kopelman, R. Fractal Reaction Kinetics. *Science* **1988**, *241* (4873), 1620–1626.
- (117) Schneider, J.; Nikitin, K.; Dillert, R.; Bahnemann, D. W. Laser-Flash-Photolysis-Spectroscopy: A Nondestructive Method? *Faraday Discuss.* **2017**, *197*, 505–516.
- (118) Niklasson, G. A. Fractal Aspects of the Dielectric Response of Charge Carriers in Disordered Materials. *J. Appl. Phys.* **1987**, *62* (7).
- (119) Hirakawa, T.; Nosaka, Y. Properties of O₂^{•-} and OH[•] Formed in TiO₂ Aqueous

- Suspensions by Photocatalytic Reaction and the Influence of H₂O₂ and Some Ions. *Langmuir* **2002**, *18* (8), 3247–3254.
- (120) Zhou, C.; Ma, Z.; Ren, Z.; Mao, X.; Dai, D.; Yang, X. Effect of Defects on Photocatalytic Dissociation of Methanol on TiO₂(110). *Chem. Sci.* **2011**, *2* (10), 1980–1983.
- (121) Thompson, T. L.; Yates, J. T. Control of a Surface Photochemical Process by Fractal Electron Transport across the Surface: O₂ Photodesorption from TiO₂(110). *J. Phys. Chem. B* **2006**, *110* (14), 7431–7435.
- (122) Mandelbrot, B. B. *The Fractal Geometry of Nature*; W.H. Freeman And Company: New York, 1983.
- (123) Avnir, D.; Farin, D.; Pfeifer, P. Chemistry in Noninteger Dimensions between Two and Three. I. Fractal Theory of Heterogeneous Surfaces. *J. Chem. Phys.* **1983**, *79* (7), 3558–3565.
- (124) Le Mehaute, A.; Crepy, G. Introduction to Transfer and Motion in Fractal Media: The Geometry of Kinetics. *Solid State Ionics* **1983**, *9–10*, 17–30.
- (125) Arabatzis, I. M.; Antonaraki, S.; Stergiopoulos, T.; Hiskia, A.; Papaconstantinou, E.; Bernard, M. C.; Falaras, P. Preparation, Characterization and Photocatalytic Activity of Nanocrystalline Thin Film TiO₂ Catalysts towards 3,5-Dichlorophenol Degradation. *J. Photochem. Photobiol. A Chem.* **2002**, *149*, 237–245.
- (126) Wang, C. Y.; Pagel, R.; Bahnemann, D. W.; Dohrmann, J. K. Quantum Yield of Formaldehyde Formation in the Presence of Colloidal TiO₂-Based Photocatalysts: Effect of Intermittent Illumination, Platinization, and Deoxygenation. *J. Phys. Chem. B* **2004**, *108* (37), 14082–14092.
- (127) Tachiya, M.; Mozumder, A. Kinetics of Geminate-Ion Recombination by Electron Tunneling. *Chem. Phys. Lett.* **1975**, *34* (1), 77–79.
- (128) Barzykin, A. V.; Tachiya, M. Mechanism of Charge Recombination in Dye-Sensitized Nanocrystalline Semiconductors: Random Flight Model. *J. Phys. Chem. B* **2002**, *106* (17), 4356–4363.
- (129) Shuttle, C. G.; Hamilton, R.; Nelson, J.; O'Regan, B. C.; Durrant, J. R. Measurement of Charge-Density Dependence of Carrier Mobility in an Organic Semiconductor Blend. *Adv. Funct. Mater.* **2010**, *20* (5), 698–702.
- (130) Nelson, J.; Haque, S.; Klug, D.; Durrant, J. Trap-Limited Recombination in Dye-Sensitized Nanocrystalline Metal Oxide Electrodes. *Phys. Rev. B* **2001**, *63*, 205321–205330.
- (131) Tang, J.; Durrant, J. R.; Klug, D. R. Mechanism of Photocatalytic Water Splitting in TiO₂. Reaction of Water with Photoholes, Importance of Charge Carrier Dynamics, and Evidence for Four-Hole Chemistry. *J. Am. Chem. Soc.* **2008**, *130* (42), 13885–13891.
- (132) Pendlebury, S. R.; Barroso, M.; Cowan, A. J.; Sivula, K.; Tang, J.; Grätzel, M.; Klug, D.; Durrant, J. R. Dynamics of Photogenerated Holes in Nanocrystalline α -Fe₂O₃ Electrodes for Water Oxidation Probed by Transient Absorption Spectroscopy. *Chem. Commun. (Camb)*. **2011**, *47* (2), 716–718.

- (133) Wang, X.; Feng, Z.; Shi, J.; Jia, G.; Shen, S.; Zhou, J.; Li, C. Trap States and Carrier Dynamics of TiO₂ Studied by Photoluminescence Spectroscopy under Weak Excitation Condition. *Phys. Chem. Chem. Phys.* **2010**, *12* (26), 7083–7090.
- (134) Sieland, F.; Schneider, J.; Bahnemann, D. W. Fractal Charge Carrier Kinetics in TiO₂. *J. Phys. Chem. C* **2017**, *121* (43), 24282–24291.
- (135) Sieland, F.; Duong, N. A.; Schneider, J.; Bahnemann, D. W. D. W. Influence of Inorganic Additives on the Photocatalytic Removal of Nitric Oxide and on the Charge Carrier Dynamics of TiO₂ Powders. *J. Photochem. Photobiol. A Chem.* **2018**, DOI:10.1016/j.jphotochem.2018.01.036.
- (136) Grum, F.; Luckey, G. W. Optical Sphere Paint and a Working Standard of Reflectance. *Appl. Opt.* **1968**, *7* (11), 2289–2294.
- (137) Grum, F.; Wightman, T. E. Absolute Reflectance of Eastman White Reflectance Standard. **1985**, *16* (11), 2775–2776.
- (138) Schneider, J.; Nikitin, K.; Wark, M.; Bahnemann, D. W.; Marschall, R. Improved Charge Carrier Separation in Barium Tantalate Composites Investigated by Laser Flash Photolysis. *Phys. Chem. Chem. Phys.* **2016**, *18*, 10719–10726.
- (139) Lin, T.-P.; Kan, K. A. Calculation of Reflectance of a Light Diffuser with Nonuniform Absorption. *J. Opt. Soc. Am.* **1970**, *60* (9), 1–5.
- (140) Kisch, H.; Bahnemann, D. W. Best Practice in Photocatalysis: Comparing Rates or Apparent Quantum Yields? *J. Phys. Chem. Lett.* **2015**, *6* (10), 1907–1910.
- (141) Friedmann, D.; Hansing, H.; Bahnemann, D. W. Primary Processes During the Photodeposition of Ag Clusters on TiO₂ Nanoparticles. *Zeitschrift für Phys. Chemie* **2007**, *221* (3), 329–348.
- (142) Kessler, R. W.; Krabichler, G.; Uhl, S.; Oelkrug, D.; Hagan, W. P.; Hyslop, J.; Wilkinson, F. Transient Decay Following Pulse Excitation of Diffuse Scattering Samples. *Opt. Acta Int. J. Opt.* **1983**, *30* (8), 1099–1111.
- (143) Bloh, J. Z.; Folli, A.; Macphee, D. E. Photocatalytic NO_x Abatement: Why the Selectivity Matters. *RSC Adv.* **2014**, *4* (86), 45726–45734.
- (144) Sieland, F.; Schneider, J.; Lippmann, T.; Bahnemann, D. W. Understanding Charge Transfer Processes on Metal Oxides – A Laser-Flash-Photolysis Study. *Proc. SPIE* **2016**, 9935, 99350G1-10.
- (145) Gumy, D.; Giraldo, S. A.; Rengifo, J.; Pulgarin, C. Effect of Suspended TiO₂ Physicochemical Characteristics on Benzene Derivatives Photocatalytic Degradation. *Appl. Catal. B Environ.* **2008**, *78*, 19–29.
- (146) Kubelka, P. New Contributions to the Optics of Intensely Light-Scattering Materials. Part I. *J. Opt. Soc. Am.* **1948**, *38* (5), 448–457.
- (147) Howe, R. F.; Grätzel, M. EPR Observation of Trapped Electrons In Colloidal TiO₂. *J. Phys. Chem.* **1985**, *89* (21), 4495–4499.
- (148) Bahnemann, D.; Henglein, A.; Spanhel, L. Detection of the Intermediates of Colloidal TiO₂-Catalysed Photoreactions. *Faraday Discuss. Chem. Soc.* **1984**, *78*, 151–163.

-
- (149) Schneider, J. Nanosecond Laser Flash Photolysis Studies for the Elucidation of Photoinduced Processes in Different TiO₂ Photocatalysts, Gottfried Wilhelm Leibniz University Hannover, 2016.
- (150) Jellison, G. E.; Modine, F. A.; Boatner, L. A. Measurement of the Optical Functions of Uniaxial Materials by Two-Modulator Generalized Ellipsometry: Rutile (TiO₂). *Opt. Lett.* **1997**, *22* (23), 1808–1810.
- (151) Moringa, K.; Yoshida, H.; Takebe, H. Compositional Dependence of Absorption Spectra of Ti³⁺ in Silicate, Borate, and Phosphate Glasses. *J. Am. Ceram. Soc.* **1994**, *77* (12), 3113–3118.
- (152) Drouilly, C.; Krafft, J. M.; Averseng, F.; Lauron-Pernot, H.; Bazer-Bachi, D.; Chizallet, C.; Lecocq, V.; Costentin, G. Role of Oxygen Vacancies in the Basicity of ZnO: From the Model Methylbutynol Conversion to the Ethanol Transformation Application. *Appl. Catal. A Gen.* **2013**, *453*, 121–129.
- (153) Jing, L.; Zhou, J.; Durrant, J. R.; Tang, J.; Liu, D.; Fu, H. Dynamics of Photogenerated Charges in the Phosphate Modified TiO₂ and the Enhanced Activity for Photoelectrochemical Water Splitting. *Energy Environ. Sci.* **2012**, *5* (4), 6552–6558.
- (154) Szczepankiewicz, S. H.; Moss, J. A.; Hoffmann, M. R. Electron Traps and the Stark Effect on Hydroxylated Titania Photocatalysts. *J. Phys. Chem. B* **2002**, *106* (31), 7654–7658.
- (155) Wang, C.; Pagel, R.; Dohrmann, J. K.; Bahnemann, D. W. Antenna Mechanism and Deaggregation Concept: Novel Mechanistic Principles for Photocatalysis. *Comptes Rendus Chim.* **2006**, *9* (5–6), 761–773.
- (156) Wang, C.; Böttcher, C.; Bahnemann, D. W.; Dohrmann, J. K. A Comparative Study of Nanometer Sized Fe(III)-Doped TiO₂ Photocatalysts: Synthesis, Characterization and Activity. *J. Mater. Chem.* **2003**, *13* (9), 2322–2329.
- (157) Toussaint, D.; Wilczek, F. Particle–Antiparticle Annihilation in Diffusive Motion. *J. Chem. Phys.* **1983**, *78* (5), 2642–2647.
- (158) Barzykin, A. V.; Tachiya, M. Diffusion-Influenced Reaction Kinetics on Fractal Structures. *J. Chem. Phys.* **1993**, *99* (12), 9591–9597.
- (159) Egan, W. *Optical Properties of Inhomogeneous Materials: Applications to Geology, Astronomy, Chemistry, and Engineering*; 1979.
- (160) Kortüm, G. *Reflectance Spectroscopy: Principles, Methods, Applications*; 1969.
- (161) Lindberg, J. D.; Douglass, R. E.; Garvey, D. M. Absorption-Coefficient-Determination Method for Particulate Materials. *Appl. Opt.* **1994**, *33*, 4314–4319.
- (162) Wei, Z.; Kowalska, E.; Wang, K.; Colbeau-Justin, C.; Ohtani, B. Enhanced Photocatalytic Activity of Octahedral Anatase Particles Prepared by Hydrothermal Reaction. *Catal. Today* **2017**, *280*, 29–36.
- (163) Colbeau-Justin, C.; Valenzuela, M. A. Time-Resolved Microwave Conductivity (TRMC) a Useful Characterization Tool for Charge Carrier Transfer in Photocatalysis: A Short Review. *Rev. Mex. Fis.* **2013**, *59* (3), 191–200.
- (164) Colbeau-Justin, C.; Kunst, M.; Huguenin, D. Structural Influence on Charge-Carrier
-

- Lifetimes in TiO₂ Powders Studied by Microwave Absorption. *J. Mater. Sci.* **2003**, 38 (11), 2429–2437.
- (165) Bisquert, J. Interpretation of a Fractional Diffusion Equation with Nonconserved Probability Density in Terms of Experimental Systems with Trapping or Recombination. *Phys. Rev. E - Stat. Nonlinear, Soft Matter Phys.* **2005**, 72 (1), 1–6.
- (166) Zhang, Z.; Wang, C.; Zakaria, R.; Ying, J. Y. Role of Particle Size in Nanocrystalline TiO₂-Based Photocatalysts. *J. Phys. Chem. B* **1998**, 102, 10871–10878.
- (167) Gao, L.; Zhang, Q. Effects of Amorphous Contents and Particle Size on the Photocatalytic Properties of TiO₂ Nanoparticles. *Scr. Mater.* **2001**, 44 (8), 1195–1198.
- (168) Li, Z.; Liu, R.; Xu, Y. Larger Effect of Sintering Temperature Than Particle Size on the Photocatalytic Activity of Anatase TiO₂. *J. Phys. Chem. C* **2013**, 117, 24360–24367.
- (169) Zou, H.; Lin, Y. S. Structural and Surface Chemical Properties of Sol-Gel Derived TiO₂-ZrO₂ Oxides. *Appl. Catal. A Gen.* **2004**, 265 (1), 35–42.
- (170) Vittadini, A.; Selloni, A.; Rotzinger, F. P.; Grätzel, M. Structure and Energetics of Water Adsorbed at TiO₂ Anatase (101) and (001) Surfaces. *Phys. Rev. Lett.* **1998**, 81 (14), 2954–2957.
- (171) Takeuchi, M.; Sakamoto, K.; Martra, G.; Coluccia, S.; Anpo, M. Mechanism of Photoinduced Superhydrophilicity on the TiO₂ Photocatalyst Surface. *J. Phys. Chem. B* **2005**, 109 (32), 15422–15428.
- (172) Mendive, C. B.; Hansmann, D.; Bredow, T.; Bahnemann, D. New Insights into the Mechanism of TiO₂ Photocatalysis: Thermal Processes beyond the Electron-Hole Creation. *J. Phys. Chem. C* **2011**, 115 (40), 19676–19685.
- (173) Ivanova, I.; Mendive, C. B.; Bahnemann, D. The Role of Nanoparticulate Agglomerates in TiO₂ Photocatalysis: Degradation of Oxalic Acid. *J. Nanoparticle Res.* **2016**, 18 (7).
- (174) Boujday, S.; Wunsch, F.; Portes, P.; Bocquet, J. F.; Colbeau-Justin, C. Photocatalytic and Electronic Properties of TiO₂ Powders Elaborated by Sol-Gel Route and Supercritical Drying. *Sol. Energy Mater. Sol. Cells* **2004**, 83 (4), 421–433.
- (175) Xie, H.; Li, N.; Liu, B.; Yang, J.; Zhao, X. Role of Sodium Ion on TiO₂ Photocatalyst: Influencing Crystallographic Properties or Serving as the Recombination Center of Charge Carriers? *J. Phys. Chem. C* **2016**, 120 (19), 10390–10399.
- (176) Redmond, G.; Fitzmaurice, D. Spectroscopic Determination of Flatband Potentials for Polycrystalline TiO₂ Electrodes in Nonaqueous Solvents. *J. Phys. Chem.* **1993**, 97 (7), 1426–1430.
- (177) Dimarco, B. N.; O'Donnell, R. M.; Meyer, G. J. Cation-Dependent Charge Recombination to Organic Mediators in Dye-Sensitized Solar Cells. *J. Phys. Chem. C* **2015**, 119 (37), 21599–21604.

- (178) Ward, C. L.; O'Donnell, R. M.; DiMarco, B. N.; Meyer, G. J. Kinetic Resolution of Charge Recombination and Electric Fields at the Sensitized TiO₂ Interface. *J. Phys. Chem. C* **2015**, *119* (45), 25273–25281.
- (179) Chamousis, R. L.; Osterloh, F. E. Use of Potential Determining Ions to Control Energetics and Photochemical Charge Transfer of a Nanoscale Water Splitting Photocatalyst. *Energy Environ. Sci.* **2014**, *7* (2), 736–743.
- (180) Pelet, S.; Moser, J.-E.; Grätzel, M. Cooperative Effect of Adsorbed Cations and Iodide on the Interception of Back Electron Transfer in the Dye Sensitization of Nanocrystalline TiO₂. *J. Phys. Chem. B* **2000**, *104* (8), 1791–1795.
- (181) Wang, H.; Peter, L. M. Influence of Electrolyte Cations on Electron Transport and Electron Transfer in Dye-Sensitized Solar Cells. *J. Phys. Chem. C* **2012**, *116* (19), 10468–10475.
- (182) Johnston, J. The Solubility-Product Constant of Calcium and Magnesium Carbonates. *J. Am. Chem. Soc.* **1915**, *37* (9), 2001–2020.
- (183) Monnin, C.; Schott, J. Determination of the Solubility Products of Sodium Carbonate Minerals and an Application to Trona Deposition in Lake Magadi (Kenya). *Geochim. Cosmochim. Acta* **1984**, *48*, 571–581.
- (184) Binas, V.; Venieri, D.; Kotzias, D.; Kiriakidis, G. Modified TiO₂ Based Photocatalysts for Improved Air and Health Quality. *J. Mater.* **2017**, *3* (1), 3–16.

Appendix

Second order kinetics

Table S1: Fitting parameters and adjusted coefficients of determination (\bar{R}^2) of the second order fits with baseline ($\Delta J = \frac{A}{1+Ak_2t} + B$) of the transient reflectance signals of charge carriers photo-generated in the samples containing PC105 mixed with Kronos1001 observed at 500 nm in the time domain between 58 ns and 200 μ s after excitation with 1 mJ/cm² ($\lambda_{\text{ex}} = 355$ nm).

PC105 / %	$A / 10^{-2}$ a. u.	$k_2 / 10^7$ a.u	$B / 10^{-3}$ a. u.	\bar{R}^2
0.0	1.4	4.5	1.5	0.89
0.4	1.4	2.7	1.9	0.91
5.0	1.0	3.0	1.7	0.85
10.0	1.6	2.1	2.5	0.93
20.0	2.1	1.9	3.1	0.95
40.0	2.1	1.7	3.7	0.94
70.0	2.7	1.4	5.7	0.94
100.0	3.2	0.9	6.3	0.96

Table S2: Fitting parameters and adjusted coefficients of determination (\bar{R}^2) of the second order fits with baseline ($\Delta J = \frac{A}{1+Ak_2t} + B$) of the transient reflectance signals of charge carriers photo-generated in the samples containing PC105 mixed with Kronos1001 observed at 500 nm in the time domain between 5 μ s and 200 μ s after excitation with 1 mJ/cm² ($\lambda_{\text{ex}} = 355$ nm).

PC105 / %	$A / 10^{-2}$ a. u.	$k_2 / 10^7$ a.u	$B / 10^{-3}$ a. u.	\bar{R}^2
0.0	0.6	2.1	1.0	0.94
0.4	0.8	1.3	1.3	0.95
5.0	0.7	1.4	1.3	0.95
10.0	0.8	1.0	1.9	0.95
20.0	1.0	0.7	2.1	0.96
40.0	1.1	0.7	2.7	0.97
70.0	1.3	0.5	4.2	0.97
100.0	1.7	0.3	4.0	0.98

Table S3: Results of the second order fits with baseline ($\Delta J = \frac{A}{1+Ak_2t} + B$) of the transient reflectance signals of charge carriers photo-generated in PC105 observed at 500 nm after excitation with 1 mJ/cm² ($\lambda_{\text{ex}} = 355$ nm).

Time window	40 ns – 4.3 μs	4.3 μs – 9 μs	9 μs – 430 μs	430 μs – 899 μs
$k_2 / 10^6$ a. u.	137.26	9.82	2.66	0.87
$A / 10^{-2}$ a. u.	3.7	1.3	0.8	0.5
$B / 10^{-3}$ a. u.	7.97	0.29	1.34	0.21

Table S4: Fitting parameters and adjusted coefficients of determination (\bar{R}^2) of the second order kinetics fits of the transient reflectance signals of charge carriers photo-generated in samples containing PC105 observed at 500 nm after the excitation with varying laser intensity ($\lambda_{\text{ex}} = 355$ nm).

Laser intensity / mJ	$A / 10^{-2}$ a. u.	$k_2 / 10^6$ a.u	$B / 10^{-3}$ a. u.	\bar{R}^2
0.6	0.8	2.9	0.3	0.87
1.0	0.9	2.8	0.9	0.94
1.9	1.1	2.0	0.9	0.96
3.3	1.2	2.0	0.1	0.96
4.2	1.2	2.0	0.9	0.96
5.1	1.3	1.8	0.1	0.97

Fractal kinetics

Table S5: Fitting parameters and adjusted coefficients of determination (\bar{R}^2) of the fractal kinetics fits ($h = 0.5$) of the transient reflectance signals of charge carriers photo-generated in samples containing PC105 mixed with Kronos1001 at 500 nm in the time domain between 58 ns and 200 μ s after the excitation with 1 mJ/cm² ($\lambda_{\text{ex}} = 355$ nm).

PC105 / %	$A / 10^{-3}$ a.u.	$k_{2,f} / 10^4$ a.u.	\bar{R}^2
0.0	2.8	3.6	0.91
0.4	2.5	2.4	0.93
5.0	1.6	2.5	0.87
10.0	2.8	1.8	0.95
20.0	3.6	1.5	0.97
40.0	3.4	1.3	0.96
70.0	4.2	0.9	0.95
100.0	5.1	0.7	0.98

Table S6: Fitting parameters and adjusted coefficients of determination (\bar{R}^2) of the fractal kinetics fits ($h = 0.5$) of the transient reflectance signals of charge carriers photo-generated in the samples containing PC105 mixed with Kronos1001 at 500 nm in the time domain between 5 μ s and 200 μ s after excitation with 1 mJ/cm² ($\lambda_{\text{ex}} = 355$ nm).

PC105 / %	$A / 10^{-3}$ a.u.	$k_{2,f} / 10^4$ a.u.	\bar{R}^2
0.0	1.1	2.5	0.92
0.4	1.6	2.1	0.95
5.0	1.3	2.2	0.94
10.0	1.5	1.5	0.94
20.0	2.1	1.2	0.96
40.0	1.8	1.0	0.96
70.0	2.1	0.6	0.96
100.0	3.4	0.6	0.99

Table S7: Fitting parameters and adjusted coefficients of determination (\bar{R}^2) of the fractal kinetics fits ($h = 0.5$) of the transient reflectance signals of charge carriers photo-generated in samples containing PC105 observed at 500 nm after the excitation with varying laser intensity ($\lambda_{\text{ex}} = 355$ nm).

Laser intensity / mJ	$A / 10^{-3}$ a.u.	$k_{2,f} / 10^4$ a.u.	\bar{R}^2
0.6	17.4	1.8	0.86
1.0	2.4	1.3	0.95
1.9	3.7	1.0	0.96
3.3	3.8	1.0	0.97
4.2	5.0	0.9	0.96
5.1	4.9	0.8	0.97

Table S8: Fitting parameters and adjusted coefficients of determination (\bar{R}^2) of the fractal kinetics fits of the transient reflectance signals of charge carriers photo-generated in samples containing PC105 observed at 500 nm after the excitation with varying laser intensity ($\lambda_{\text{ex}} = 355$ nm).

Laser intensity / mJ	$A / 10^{-3}$ a.u.	$k_{2,f} / 10^4$ a.u.	h
0.6	1.3	1.8	0.40
1.0	1.8	1.3	0.46
1.9	1.8	1.1	0.42
3.3	2.0	1.0	0.45
4.2	1.8	0.9	0.49
5.1	2.2	0.9	0.46

Table S9. Fitting parameters and adjusted coefficients of determination (\bar{R}^2) of the second order kinetics fits of the transient reflectance signals of charge carriers photo-generated in the samples containing PC500 mixed with Kronos1001 at 500 nm in the time domain between 5 μ s and 200 μ s after excitation with 1 mJ/cm² ($\lambda_{\text{ex}} = 355$ nm).

PC500 / %	$A / 10^{-2}$ a. u.	$k_2 / 10^7$ a.u	$B / 10^{-3}$ a. u.	\bar{R}^2
0.0	0.7	1.1	1.5	0.95
0.4	0.8	1.6	1.3	0.94
5.0	0.8	1.2	1.7	0.96
10.0	0.9	1.6	1.6	0.93
20.0	0.9	0.8	2.4	0.95
40.0	0.8	0.9	2.2	0.95
70.0	0.9	0.5	4.2	0.96
100.0	1.0	0.3	2.7	0.95

Table S10. Fitting parameters and adjusted coefficients of determination (\bar{R}^2) of the fractal kinetics fits ($h = 0.5$) of the transient reflectance signals of charge carriers photo-generated in the samples containing PC500 mixed with Kronos1001 at 500 nm in the time domain between 5 μ s and 200 μ s after excitation with 1 mJ/cm² ($\lambda_{\text{ex}} = 355$ nm).

PC500 / %	$A / 10^{-3}$ a. u.	$k_{2,f} / 10^4$ a.u.	\bar{R}^2
0.0	1.4	1.8	0.95
0.4	1.4	2.2	0.93
5.0	1.4	1.7	0.95
10.0	1.3	1.9	0.91
20.0	1.6	1.1	0.94
40.0	1.3	1.2	0.93
70.0	1.5	0.5	0.95
100.0	2.0	0.7	0.96

Table S11: Fitting parameters and adjusted coefficients of determination (\bar{R}^2) of the fractal kinetics fits ($h = 0.5$) of the transient reflectance signals of charge carriers photo-generated in the $\text{TiO}_2\text{-BaSO}_4$ samples at 500 nm in the time domain between 5 μs and 200 μs after excitation with 1 mJ/cm^2 ($\lambda_{\text{ex}} = 355 \text{ nm}$).

$\text{TiO}_2 / \%$	$A / 10^{-3} \text{ a.u.}$	$k_{2,f} / 10^4 \text{ a.u.}$	\bar{R}^2
5.0	1.1	1.8	0.77
10	1.1	1.8	0.94
25	1.1	1.7	0.94
50	1.1	1.8	0.94
100	1.1	2.0	0.96

Table S12: Fitting parameters and adjusted coefficients of determination (\bar{R}^2) of the fractal kinetics fits ($h = 0.5$) of the transient reflectance signals of charge carriers photo-generated in the $\text{TiO}_2\text{-Na}_2\text{CO}_3$ samples at 500 nm in the time domain between 5 μs and 200 μs after excitation with 1 mJ/cm^2 ($\lambda_{\text{ex}} = 355 \text{ nm}$).

$\text{TiO}_2 / \%$	$A / 10^{-3} \text{ a.u.}$	$k_{2,f} / 10^4 \text{ a.u.}$	\bar{R}^2
5.0	1.5	7.7	0.69
10	1.4	8.8	0.77
25	1.2	6.5	0.82
50	1.4	7.6	0.88
100	1.1	2.0	0.96

Table S13: Fitting parameters and adjusted coefficients of determination (\bar{R}^2) of the fractal kinetics fits ($h = 0.5$) of the transient reflectance signals of charge carriers photo-generated in the $\text{TiO}_2\text{-CaCO}_3$ samples at 500 nm in the time domain between 5 μs and 200 μs after excitation with 1 mJ/cm^2 ($\lambda_{\text{ex}} = 355 \text{ nm}$).

$\text{TiO}_2 / \%$	$A / 10^{-3} \text{ a.u.}$	$k_{2,f} / 10^4 \text{ a.u.}$	\bar{R}^2
5.0	1.0	2.0	0.93
10	1.0	1.5	0.94
25	1.0	1.5	0.97
50	1.1	1.6	0.97
100	1.1	2.0	0.96

Table S14: Results of the fractal kinetics fits of the transient reflectance signals of charge carriers photo-generated in the TiO₂ paints at 500 nm after laser excitation with 1 mJ/cm² ($\lambda_{ex} = 355$ nm) in the time domain from 5 μ s to 200 μ s ($h = 0.5$).

	$A / 10^{-3} \text{ a.u.}$	$k_{2,f} / 10^4 \text{ a.u.}$	\bar{R}^2
Lithium	5.2	1.0	0.82
Iron	5.8	0.7	0.84
Copper	2.4	2.9	0.48
Zinc	7.9	0.8	0.92
Cobalt	11.6	1.5	0.85
Reference	3.1	5.9	0.54

Table S15: Results of the fractal kinetics fits of the transient reflectance signals of charge carriers photo-generated in PC105 observed in the range from 400 to 700 nm after excitation with 1 mJ/cm² ($\lambda_{ex} = 355$ nm) in the time domain from 40 ns to 200 μ s.

Wavelength	h	$k_{2,f} / 10^4 \text{ a.u.}$	$A / 10^{-2} \text{ a.u.}$	\bar{R}^2
400	0.54	0.67	129.3	0.97
420	0.65	0.14	*	0.96
440	0.70	0.07	*	0.95
460	0.71	0.05	*	0.96
480	0.71	0.05	190.2	0.97
500	0.72	0.05	111.2	0.96
520	0.67	0.09	18.6	0.97
540	0.69	0.07	29.1	0.96
560	0.66	0.11	13.0	0.97
580	0.67	0.09	12.7	0.97
600	0.66	0.10	9.8	0.96
620	0.67	0.09	11.0	0.96
640	0.63	0.16	6.4	0.94
660	0.59	0.28	4.8	0.92
680	0.63	0.17	4.8	0.88
700	0.59	0.13	3.4	0.78

* fitting process failed to produce reasonable A parameters

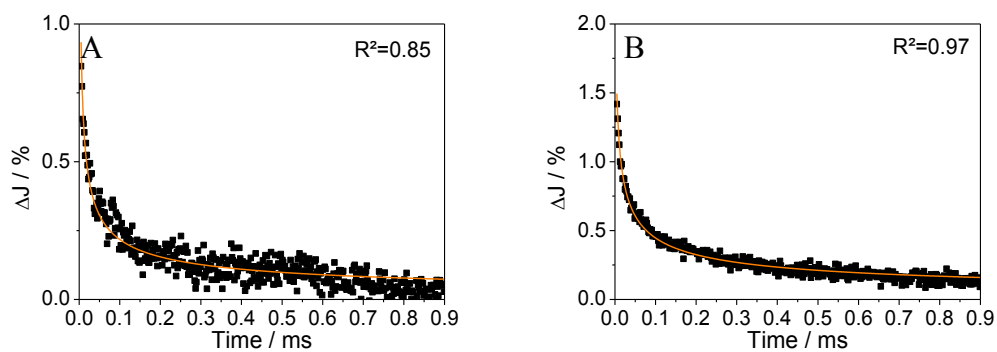


Figure S16: Transient reflectance signals of charge carriers photo-generated in PC105 at 500 nm (black) and fractal kinetics fit (orange) after laser excitation with 0.6 mJ/cm² (A) and 5.1 mJ/cm² (B) ($\lambda_{\text{ex}} = 355$ nm).

Table S17: Results of the power-law fits ($\Delta J = At^{-x}$) of the transient reflectance signals of charge carriers photo-generated in PC105 at 500 nm after excitation with 0.6 mJ/cm² and 5.1 mJ/cm² ($\lambda_{\text{ex}} = 355$ nm).

Laser intensity	0.6 mJ/cm ²	5.1 mJ/cm ² .
$A / 10^{-5} \text{ a. u.}$	5.7	17.0
$x / \text{a. u.}$	0.41	0.36
$\bar{R}^2 / \text{a. u.}$	0.875	0.953

Table S18: Fitting parameters and adjusted coefficients of determination (\bar{R}^2) of the fractal kinetics fits of the TRMC of charge carriers photo-generated in P25 after laser excitation ($\lambda_{\text{ex}} = 355$ nm).

	$A / 10^{19} \text{ a. u.}$	$k_{2,f} / \text{a.u.}$	h	\bar{R}^2
TRMC	0.6	2.8	0.95	0.52

Table S19: Fitting parameters and adjusted coefficients of determination (\bar{R}^2) of the fractal kinetics fits of the transient reflectance signals of charge carriers photo-generated in tungsten oxide at 440 nm after excitation with 2 mJ/cm² ($\lambda_{\text{ex}} = 355$ nm).

	$A / 10^{-2} \text{ a. u.}$	$k_{2,f} / 10^4 \text{ a.u.}$	h	\bar{R}^2
Tungsten oxide	0.6	0.6	0.52	0.98

Table S20: Fitting parameters and adjusted coefficients of determination (\bar{R}^2) of the fractal kinetics fits of the transient reflectance signals of charge carriers photo-generated in zinc ferrite measured at 540 nm after excitation with 2 mJ/cm² ($\lambda_{\text{ex}} = 355$ nm).

	$A / 10^{-2} \text{ a.u.}$	$k_{2,f} / 10^4 \text{ a.u.}$	h	\bar{R}^2
Zinc ferrite	2.0	0.6	0.55	0.73

Table S21: Fitting parameters and adjusted coefficients of determination (\bar{R}^2) of the fractal kinetics fits of the transient reflectance signals of charge carriers photo-generated in samples containing PC105 mixed with Kronos1001 at 500 nm in the time domain between 5 μs and 200 μs after excitation with 1 mJ/cm² ($\lambda_{\text{ex}} = 355$ nm).

PC105 / %	$A / 10^{-2} \text{ a.u.}$	$k_{2,f} / 10^4 \text{ a.u.}$	h	\bar{R}^2
0.0	4.1	1.6	0.56	0.92
0.4	2.8	1.6	0.53	0.93
5.0	2.1	1.0	0.57	0.87
10.0	3.6	0.8	0.56	0.95
20.0	5.3	0.5	0.58	0.97
40.0	5.5	0.3	0.61	0.96
70.0	12.9	0.1	0.68	0.98
100.0	7.6	0.2	0.61	0.99

Table S22: Fitting parameters and adjusted coefficients of determination (\bar{R}^2) of the fractal kinetics fits of the transient reflectance signals of charge carriers photo-generated in samples containing PC500 mixed with Kronos1001 at 500 nm in the time domain between 5 μ s and 200 μ s after excitation with 1 mJ/cm² ($\lambda_{\text{ex}} = 355$ nm).

PC500 / %	$A / 10^{-2}$ a.u.	$k_{2,f} / 10^4$ a.u.	h	\bar{R}^2
0.0	4.1	1.6	0.56	0.93
0.4	3.9	1.19	0.56	0.93
5.0	4.2	0.54	0.61	0.93
10.0	3.6	0.92	0.57	0.93
20.0	4.8	0.35	0.61	0.95
40.0	4.3	0.26	0.65	0.94
70.0	64.7	0.03	0.78	0.93
100.0	48.0	0.04	0.76	0.94

Publications

Publications as main author

1. Granone, L.I.; Sieland, F.; Zheng, N.; Dillert, R.; Bahnemann, D. W. Photocatalytic Conversion of Biomass into Valuable Products: A Meaningful Approach?. *Green Chemistry* **2018**, *20*, 1169-1192.
2. Sieland, F.; Schneider, J.; Bahnemann, D. W. Photocatalytic Activity and Charge Carrier Dynamics of TiO₂ Powders with Binary Particle Size Distribution. *Phys. Chem. Chem. Phys.* **2018**, *20*, 8119-8132.
3. Sieland, F.; Duong, A.-T.; Schneider, J.; Bahnemann, D. W. Influence of Inorganic Additives on the Photocatalytic Removal of Nitric Oxide and Charge Carrier Dynamics of TiO₂ Powders. *Journal of Photochemistry and Photobiology A: Chemistry* **2018**, In Press (DOI:10.1016/j.jphotochem.2018.01.036).
4. Sieland, F.; Schneider, J.; Bahnemann, D. W. Fractal Charge Carrier Kinetics in TiO₂. *J. Phys. Chem. C* **2017**, *121* (43), 24282-24291.

Non-peer-reviewed publications

1. Sieland, F.; Schneider, J.; Lippmann, T.; Bahnemann, D. W. Understanding Charge Transfer Processes on Metal Oxides – A Laser-Flash-Photolysis Study. *Proc. SPIE* **2016**, 99350G1-10.

Co-authored publications

1. Nie, J; Schneider, J.; Sieland, F.; Xia, S.; Bahnemann, D. W. The Role of Au Loading for Visible-Light Photocatalytic Activity of Au-TiO₂ (Anatase). *Journal of Photochemistry and Photobiology A: Chemistry* **2018**, In Press (DOI:10.1016/j.jphotochem.2018.03.016).
2. Faustino, L.; Souza, B.; Nunes, B.; Duong, A.-T.; Sieland, F.; Bahnemann, D.W.; Patrocínio, A. Photocatalytic CO₂ reduction by Re(I) polypyridyl complexes immobilized on niobates nanoscrolls. *ACS Sustain. Chem. Eng.* **2018**, In Press (DOI:10.1021/acssuschemeng.7b04713).
3. Nie, J; Patrocínio, A. O.; Hamid, S.; Sieland, F.; Sann, J.; Xia, S.; Bahnemann, D. W.; Schneider, J. New Insights into the Plasmonic Enhancement for Photocatalytic

H₂ Production by Cu-TiO₂ upon Visible Light Illumination. *Physical Chemistry Chemical Physics* **2018**, *20*, 5264-5273.

4. Lim, J.; Kwak, D.Y.; Sieland, F.; Kim, C.; Bahnemann, D. W.; Choi, W. Visible Light-Induced Catalytic Activation of Peroxymonosulfate Using Heterogeneous Surface Complexes of Amino Acids on TiO₂. *Appl. Catal. B: Environ.* **2018**, *225*, 406-414.
5. Ihrner, N.; Johannisson, W.; Sieland, F.; Zenkert, D.; Johansson, M. Structural Lithium Ion Battery Electrolytes (SBE's) via Reaction Induced Phase-Separation, High Stiffness in Combination with High Ionic Conductivity. *Journal of Materials Chemistry A* **2017**, *5*, 25652-25659.

Oral presentations

F. Sieland, J. Schneider, D.W. Bahnemann, "Kinetic Analysis of Charge Carrier Recombination in TiO₂", Russian-German Workshop, National University of St. Petersburg, October 16-20, 2017, St. Petersburg, Russia.

F. Sieland, J. Schneider, D.W. Bahnemann, "Fractal Charge Carrier Kinetics in TiO₂", New Photocatalytic Materials for Environment, Energy and Sustainability 2 (NPM-2), Intercity Hotel Göttingen, July 3-6, 2017, Ljubljana, Slovenia.

F. Sieland, J. Schneider, T. Lippmann, D.W. Bahnemann, "Understanding Charge Transfer Processes on Metal Oxides- A Laser Flash-Photolysis Study", SPIE Optics and Photonics, Convention Center San Diego, August 28-September 1, 2016, San Diego, USA.

F. Sieland, J. Schneider, D.W. Bahnemann, "Influence of Water on Charge Carrier Kinetics in TiO₂", New Photocatalytic Materials for Environment, Energy and Sustainability (NPM-1), Intercity Hotel Göttingen, June 7-10, 2016, Göttingen, Germany.

Poster presentations

F. Sieland, Anh-Thu Duong, J. Schneider, D.W. Bahnemann, “Improving Photocatalytic Paints”, Nanoday 2017, Laboratorium für Nano- und Quantenengineering (LNQE), Leibniz University Hannover, September 28, 2017, Hannover, Germany.

F. Sieland, Anh-Thu Duong, J. Schneider, D.W. Bahnemann, “Influence of Inorganic Additives on the Charge Carrier Dynamics and the Photocatalytic NO Degradation of TiO₂ Powders”, 6th International Conference on Semiconductor Photochemistry (SP6), Carl von Ossietzky University, September 11-14, 2017, Oldenburg, Germany.

F. Sieland, J. Schneider, D.W. Bahnemann, “Charge Carrier Kinetics in Semiconductor Materials”, International School for Materials for Energy and Sustainability (ISMES VI), Caltech, July 16-22, 2017, Pasadena, USA.

Barbara N. Nunes, Leandro A. Faustino, Breno L. Souza, Anh-Thu Duong, Fabian Sieland, Detlef W. Bahnemann, Antonio Otavio T. Patrocínio, “Spectroscopic Characterization of Re(I) Polypyridyl Complexes Adsorbed on Niobate Nanosheets“, 22nd International Symposium on Photochemistry and Photophysics of Coordination Compounds (ISPPCC 2017), St. Catherine’s College, July 9-14, 2017, Oxford, UK.

F. Sieland, J. Schneider, L. Rehbock, D.W. Bahnemann, “Through Space Degradation of Luminescent Europium Dyes with TiO₂”, Nanoday 2016, Laboratorium für Nano- und Quantenengineering (LNQE), Leibniz University Hannover, September 29, 2016, Hannover, Germany.

F. Sieland, J. Schneider, T. Lippmann, D.W. Bahnemann, “Photocatalytic Activity and Charge Carrier Reaction Dynamics of Physically Mixed TiO₂ Powders with Binary Particle Size Distribution”, IPS 21, Holiday Inn Moskovskie Vorota, July 25-29, 2016, St. Petersburg, Russia.

Curriculum vitae

Personal data

Name **Sieland, Fabian**

Date of birth **04.09.1990**

Place of birth **Bad Pyrmont, Germany**

Education

Since 10/2015 PhD Student at the Leibniz University of Hannover, Institute of Technical Chemistry: “Fractal Charge Carrier Recombination Kinetics in Photocatalytic Systems”.

02/2015 – 08/2015 Master Thesis at the Kungliga Tekniska Högskolan (KTH) in Stockholm, Sweden: “Novel Multifunctional Solid Polymer Electrolytes for Lithium Ion Conduction in Structural Batteries“.

10/2013 – 09/2015 Master of Science (M.Sc.) in Chemistry at the University of Paderborn, Major: Synthesis and Structure.

06/2013 – 08/2013 Bachelor Thesis in Cooperation with Lanxess, carried out at the “High Performance Rubber Research Center“ in Qingdao, China: “Determination of the Hansen Solubility Parameters (HSP) of EPDM by Swelling Experiments and Correlation with the Flory-Huggins Interaction Parameter“.

10/2010 – 09/2013 Bachelor of Science (B.Sc.) in Chemistry at the University of Paderborn.

08/2003 – 06/2010 Abitur at the Humboldt Gymnasium Bad Pyrmont